Warming and Forest Thinning Effects on the Hydrologic Cycle in the Beaver Creek

by

Charles Joshua Cederstrom

A Thesis Presented in Partial Fulfillment
of the Requirements for the Degree
Master of Science

Approved November 2021 by the
Graduate Supervisory Committee:

Enrique R. Vivoni, Chair
Giuseppe Mascaro
Bohumil Svoma

ARIZONA STATE UNIVERSITY

December 2021

ABSTRACT

Observational evidence is mounting on the reduction of winter precipitation and an earlier snowmelt in the southwestern United States. It is unclear, however, how these changes, along with forest thinning, will impact water supplies due to complexities in the precipitation-streamflow transformation. In this study, I use the Triangulated Irregular Network-based Real-time Integrated Basin Simulator (tRIBS) to provide insight into the independent and combined effects of climate change and forest cover reduction on the hydrologic response in the Beaver Creek (~1100 km^2) of central Arizona. Prior to these experiments, confidence in the hydrologic model is established using snow observations at two stations, two nested streamflow gauges, and estimates of spatially-distributed snow water equivalent over a long-term period (water years 2003-2018). Model forcings were prepared using station observations and radar rainfall estimates in combination with downscaling and bias correction techniques that account for the orographic controls on air temperature and precipitation. Model confidence building showed that tRIBS is able to capture well the variation in snow cover and streamflow during wet and dry years in the 16 year simulation period. The results from this study show that the climate change experiments increased average annual streamflow by 1.5% at +1°C of warming. However, a 28% decrease in streamflow occurs by +6°C of warming as evapotranspiration (ET) increases by 10%. Forest thinning shifted the warming threshold where ET increases reduce streamflow yield until +4°C of warming as compared to no forest thinning when this threshold occurs at +2°C. An average increase in streamflow of 12% occurs after forest thinning across all climate scenarios. While the snow covered area is unaffected by thinning, the volume of snowmelt increases and is linked to the

higher water yield. These findings indicate that water managers can expect decreases in streamflow due to climate change but may be able to offset these impacts up to a warming threshold by thinning forested areas within the Beaver Creek.

ACKNOWLEDGEMENTS

This work was completed under the project “Watershed Response to Climate Change and Forest Thinning in the Beaver Creek of central Arizona” funded by the Salt River Project through the Salt River Project – Joint Research Program. The views expressed in this work do not necessarily represent those of the supporting organization. I would also like to thank Gretchen Baumgardner for her assistance in providing initial simulation materials from Hawkins (2012). I cannot thank Dr. Enrique R. Vivoni enough for all of the assistance and advice with aspects of school, life, and this work throughout my master’s degree. I would also like to thank my committee member Dr. Giuseppe Mascaro and Bohumil Svoma for the support and feedback through my time as a masters student. I am grateful for everyone in the hydrologic science and sustainability research group who I was able to share my experiences with.

I would like to acknowledge Research Computing at Arizona State University for providing high performance computing center resources that have contributed to the research results reported within this paper.

Lastly, I would like to thank all of my family and friends who supported me over the course of this masters degree. Whether it be a place to live or someone to talk with I could not have got this done without these people in my life.

TABLE OF CONTENTS

Page

LIST OF TABLES vii

LIST OF FIGURES ix

CHAPTER

1 INTRODUCTION 1

1.1 Literature Review 2

2 STUDY AREA & DATASETS 9

2.1 Study Area & Characteristics 9

2.2. Datasets 12

2.2.1 Precipitation 13

2.2.2 Meteorological 15

2.2.3 Soils 16

2.2.4 Land Cover and Vegetation 18

2.2.5 Bedrock 22

2.2.7 Snow Water Equivalent 24

3 METHODOLOGY 26

3.1 Precipitation Bias-Correction 26

3.2 Meteorological Forcing Preparation 28

3.2.1 Gap Filling Station Data 28

3.2.1 Localized Lapse Rates & Downscaling 30

3.3 Simulation Experiments 32

3.3.1 Climate Change 33

CHAPTER Page

3.3.2 Forest Thinning 34

3.4 tRIBS Model Overview 39

3.4.1 Snowpack Model 40

3.4.2 Runoff Production and Infiltration 46

3.4.3 Surface Energy Balance 49

3.4.4 Canopy Interception and Evapotranspiration 50

4 RESULTS AND DISCUSSION 52

4.1 Model Calibration and Validation 52

4.1.1 Soil Parameters 53

4.1.2 Land Cover Parameters 57

4.1.3 Model Initialization 59

4.1.4 Performance Metrics 61

4.1.5 Point Scale Modelling 61

4.1.6 Basin Scale Modelling 68

4.2 Simulation Experiments 80

4.2.1 Water Balance Impacts 81

4.2.3 Changes in Snowpack 83

4.2.2 Changes in Evapotranspiration 87

4.2.4 Changes in Streamflow 93

5 CONCLUSIONS & FUTURE WORK 98

REFERENCES 103

APPENDIX Page

A. OBSERVATIONAL DATASETS 115

B. GIS DATASETS 118

C. MODEL SETUPS.....121

D tRIBS MODEL DOCUMENTATION.....126

E. FIGURES AND SCRIPTS 138

F. ANNUAL WATER BALANCES.....142

LIST OF TABLES

Table Page

1. Study area characteristics for the Beaver Creek and the two subwatersheds. Note that the characteristics were calculated using ArcMap 10.3 using a 1/3 arc-second DEM. 11

2. Station characteristics for daily and hourly stations. 14

3. Areal coverage of the soil classifications in the Beaver Creek and its subwatersheds. 17

4. Areal coverage for land cover classification in the Beaver Creek and subwatersheds. 19

5. Coefficients of regression derived from linear regression of monthly average air temperature and elevation of PRISM raster cells. The regression equation follows the form: $TA = aZ + b$ where *TA* is the air temperature and *Z* is the elevation. ... 31

6. Summary of model simulation experiments with acronyms and descriptions. 33

7. tRIBS soil parameter descriptions. 53

8. Soil parameter values for the Beaver Creek watershed. Soil classes that span both Wet and Dry Beaver Creek were separated into unique types for each watershed. 54

9. tRIBS land cover parameter descriptions. 57

10. Land cover parameter values for Beaver Creek watershed. 58

Table Page

11. Distributed snow model parameters adjusted during the calibration process. Note that initial parameters are those derived from Rinehart et al., (2008). 62

12. Model land cover and soil parameters from calibration at Happy Jack and validation at Bar-M SNOTEL stations. Parameter values for Bar-M were retrieved from the watershed scale model. 67

13. Performance metrics for Happy Jack and Bar-M snowpack simulations. Metrics were calculated using daily average SWE for the cold season (NOV. to APR.). .. 67

14. Performance metrics between estimated and modeled basin average SWE for the calibration and validation periods. Metrics computed at a daily resolution during only months within the cold season. 71

15. Model performance metrics for quantifying modeled hourly streamflow performance for Wet and Dry Beaver Creek broken down by season of the year. Cold season corresponds to November to April while warm season is May to October. 74

16. Watershed scale water balance for the entire Beaver Creek. Note that Q_{sim} is the simulated streamflow at the model outlet..... 79

17. Summary of pre- and post-treatment differences in LAI, p, S, and kt and change factors used derive post-treatment values. 81

LIST OF FIGURES

Figure Page

1. Verde River watershed in the state of Arizona, USA. (a) Beaver Creek watershed digital elevation model (DEM) with polygons indicating Wet and Dry Beaver Creek subwatersheds along with locations of USGS stream gauges, meteorological stations, and precipitation gauges..... 10

2. (a) Natural color aerial imagery from NAIP (2019) showing Bar-M and Happy Jack SNOTEL locations within the Beaver Creek. (b) Photograph of snow pillow measurement instrumentation at Bar-M. (b) Photograph of the measurement station at Happy Jack. Photographs obtained from NRCS (1997)..... 12

3. Map of soil texture types in the Beaver Creek watershed from SSURGO. 18

4. Map of land cover types with 30 m raster cells in Beaver Creek watershed from LANDFIRE REMAP. 20

5. Maps of (a) vegetation fraction and (b) vegetation heights in 30 m raster cells in the Beaver Creek watershed from LANDFIRE REMAP..... 21

6. Map of depth to bedrock for the Beaver Creek Watershed from gNATSGO..... 23

7. Daily map of SWE from SWANN on February 23, 2008, for the state of Arizona based on the Salt River Project private version of SWANN at 1 km resolution.... 24

Figure Page

8. Monthly mean precipitation as a function of elevation from stations and NEXRAD for (a) January and (b) July over a 16 year period. (c) Monthly mean areal precipitation for the Beaver Creek from raw and bias corrected NEXRAD. Dashed and solid lines in (a) and (b) are linear regressions for stations and NEXRAD, respectively. 28

9. Comparison of air temperature lapse rates for (a) January and (b) July from PRISM and Liston and Elder (2006b). Symbols corresponds to average air temperature for each raster cell from PRISM that are located within the Beaver Creek watershed. 31

10. (a) Scatter plot of pre- and post-treatment basal area from 4FRI dataset with a dashed line showing the linear regression. (b) Relative frequency distributions of basal area from 4FRI and linear regression. 35

11. (a) Pre-treatment basal area for the ponderosa pine forest in the Beaver Creek at 30 m resolution. (b) Percent change in ponderosa pine basal area from modeled forest thinning using linear regression. 36

12. Map of vegetation fraction after thinning in the ponderosa pine forest. 39

13. Map of initial groundwater depth at the start of the calibration period (October 1st, 2002) after 4 years of model spin-up using raw 12 km resolution forcing from the NLDAS-2 dataset. 60

14. Hourly time series of precipitation, air temperature, and modeled versus observed snow water equivalent at Happy Jack SNOTEL. 63

Figure Page

15. (a) Monthly mean time series of precipitation, modeled versus observed volumetric soil moisture, $\theta_{sur.}$ (b) Monthly mean modeled versus observed soil temperature, T_s. Monthly standard deviations are shown as error bars. 65

16. Hourly time series of precipitation, air temperature, and modeled versus observed snow water equivalent at Bar-M SNOTEL. 68

17. (a) Modeled and estimated mean snow water equivalent timeseries from calibration (WY2003-2010) and validation (WY2011-2018). Mean winter (NOV.-APR.) snow water equivalent from 1km raster cells for (b) calibration and (c) validation. 70

18. Maps of average difference in SWE between modeled and estimated (modeled minus estimated) across water years for (a) calibration and (b) validation periods. 73

19. Hourly time series of mean areal precipitation and modeled versus observed streamflow for (a) Wet Beaver Creek and (b) Dry Beaver Creek. 75

20. Modeled versus observed streamflow for calibration and validation periods in the (a, b) Wet Beaver Creek and (c, d) Dry Beaver Creek. Results are shown as monthly totals for precipitation and monthly means for streamflow with shaded curves and error bars showing ±1 standard deviations. 76

21. Hourly cumulative streamflow from observations and modeled for (a) Wet and (b) Dry Beaver Creek along with mean areal precipitation. 77

Figure Page

22. Percent change in components of the basin scale water balance for the climate change and forest thinning experiments. 82

23. (a – h) Average annual components of the basin scale water balance for Base Case and Post-treatment simulation experiments at +0, +1 +2, and +6°C of warming. Where *P* is precipitation, *SWE* is snow water equivalent, *M* is snowmelt, Sg is ground sublimation, Sc is canopy sublimation, *ET* is total evapotranspiration, $Esoil$ is bare soil evaporation, ETc is canopy evapotranspiration, ΔS is change is subsurface storage, and *R* is runoff. 83

24. Annual mean snowfall fraction during the cold season for +0, 1, 2, 4, and 6°C of warming (a, b, c, d, and e respectively). 85

25. (a) Mean monthly percent snow covered area and (b) mean monthly total snowmelt for the Base Case and Post-treatment scenarios at +0, 2, and 6° of warming. 86

26. Percent change in components of basin scale total evapotranspiration for the climate change and forest thinning experiments. 88

27. Total evapotranspiration results for warming and forest thinning experiments in the Beaver Creek for 16 years for +0, +2, and +6°C of warming (a, b, and c respectively) and (d) Base Case with warming experiments. Results are shown as monthly means with shaded curves representing ±1 standard deviation from the mean. 90

Figure Page

28. Difference maps of mean annual total evapotranspiration between (a) forest thinning experiments and (b, c, d, and e) climate change scenarios. 92

29. Modeled total evapotranspiration in the ponderosa pine forest compared to topographic index along with relative frequency of topographic index. Results shown for total evapotranspiration were averaged to integer values of topographic index. 93

30. Double mass curves of cumulative annual streamflow for experiments as compared to Base Case. Solid lines are linear regressions for each simulation experiment. . 94

31. Annual modeled streamflow compared against annual precipitation over a 16 year period for the 10 simulation experiments. Solid lines represent linear regressions across the climate change scenarios for the Base Case and Post-treatment experiments. Note that WY2005 was not used in the calculation of the regression equations due to the large under simulation during that year..... 96

32. Streamflow results for warming and forest thinning experiments in the Beaver Creek for 16 years for +0, +2, and +6°C of warming (a, b, and c respectively) and (d) Base Case with warming experiments. Results are shown as monthly means with shaded curves representing ±1 standard deviation from the mean..... 97

1 INTRODUCTION

Mid-latitude, subtropical regions across the globe are predicted to have the largest decrease in water resources due to climate change (IPCC, 2021). Water managers in the southwestern United States are confronted with projections indicating increased temperatures, declining snowpacks, and increased tree mortality due to wildfires (MacDonald, 2010; Xiao, 2021). In addition, the Southwest experiences highly variable precipitation from year to year which has historically been managed using reservoirs to reduce the variability in water supply for downstream communities (Philips et al., 2009). These reservoirs store snowmelt from high elevation mountainous regions and account for a large portion of the annual water supply for metropolitan areas like Phoenix, Arizona (Gooch et al., 2007). Thus, there is a need for increasing the understanding of streamflow response to changes in climate, so water managers such as the Salt River Project (SRP) can make improvements to surface water forecasting and management.

Forest structure and air temperature play an important role in the precipitation-streamflow transformation in mountainous regions with intermittent snowpacks (Mote et al., 2006; Hammond and Kampf, 2020). Studies have shown that warming will accelerate snowmelt and shift precipitation phase from solid to liquid (Fritze et al., 2011; Harpold et al., 2017). Additionally, extensive research over the last 70 years in ponderosa pine forested areas has shown the potential for increasing streamflow and reducing snow sublimation through forest thinning (Baker, 1986; Moreno et al., 2016; Svoma, 2017). Large forest thinning projects are already underway in Arizona such as the Four Forest Restoration Initiative (4FRI) which plans to thin about 10 million acres of ponderosa pine forest with the goal of reducing large scale wildfires (U.S Forest Service, 2015). Thus, it

is crucial for water managers to understand how the reduction of forest cover impacts hydrologic processes such as evapotranspiration and streamflow at the watershed scale. Furthermore, it is valuable for water managers to know the hydrologic response differences between pre- and post-forest thinning under the effects of climate change for the planning of future forest restoration projects.

This study investigates the hydrologic responses to climate change and forest thinning in a watershed of central Arizona. Using a physically-based, distributed hydrologic model, I aim to provide insight into how land cover and climate change might impact the basin scale water balance. To accomplish this, the model is tested at the point and watershed scale for simulating snow water equivalent and streamflow before exploring the separate and combined effects of climate change and forest thinning.

1.1 Literature Review

The Phoenix Metropolitan Area (PMA) is the 5th largest city in the United States with the fastest rate of population growth from 2010 to 2020 (U.S. Census Bureau, 2020). Like other arid regions in the southwestern US, the PMA obtains its water supply from a combination of groundwater, surface water, and reclaimed water (ADWR, 2021). Surface water supplies come from two main sources: Salt and Verde watersheds from the Salt River Project, and Colorado River water from the Central Arizona Project. The Central Arizona Project uses a diversion canal and a series of pumping stations to transport water from Lake Havasu to Tucson, Arizona. Since the construction of the project, the CAP has been a key provider of water for agricultural and residentials users in central and southern Arizona. The recent drought across much of the southwestern US has reduced inflows

into reservoirs on the Colorado River such that a federal shortage declaration was made for 2022 (MacEachern and Person, 2021). The new Drought Contingency Plan, finalized in 2020, states that Arizona, along with Nevada, are the first states to see reduced water supplies under shortage (U.S. Bureau of Reclamation, 2020). This reduction of Colorado River supply in Arizona will place a higher importance on management of local watersheds like the Salt and Verde Rivers.

Ponderosa pine forests that dominate the high elevations of the Salt and Verde watersheds have seen increases in the number and magnitude of severe forest fires along with insect-induced die off (Covington and Moore, 1994; Chojnacky et al., 2011). The reason for this is attributed to forest management policies implemented in the early 20th century to suppress forest fires (Allen et al., 2002). The result of such policies can be seen in the C.C. Cragin reservoir area of northern Arizona where tree stand density has increase from an estimated 100 to 6000 trees per an acre due to growth of primarily small diameter trees (U.S. Forest Service, 2018). Before widespread fire suppression, more common but less severe forest fires would remove small trees and ground litter that allow high intensity fires to spread rapidly across a landscape (Allen et al., 2002; Stambaugh et al., 2011). The regions most impacted by fire suppression are seasonally dry and produce an abundance of ground litter, like the ponderosa pine forests (Ryan et al., 2013, Huffman et al., 2015). Large forest fires pose significant problems to water resource managers due to increases in flooding which results in early releases of water from reservoirs to mitigate flood damages and increases in sediment transport into reservoirs that reduce storage capacity (Leonard et al., 2017; Sankey et al., 2017). Thus, it is critical for forest health to be restored to its natural state before human intervention (Covington and Moore,

1994). Forest thinning restoration project, such as 4FRI, aim to reduce the problems outlined above but there is also the potential for increased water supply in restored watersheds (Simonit et al., 2015).

The impact of large-scale forest restoration projects on watershed hydrologic processes and streamflow in semiarid regions has not yet been observed (Robles et al., 2017). Past studies on forest thinning typically use a set of smaller, paired watersheds to observe changes in runoff amounts (Brown et al., 1974; Baker 1986; Brown et al., 2005). The most relevant of these are the Beaver Creek Experimental watershed studies which implemented multiple methods of treatment like overstory removal and the creation of open clearings (Baker, 1984). Each of these treatment methods had different levels ranging from complete to light removal. The paired watershed studies found that removal of ponderosa pine led to increased runoff, ranging from 10-45% annually but that these reverted to pre-treatment values after 7 years (Baker, 1986). Additionally, it was found that north facing slopes retain the benefits of thinning longer than south facing slopes. In recent years, similar work in Colorado looked at the removal of vegetation due to bark beetle infestations (Biederman et al., 2015). Researchers found that reduction of ponderosa pine stand density showed no statistically significant change in streamflow and an increase in evapotranspiration, attributed to increased bare soil evaporation (Biederman et al., 2014; Biederman et al., 2015). Changes in streamflow at the basin scale from forest thinning are inconclusive and current projects are not occurring in a stationary climate where additional stressors like climate change serve to further alter ecosystem services.

The effects of human-induced climate warming through the release of greenhouse gases into the atmosphere on snow dominated watersheds in the western United States has been research extensively over recent decades (Leung and Wigmosta, 1999; Christensen et al., 2004; Adam et al., 2009; Elsner et al., 2010). Studies in the Upper Colorado River Basin (UCRB) show a shift in winter precipitation from snow to rain, faster winter snow melt, and reduced summer streamflow (Christensen et al., 2004). Using five different land surface models, Vano et al. (2012) estimated a 20% decrease of average annual streamflow from the UCRB by the middle of the 21st century. Certain climate models show increases in annual precipitation which could counteract losses to streamflow, but agreement between these models on future precipitation amounts is not apparent (Udall and Overpeck, 2017). Studies have focused on the UCRB due to its importance on water supply for many western states, but lesser focus has been placed on the Lower Colorado River Basin, in particular the Salt and Verde watersheds in Arizona.

Streamflow declines observed in the UCRB are not consistent across all the western United States (Nayak et al., 2010). Watersheds characterized by intermittent, shallower snowpacks with warmer temperatures like the Salt and Verde watersheds of the LCRB have not seen significant changes in streamflow volume due to the warming that has occurred in the 20th century (Robles et al., 2017). The lack of climate change signal has been attributed to runoff efficiency peaking during winter months and that the shift from snow to rain leads to the majority of runoff production occurring in winter rather than spring (Hammond et al., 2020). Comparing the latter to the UCRB where the timing of streamflow generated from snowmelt and peak energy demands are more strongly coupled than the LCRB suggests one hypothesis as to why losses in the UCRB are not

observed in the LCRB (Robles et al., 2021). Low evaporative demand during winter months means that although less snow is falling, rainfall is able to generate the same amount of annual streamflow. Additionally, atmospheric river events that occur in Central Arizona can generate large amounts of winter streamflow have been observed to be increasing in frequency since the middle of the 20th century. This indicates that a potential exists for increase winter supply under the effects of climate change (Singh et al., 2018; Robles et al., 2021).

Watershed management has becoming increasingly more difficult due stresses like climate change and unhealthy forests. Together, these have increased interest from local watershed managers in using tools that can help predict the response to these stresses. Physically-based, fully distributed hydrologic models are tools that have been used extensively in the research community over the last two decades. The adoption of these models outside the research community is low due to the lack of testing data and difficulties in parameterization (Fatichi et al., 2016). However, improvements in the availability of high temporal and spatial resolution remote sensing data from satellites has allowed the modelling of regional watersheds that have little to no ground observation networks (Ko et al., 2019). Furthermore, improvements in computational power and code parallelization allows for high-resolution, long-term modelling (Vivoni et al., 2011). While hydrological models are most used for the prediction of flood events, fully distributed models that explicitly account for earth system processes provide a virtual testbed that enables the testing of experimental hypotheses. This allows the testing of hypothesis that are too difficult to test in the real world or can aid in the design of real-world experiments. Additionally, these models enable prediction of future changes in

hydrological processes due to changes in the environment. Distributed models are at a pivotal moment after extensive testing and advancements in data availability where they are prime to see use outside of the research community.

While these models have seen widespread use in North America, applications in the semiarid regions of the southwester US are limited. Previous application of these models in this region focused mainly on warm season processes. Hawkins (2012), for example, used a distributed model to predict changes in streamflow response to the North American Monsoon (NAM) under a single climate scenario. Application of these models in semiarid watersheds of Arizona that experience snowpacks at higher elevations have received less attention due to the complexity of mountainous terrain controls on solar radiation and meteorological conditions (Young et al., 1999; Rinehart et al., 2008; Livneh et al., 2014). Notably, Hussein (2020) applied the National Water Model, a distributed hydrologic model, in the Oak Creek watershed of central Arizona which is known for large flood events due exposed bedrock and rugged terrain. Forecasting of streamflow was improved using a calibration procedure that targeted distinct flood generation mechanisms. In the Tonto Creek watershed of central Arizona, a distributed hydrological was used to examine the changes in hydrologic processes due to the 4FRI along with the effects of soil compaction from thinning (Moreno et al., 2016). The simulations showed that annual watershed scale runoff increased after thinning but may be more at risk to extreme hydrologic events due to lower subsurface storage and smaller snowpacks.

With a goal of analyzing the effects of forest thinning, this study follows efforts similar to Moreno et al. (2016). However, I do not consider changes to soil properties due to forest thinning activities due the difficulty in quantifying the magnitude of those

changes (Lopez et al., 2021). Nevertheless, this study uses newly available products like vegetation fraction and snow water equivalent and enhancement of model physics to improve simulation performance. Building off the model developed in Hawkins (2012), this study expands those efforts over the long-term, including snow processes in the cool season, and explores a greater number of climate change experiments that account for the range of most common future warming potentials.

In this study, a semiarid watershed in central Arizona, the Beaver Creek watershed, is investigated using physically-based distributed model. To do so, model confidence was established through simulations at the point scale for two snow measurement stations. Furthermore, calibration of the watershed scale model was completed over a 16 year period using streamflow observations at two internal stream gauges along with estimates of spatially distributed snow water equivalent (SWE). Prior to calibration, a set of bias-corrected model forcings were prepared that account for the orographic controls on air temperature and precipitation in the watershed. After model calibration, a set of 9 additional simulation experiments were completed that account for both separate and combined effects of warming due to climate change and forest thinning. From these simulation experiments, changes in snow cover, evapotranspiration, and streamflow were analyzed using timeseries, spatial maps, and trends analysis.

2 STUDY AREA & DATASETS

2.1 Study Area & Characteristics

The study basin, Beaver Creek watershed (BCW), is located in the Central Arizona Highlands between Flagstaff and Camp Verde (111.61°W, 34.75°N). The watershed features a 1,625-meter elevation gradient, due to the Mogollon Rim that encompasses the northern most portion of the watershed. Surface water flows generated in the watershed aggregate in the Beaver Creek, which later drains into the Verde River (1108 km^2 above USGS gauge in Camp Verde, AZ 09505400). Beaver Creek is fed by Dry Beaver Creek (DBC), an intermittent creek which dominates the northeastern portion of the watershed, and Wet Beaver Creek (WBC), a perennial creek which dominates the southeastern portion of the watershed (Figure 1). Detailed characteristics of the Beaver Creek and the two subwatersheds are shown in Table 1.

The wide range of elevation in the watershed coincides with a variety of vegetation and soil types. The desert shrubland that dominates the lower elevations exists atop coarse loamy soils. Above the desert shrublands, soils are volcanic in origin, predominantly clay soil textures with bedrock lined stream channels that have little to no hydrologic connection to the geologic media below (Baker, 1982). The pinyon-juniper forest is predominately located between the desert shrubland and the high elevation Mogollon Rim. Table 3 presents a more detailed description of the percent coverage of the 13 soil classes in the Beaver Creek watershed. These soil classes are the main control on the transformation of precipitation to runoff in the tRIBS model. Similarly, Table 4 shows the percent coverage of the vegetation classes in the model. The vegetation classes

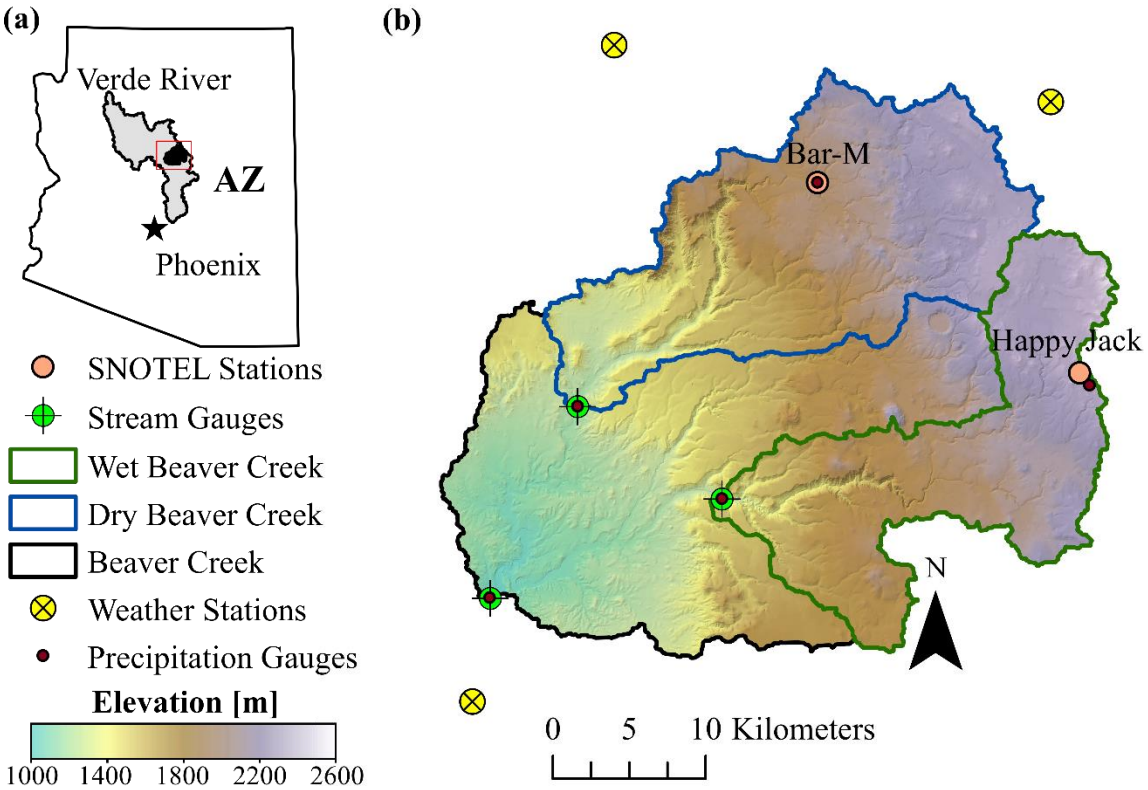

Figure 1. Verde River watershed in the state of Arizona, USA. (a) Beaver Creek watershed digital elevation model (DEM) with polygons indicating Wet and Dry Beaver Creek subwatersheds along with locations of USGS stream gauges, meteorological stations, and precipitation gauges

control processes like the amount of transpiration, intercepted precipitation, and amount of solar shading at the soil surface.

Figure 1 highlights the presence of two SNOw TELemetry (SNOTEL) sites within the Beaver Creek. SNOTEL stations are located across the western United States and were established by the Natural Resources Conservation Service to provide point-scale measurements of snow water equivalent, precipitation, and air temperature with some stations measuring additional variables (NRCS, 1977). The main site with the

Table 1. Study area characteristics for the Beaver Creek and the two subwatersheds. Note that the characteristics were calculated using ArcMap 10.3 using a 1/3 arc-second DEM.

Property	Units	Beaver Creek	Wet Beaver Creek	Dry Beaver Creek
ID	~	BC	WBC	DBC
USGS Stream Gauge ID	~	09505400	09505200	09505350
Total Area	km^2	1108	286	367
Length of main channel	km	~	23.6	22.9
Slope of main channel	m/km	~	30.6	25.4
Mean elevation	m	1735	1999	1883
Minimum/maximum elevations	m	974/2600	1225/2600	1128/2390
Std. elevation	m	394	241	321
Mean slope	%	16	14	17
Std. slope	%	20	20	24

longest record of historical data (1998-2021) is Happy Jack SNOTEL, located near the watershed boundary in the Wet Beaver Creek. The second SNOTEL, known as Bar-M, was installed in 2012 in cooperation with the Salt River Project (SRP) and only measures snow water equivalent, precipitation, and air temperature. Figure 2 shows the location of the two SNOTEL stations along with images of the station layout in the field.

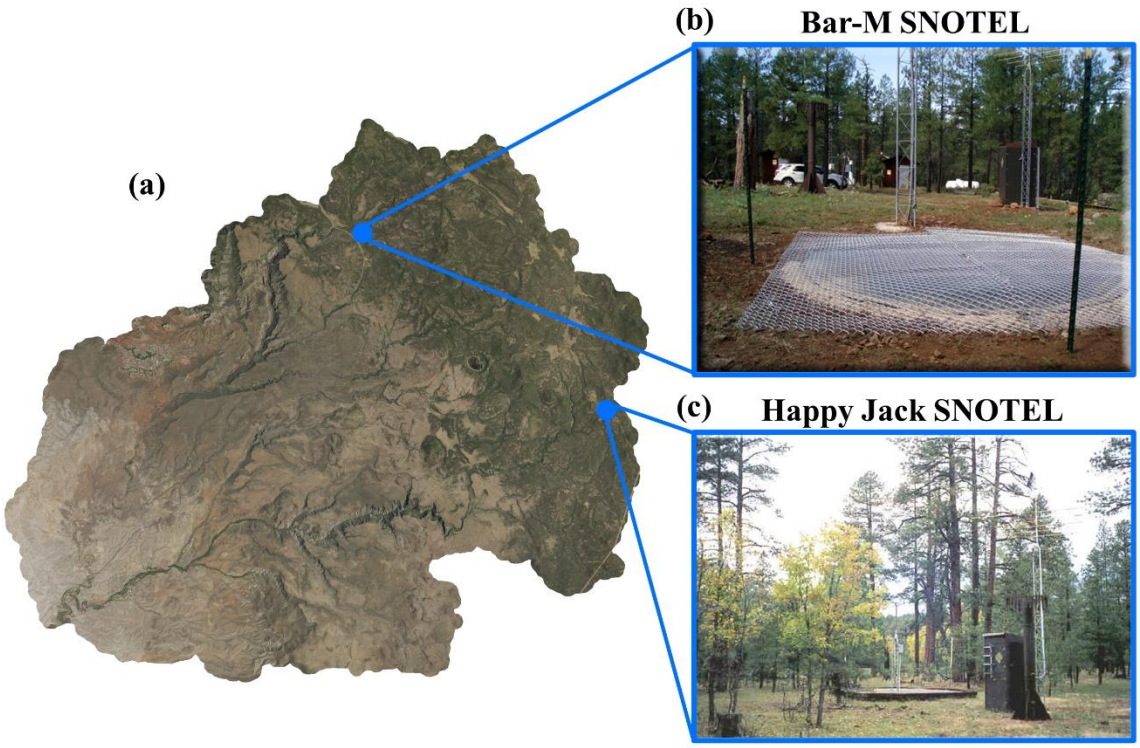

Figure 2. (a) Natural color aerial imagery from NAIP (2019) showing Bar-M and Happy Jack SNOTEL locations within the Beaver Creek. (b) Photograph of snow pillow measurement instrumentation at Bar-M. (b) Photograph of the measurement station at Happy Jack. Photographs obtained from NRCS (1997).

2.2. Datasets

There are a number of different datasets used in the study, ranging from time-varying spatially distributed raster data to single weather stations. These datasets are used either for comparison to simulation results or for the generation of model forcing. For this study, the processing of spatially distributed raster data follows the same procedure: raw raster data is obtained and then clipped and reprojected into the UTM Zone 12N, North American 1983 datum coordinate system using the Geospatial Data Abstraction Library (GDAL). GDAL is a robust and open-source software package that is run from command line for process automation and can handle all commonly used file formats (GDAL,

2020). After processing the raw raster data into the geoTIFF file format, Matlab is used to define the geospatial domain and cell size and convert the raster cell data into ASCII grids. As with the geospatial data, processing time series data followed a consistent procedure. Time series are imported into Matlab as timetables (links dates/time with each point of data). If the dataset is to be used as forcing, Matlab is used to write text files into format required by tRIBS. Other datasets were saved into a Matlab file format for quicker data processing times.

2.2.1 Precipitation

Two different forms of precipitation data were used in the study: rain gauges and weather radar. A number of rain gauges are present within or near the Beaver Creek watershed. The agencies managing these different gauges are the United States Geological Survey (USGS), United States Forest Service (USFS), Salt River Project (SRP), and Yavapai County Flood Control District (YCFCD). The largest network of gauges in the area are from YCFCD which are tipping bucket gauges used for flood alerts. However, these observations have missing data during the winter season and were not used. Measuring snowfall with tipping bucket style gauges is subject to multiple different sources of error such as wind, frozen equipment, and low snowfall rates (Rasmussen et al., 2015). The rain gauge data provided by SRP are daily totals of precipitation from either USGS or SRP gauges that have been quality controlled by staff meteorologists. Detailed information about these stations is found in Table 2.

Table 2. Station characteristics for daily and hourly stations.

Name	Lat. [°]	Long. [°]	Elevation [m]	Period of Record
SNOTEL (Hourly)				
Happy Jack	-111.42	34.75	2326	06/01/1999 - Present
Bar-M	-111.6	34.867	1949	09/06/2012 - Present
Precipitation Gauges (Daily)				
Bar-M	-111.61	34.861	1945	03/17/1990 - Present
Dry Beaver	-111.77	34.73	1126	01/01/1986 - Present
Happy Jack	-111.41	34.743	2376	11/06/1987 - Present
Montezuma	-111.84	34.609	972	03/15/1990 - Present
Wet Beaver	-111.67	34.975	1225	01/01/1986 - Present
Meteorological Stations (Hourly)				
Happy Jack	-111.34	34.618	2071	06/01/2010 - Present
Mormon Lake	-111.44	34.911	2256	10/01/1996 - Present
Oak Creek	-111.75	34.943	1501	12/01/1992 - Present
Verde	-111.85	34.554	945	11/01/1993 - Present

The second source of precipitation data is the Next Generation Weather Radar (NEXRAD) Stage IV. NEXRAD Stage IV is aggregated, quality controlled, and bias-corrected dataset distributed by the Colorado River Basin Forecasting Center (CRBFC). The Stage IV product is an hourly product with a 4 km grid cell size that is created using radar data from stations located throughout the Colorado River Basin (Du, 2011). The nearest radar is operated by the Phoenix branch of National Oceanic and Atmospheric Administration (NOAA). While the Stage IV product is bias corrected by the CRBFC, weather radars are known to have poorer performance in winter months due to orographic enhancement of precipitation in mountainous regions (Zhang et al., 2012). An additional local bias correction was completed using data from the five rain gauges from SRP to generate the precipitation forcing for the model, detailed in section 3.1.

2.2.2 Meteorological

There are five meteorological variables used in the hydrologic simulations: wind speed (US), relative humidity (RH), air pressure (PA), incoming solar radiation (IS), and air temperature (TA). Three different datasets were combined to generate the meteorological forcing. Weather station data from four Remote Automated Weather Stations (RAWS) and one SNOw TELelemetry (SNOTEL) station are the primary dataset. Hourly gridded weather data from North American Land Data Assimilation System (NLDAS) were used for air pressure and for the gap filling of station data. Lastly, air temperature data from Parameter-Elevation Regression on Independent Slope Model (PRISM) was used for calculating local air temperature lapse rates for the spatial interpolation of station data. A detailed description of the methodology for meteorological model forcing preparation is described in section 3.2.

Details of the five weather stations used to prepare model forcing are available in Table 2 with spatial locations shown in Figure 1. The RAWS stations are a set of interagency managed weather stations that are typically used for monitoring fire hazard (WRCC, 2013). Figure 1 shows that all the RAWS are in close proximity to the Beaver Creek Watershed boundary, therefore useful for the purposes of downscaling. NLDAS-2 is a gridded (12 km, hourly) product derived from North American Regional Analysis (NARR) through spatial interpolation (Cosgrove, 2003). It was used for model initialization due to the lack of station observations before the year 2002 and to gap filling of station data. PRISM is a nationwide climate data set developed by Oregon State's PRISM Climate Group and is regarded as a highly accurate spatially distributed dataset for air temperature and precipitation in mountainous regions (PRISM Climate

Group, 1994). The version of PRISM used in this study is the daily average air temperature at 4 km resolution. PRISM is not a direct observation of air temperature but is a model output based on a localized regression equations that are parameterized using nearby observations and multiple physiographic indicators like elevation.

2.2.3 Soils

The soil map for the BCW was previously developed in Hawkins (2012) using spatially distributed soils data from the Soil Survey Geographic Database (SSURGO) provided by the USDA (Soil Survey Staff, 2020). SSURGO data for the Beaver Creek has 73 unique soil types which were further aggregated into texture types to reduce model complexity. The details of this aggregation can be found in Hawkins (2012). The aggregation results in 13 different soil classes with their percent coverage of the watershed provided in Table 3.

Table 3. Areal coverage of the soil classifications in the Beaver Creek and its subwatersheds.

Soil Texture	Beaver Creek		Wet Beaver Creek		Dry Beaver Creek	
	Area (km^2)	Basin Coverage (%)	Area (km^2)	Basin Coverage (%)	Area (km^2)	Basin Coverage (%)
Silty Loam	138.5	11.4	53.5	18.7	57.3	15.7
Clay Loam (WBC)	117.0	9.7	68.6	23.9	3.8	1.0
Unweathered Bedrock (WBC)	109.6	9.1	46.8	16.3	~	~
Sandy Loam	81.8	6.8	~	~	36.0	9.8
Clay (WBC)	224.8	18.6	88.9	31.0	7.9	2.2
Water	0.8	0.1	0.1	0.1	~	~
Loamy Sand	0.2	0.0	~	~	~	~
Sand	11.0	0.9	~	~	2.7	0.7
Silty Clay Loam	1.9	0.2	~	~	~	~
Clay Loam (DBC)	117.0	9.7	0.2	0.1	93.4	25.5
Clay (DBC)	117.8	9.7	~	~	66.3	18.1
Unweathered Bedrock (DBC)	116.2	9.6	~	~	80.3	21.9
Loam	174.6	14.4	28.5	9.9	18.4	5.0

The spatial distribution of the soil classes in Table 3 is provided in Figure 3. The soil classes that spanned both the WBC and DBC subwatersheds were split into unique soil classes for each watershed. Doing so enabled the calibration of the soil parameters separately for each of the watersheds. The soil map in Figure 3 shows a general pattern of bedrock lined channels and clay soils at higher elevations. The low infiltration rates of bedrock and clay soil types leads to increased runoff generation and the potential for large flood events. Notably, during the winter of 1993 a flood event of 150 m^3/s was measured at the Wet Beaver Creek streamflow gauge which is the largest event of record.

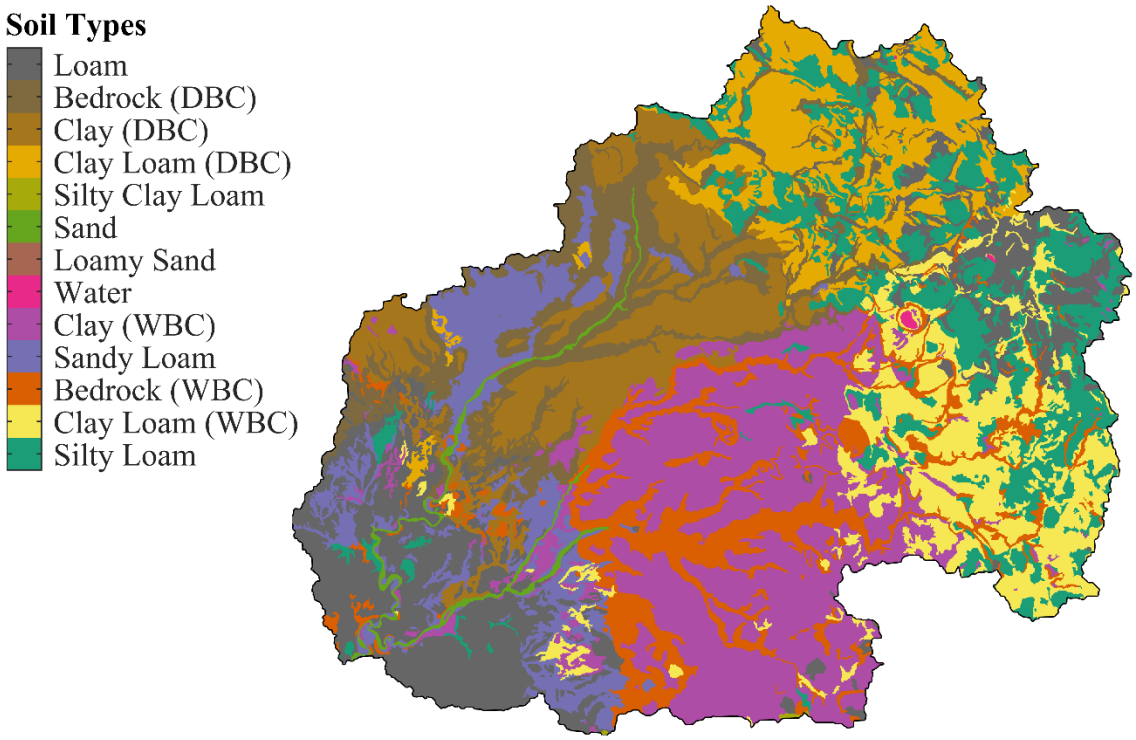

Figure 3. Map of soil texture types in the Beaver Creek watershed from SSURGO.

2.2.4 Land Cover and Vegetation

Land cover is a model input for the classification of different vegetation types within the watershed. There is a set of 12 parameters required by tRIBS that are based on vegetation types which play important roles in the modeling of evapotranspiration and snow dynamics. tRIBS possess the ability to ingest vegetation parameters in tabular form and raster grids. The Beaver Creek model uses a combination of both methods. The land cover product utilized in the study is LANDFIRE REMAP, developed by the USDA (Picotte et al., 2019). LANDFIRE REMAP is a newly updated (2020) version of the LANDFIRE product suite that serves to represent the environmental conditions in 2016. LANDFIRE REMAP takes advantage of satellite imagery, Light Detection and Ranging

Table 4. Areal coverage for land cover classification in the Beaver Creek and subwatersheds.

Land Cover Class	Beaver Creek		Wet Beaver Creek		Dry Beaver Creek	
	Area (km^2)	Basin Coverage (%)	Area (km^2)	Basin Coverage (%)	Area (km^2)	Basin Coverage (%)
Desert Shrub	226.5	20.4	22.3	7.8	23.5	6.4
Desert Riparian	28.2	2.5	5.8	2.0	16.0	4.4
Grassland	1.6	0.1	0.3	0.1	0.3	0.1
Pinyon-Juniper	407.9	36.8	96.5	33.6	119.2	32.4
Developed	28.0	2.5	1.2	0.4	12.4	3.4
Ponderosa Pine	394.6	35.6	152.9	53.2	195.2	53.1
Water	0.2	0.0	0.0	0.0	0.0	0.0
Desert	20.8	1.9	8.3	2.9	1.0	0.3

(LiDAR), and control plots to create a gridded product at 30 m resolution for entire United States. LANDFIRE REMAP vegetation types from the raw products includes highly detailed vegetation types which were aggregated to eight main vegetation types using methods outlined in Hawkins (2012). Table 4 and Figure 4 show the percent coverage and spatial distribution of the aggregated vegetation types in the Beaver Creek.

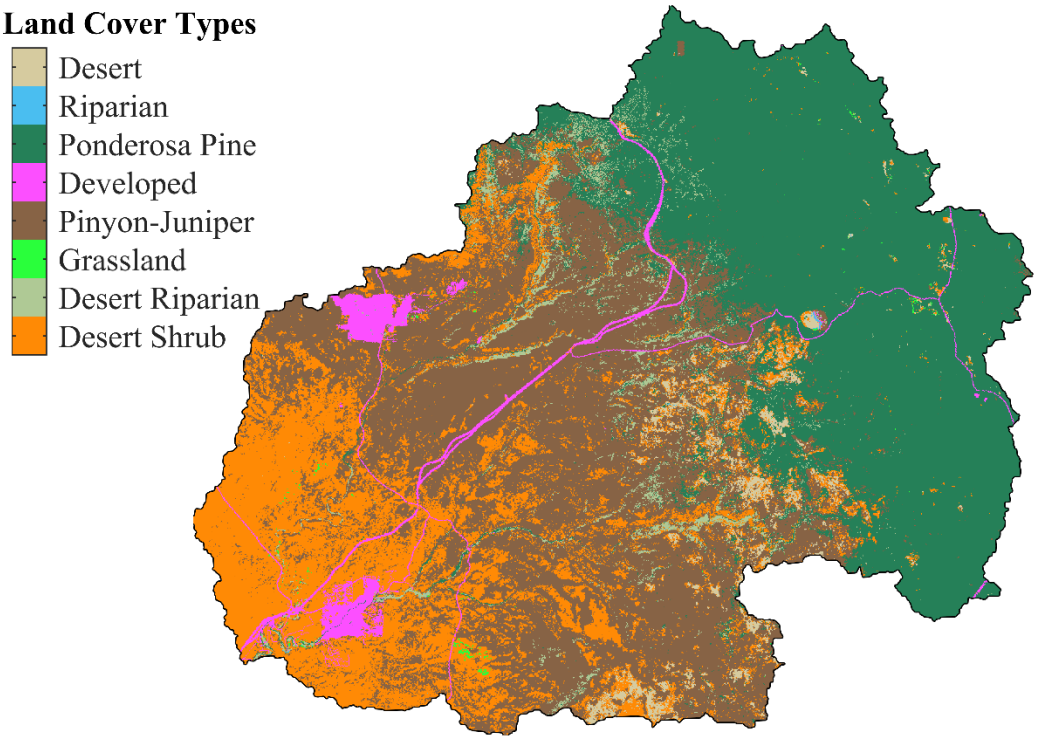

Figure 4. Map of land cover types with 30 m raster cells in Beaver Creek watershed from LANDFIRE REMAP.

The main improvement of LANDFIRE REMAP over previous versions are continuous distributions of vegetation fraction and vegetation height. Previous versions of LANDFIRE provided these in ~10 m increments of vegetation height and ~10% increments of vegetation fraction as polygons. A new base map derived from LiDAR for LANDFIRE REMAP provides raster values at <1 m resolution at increments of 1% for vegetation height and fraction, respectively. To take advantage of these improvements, these new products were incorporated into the Beaver Creek model. The maps for these vegetation parameters are provided in Figure 5.

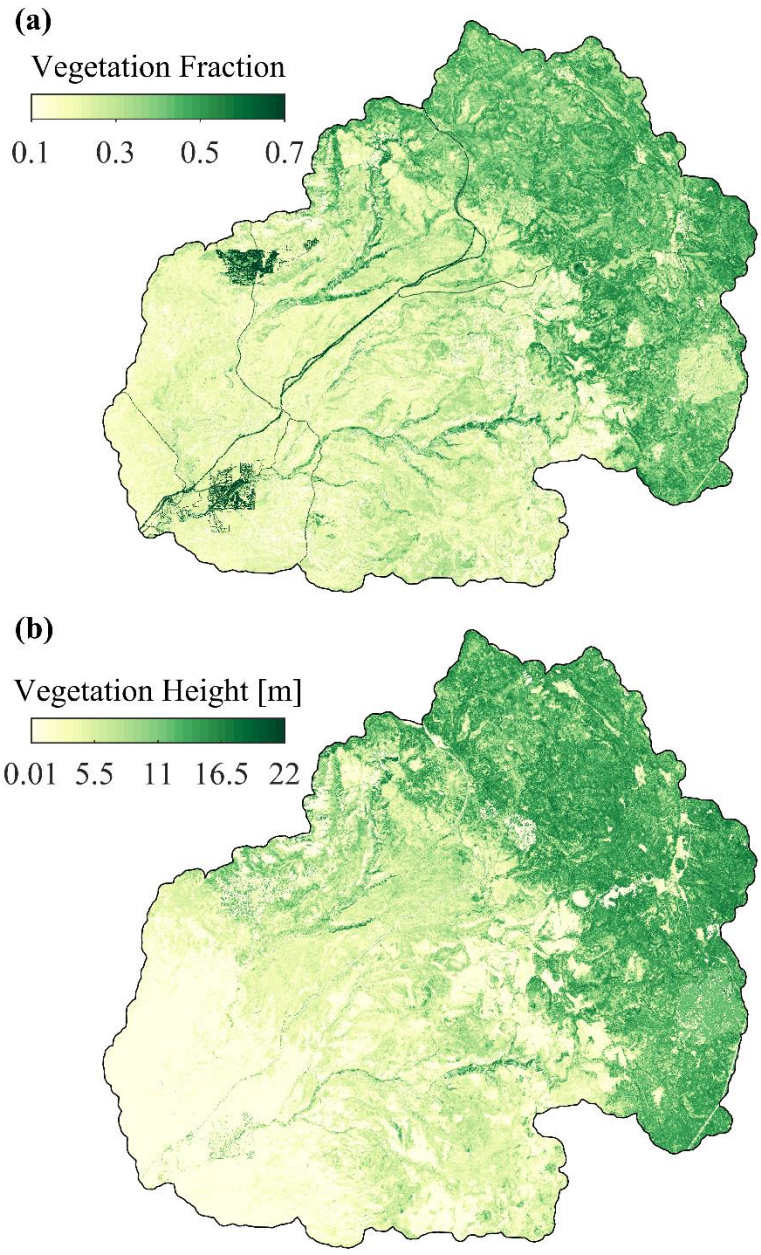

Figure 5. Maps of (a) vegetation fraction and (b) vegetation heights in 30 m raster cells in the Beaver Creek watershed from LANDFIRE REMAP.

There is a section in southeast corner of the watershed within the ponderosa pine forest originally classified as a burned area with reduced vegetation height and fraction. Imagery from the same time period as the maps did not show this area to be different than

the surroundings. Thus, due to the importance of vegetation height on snowpack dynamics, vegetation height in this area was adjusted using linear regression. The linear regression was created by selecting a region close to the burned area of the same area coverage. Then, using vegetation height as the predictand and vegetation fraction as the predictor for the regression, the vegetation height in the burned was adjusted to what is shown in Figure 5. The land use, vegetation height, and vegetation fraction maps were converted into the arcgrid format using MATLAB which can be read by the model.

2.2.5 Bedrock

Depth to bedrock provides a lower model boundary condition at the bottom of the soil column. In the original application of Hawkins (2012), the bedrock information from the SSURGO dataset were increased during the model calibration process. A model physics update completed in this study allowed for a more realistic use of depth to bedrock. Furthermore, a newer version of soil information that combines multiple datasets known as gNATSGO has since been released (Soil Survey Staff, 2020). This new updated bedrock map was used for the Beaver Creek application as shown in Figure 6 which represents the depth from the soil surface to bedrock in meters.

The depth bedrock map in Figure 6 generally corresponds with the soil classes shown in Figure 3. Due to the way the depth to bedrock is measured, certain sections of the watershed had missing data and are represented as bedrock depths greater than 2 meters. The data was modified such that depths greater than 2 meters were set to 2 m.

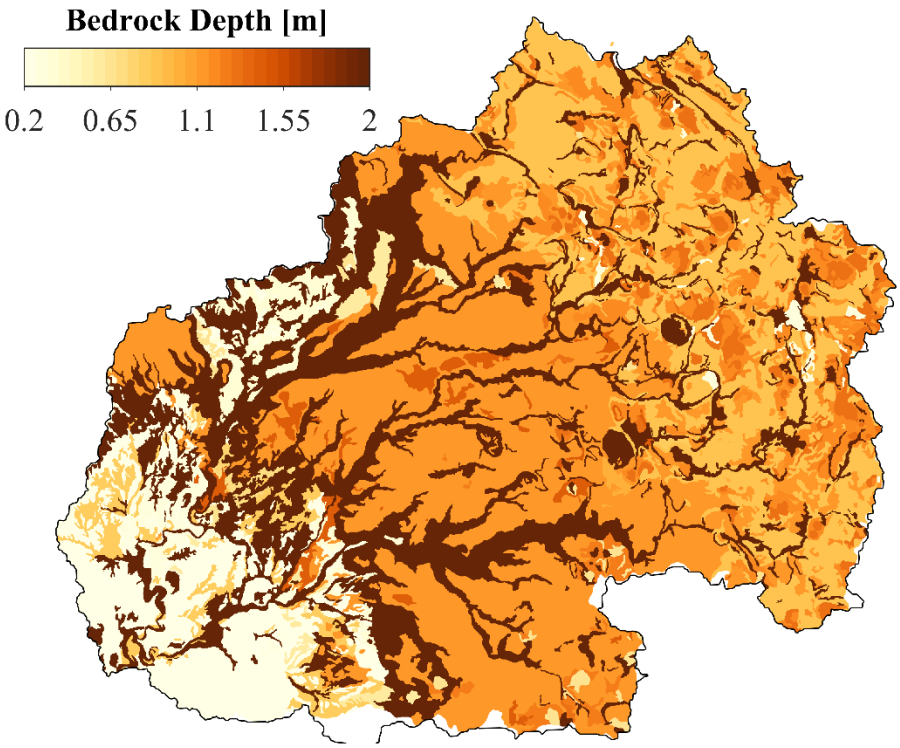

Figure 6. Map of depth to bedrock for the Beaver Creek Watershed from gNATSGO.

2.2.6 Streamflow

There are three active stream gauges within the BCW, with their spatial locations shown in Figure 1. The gauges on the WBC and DBC are funded in part by the Salt River Project and Arizona Department of Water Resources and maintained by the USGS. These two gauges are the main streamflow observations used for model calibration. The data is acquired from the USGS National Water Information Service (U.S. Geological Survey, 2016). The stream gauge at the outlet of the Beaver Creek watershed near Camp Verde, Arizona was taken over by the National Park Service (NPS) around 2010. The data before this period is sparsely available from Hawkins (2012). The streamflow records for after the year 2010 were acquired from an NPS staff member, but a rating curve for the

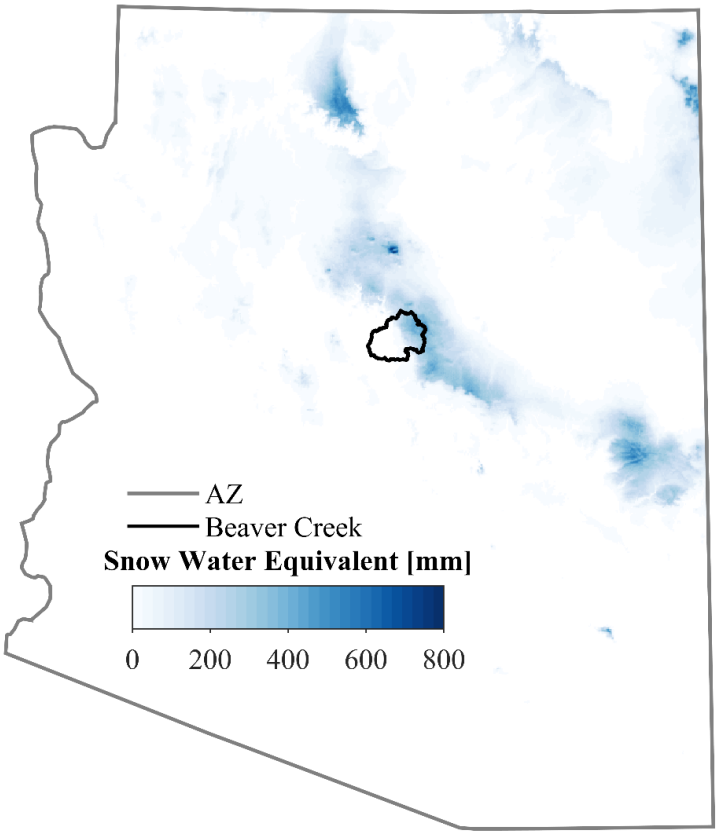

Figure 7. Daily map of SWE from SWANN on February 23, 2008, for the state of Arizona based on the Salt River Project private version of SWANN at 1 km resolution.

site has not been properly maintained (personal communication, August 9, 2019). Streamflow values above 1 m^3/s are considered inaccurate and there are large periods of missing data. Thus, the study excluded records from the outlet stream gauge and only used the WBC and DBC for calibration of the model.

2.2.7 Snow Water Equivalent

High temporal resolution and spatially distributed measurements of snow depth or snow water equivalent (SWE) in the United States are limited to specific circumstances such as field campaigns (Broxton et al., 2016). Snow pillow measurements such as the

previously described SNOTEL lack the high spatial resolution that distributed models are able to simulate. Remote sensing methods that estimate snow extent or snow-covered area are available daily at high spatial resolutions but lack the ability to provide information about volume. To address these issues, researchers at the University of Arizona combined different observational datasets (SNOTEL and Cooperative Observer Network) with precipitation and air temperature forcings from PRISM to construct gridded SWE across the entire continental US (Broxton et al., 2016). The result is a daily, 4 km resolution dataset, available publicly from the National Snow and Ice Data Center for water years 1982-2020 (Broxton, 2019b). for specific applications in Arizona, the Salt River Project funded these researchers to conduct an extensive snow survey campaign in northern Arizona at two 100 km^2 sites where ground measurements like snow density along with LiDAR and satellite imagery were used to train an artificial neural network (Broxton et al., 2017). The artificial neural network was then used to downscale the original SWE dataset based on topography and other land surface characteristics to a 1 km resolution for the state of Arizona, now called Snow Water Artificial Neural Network (SWANN). The ANN was able to represent the two study sites well but extending the ANN model to the watershed scale led to biases in SWE of up to 30%, due to the high spatial variability of snow density (Broxton et al., 2019). An example of the SWANN product is shown in Figure 7 on the day of maximum SWE for the Beaver Creek watershed in the 2008 water year. This product is a very useful tool for this work due it's continuous record and the high spatial resolution which allows basin scale calibration of SWE at temporal and spatial scales.

3 METHODOLOGY

3.1 Precipitation Bias-Correction

Using the five rain gauges with quality controlled daily data provided by SRP staff, bias-correction of NEXRAD Stage IV data was completed using methods from Hussein (2020). Climatological monthly average precipitation for water years 2002-2018 was computed for the five stations and each of the NEXRAD raster cells that fall within the BCW boundary. The known station elevations shown in Table 2 along with the elevations of the NEXRAD raster cells, found by resampling the 1/3 arc-second digital elevation model (DEM) from the USGS were used to compute precipitation lapse rates. Lapse rates were estimated using linear regressions for each month of the year with precipitation as the predictand and elevation as the predictor. The lapse rates for a month during the cold and warm season (January and July) are provided in Figure 8. The gauge lapse rates for warm season months are closer to the raw NEXRAD data, while the cold season months like January and February showed large differences at higher elevations. The latter spurred the implementation of a bias-correction method that account for elevation differences in precipitation.

The bias-correction procedure has two steps: (1) adjust NEXRAD based on station lapse rates for the entire BCW, and (2) adjust NEXRAD based on monthly totals of areal precipitation at the stations and co-located raster cells. The bias-correction procedure is outlined below:

$$P_{y,m}(z) = P_{N,y,m} * \gamma_m(z) * \omega_{y,m}, \quad (1)$$

where $P_{y,m}$ is the bias-corrected precipitation for year, *y*, and month, *m*, at elevation, *z*. $P_{N,y,m}$ is the raw NEXRAD precipitation for year, *y*, and month, *m*, at elevation, *z*. $\omega_{y,m}$ is the total monthly precipitation correction factor for year, *y*, and month, *m*. The correction factor based on precipitation lapse rates, γ_m is the lapse rate weight for month, *m*, at elevation, *z*. The monthly precipitation weight is calculated as follows:

$$\gamma_m(z) = \frac{a_{g,m} + b_{g,m} z}{a_{N,m} + b_{N,m}\,\bar{z}}, \tag{2}$$

where $a_{g/N,m}$ and $v_{g/N,m}$ are the regression coefficients for month, *m*, from the lapse rate regressions for gauges and NEXRAD, respectively, and $\bar{z}$ is the mean watershed elevation. The second correction factor, based on total monthly precipitation is:

$$\omega_{y,m} = \frac{1}{S}\sum_{i=1}^{S} \frac{P_{g,i,y,m}}{P_{N,i,y,m}}, \tag{3}$$

where $P_{g,i,y,m}$ is the monthly precipitation for station *i* in month *m* of year *y*, S is the total number of stations, and $P_{N,i,y,m}$ is the NEXRAD precipitation in the co-located raster cell for station, *i*, month, *m*, and year, *y*. The bias-corrected monthly precipitation is disaggregated to the hourly NEXRAD precipitation based on the number of hours with zero precipitation in the month as follows:

$$P_{y,m,d,h}(z) = P_{N,y,m,d,h}(z) + \frac{P_{y,m}(z) - P_{N,y,m}}{N_{h,y,m}}. \tag{4}$$

where $N_{h,y,m}$ is the number of hours in month, *m* and year, *y* with nonzero values of precipitation. Figure 8c shows the differences in mean total monthly precipitation across 2003-2018 water years for the raw and bias corrected NEXRAD.

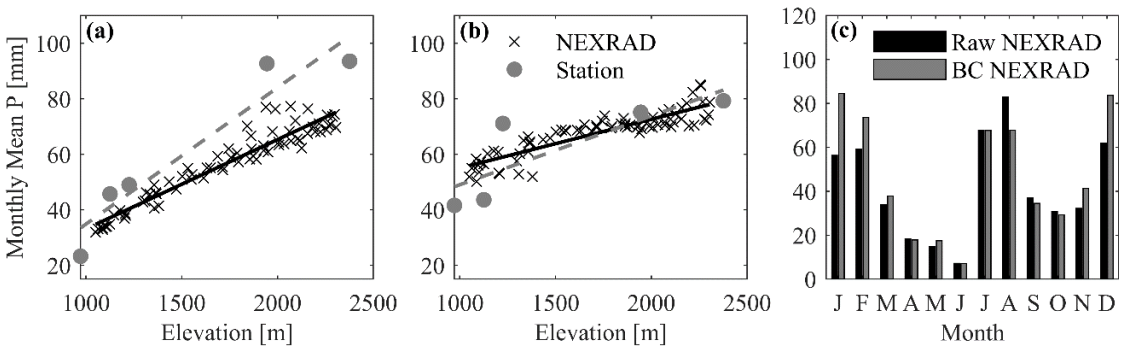

Figure 8. Monthly mean precipitation as a function of elevation from stations and NEXRAD for (a) January and (b) July over a 16 year period. (c) Monthly mean areal precipitation for the Beaver Creek from raw and bias corrected NEXRAD. Dashed and solid lines in (a) and (b) are linear regressions for stations and NEXRAD, respectively.

3.2 Meteorological Forcing Preparation

The meteorological forcing for the model was prepared using the three datasets outlined in section 2.2.2. Multiple iterations of the meteorological forcing were prepared over the course of the study. The first iteration was raw NLDAS-2 data, but the pixilation effects shown in Hawkins (2012) were undesirable. Following Ko et al. (2019), the raw NLDAS-2 was downscaled using functional relations outlined in Liston and Elder (2006b). After testing the downscaled NLDAS-2, we found air temperature was not properly represented across the watershed. The final forcing used for model simulations was prepared by downscaling gap filled station data using localized lapse rates. The details of the procedure are outlined in the following two sections.

3.2.1 Gap Filling Station Data

The station data from the five weather stations discussed in section 2.2.2 contained sections of missing or erroneous data over the 16-year period of interest.

Manual quality control of erroneous measurements like values outside of their physical limits were removed from the station time series because continuous hourly records were required for the downscaling procedure. The missing or removed data were repopulated using bias corrected NLDAS-2 data.

The bias corrected NLDAS-2 data was prepared using a method known as quantile mapping. Quantile mapping is a commonly used method of bias correcting when downscaling global climate models that uses the statistical distribution of two datasets (Cannon et al., 2015). First, hourly time series of the co-located NLDAS-2 raster cells were extracted from the raster grids. Any missing data from the station timeseries is also removed from NLDAS-2. After the two timeseries are obtained, the bias correction is completed using the following equation:

$$x_{BC,h,d,m,y} = F^{-1}\left[F\left(x_{NLDAS,h,d,m,y}, X_{NLDAS,m}\right), X_{Obs,m}\right] \quad (5)$$

where $x_{BC,h,d,m,y}$ and $x_{NLDAS,h,d,m,y}$ are the bias corrected and raw NLDAS variable value for hour, *h* of day, *d* of month, *m* of year *y*, respectively. $X_{NLDAS,m}$ and $X_{Obs,m}$ are the raw NLDAS and station variable values of month *m*, respectively. *F* is the empirical cumulative distribution function using the Hazen-Williams plotting position and F^{-1} is the inverse of *F*. The method outlined in equation 5 fits a distribution to the meteorological variable for NLDAS observations for a given month. Then the cumulative probability for a NLDAS data point is found from the NLDAS distribution. The cumulative probability is used to find the corresponding variable value from the observation distribution. In short, quantile mapping transforms the statistical distribution of NLDAS to be more similar the observations. After the bias correction was completed, missing or erroneous data from stations is populated with bias corrected values.

3.2.2 Localized Lapse Rates & Downscaling

The spatial interpolation methodology used here to interpolate weather station data into gridded meteorological data requires air temperature lapse rates. Initially, monthly air temperature lapse rates from the literature were used, but after further examination the local lapse rates for Beaver Creek in winter months were found to be significantly different from published values. Localized lapse rates for the Beaver Creek watershed were computed using PRISM. To compute these lapse rates, average monthly air temperature for each of the PRISM raster cells that fall within the Beaver Creek watershed were extracted for water years 2003 to 2018. In addition, a 1/3 arc-second DEM from the USGS was aggregated to the 4 km resolution of PRISM for the raster cell elevations. Using simple linear regression, lapse rates were computed for each month of the year, with the regression coefficients show in Table 5. Additionally, Figure 9 illustrates the differences in lapse rates from literature (Liston and Elder, 2006b) and the localized rates from PRISM for a winter and summer month.

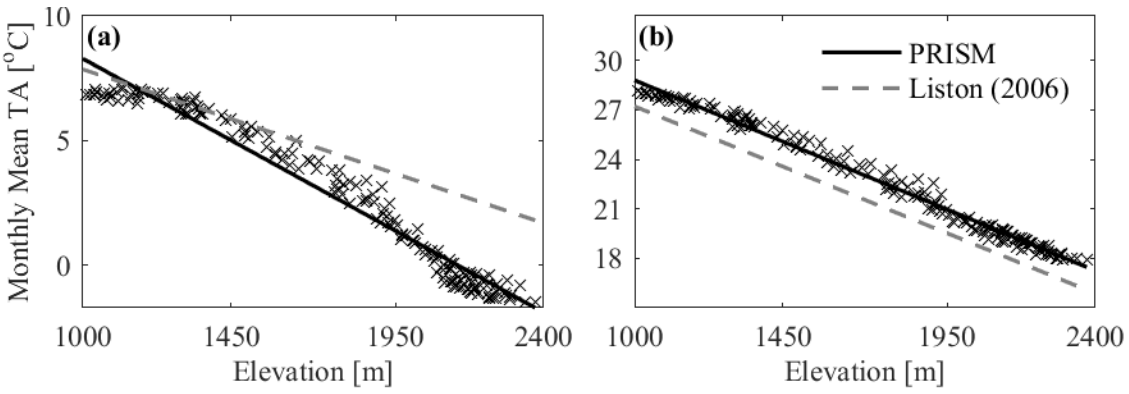

Figure 9. Comparison of air temperature lapse rates for (a) January and (b) July from PRISM and Liston and Elder (2006b). Symbols corresponds to average air temperature for each raster cell from PRISM that are located within the Beaver Creek watershed.

Table 5. Coefficients of regression derived from linear regression of monthly average air temperature and elevation of PRISM raster cells. The regression equation follows the form: $TA = aZ + b$ where TA is the air temperature and Z is the elevation.

Month	***a* [ºC]**	***b* [ºC/km]**
Jan	15.6	-7.27
Feb	17.7	-7.76
Mar	20.7	-7.90
Apr	24.5	-8.20
May	29.4	-8.47
Jun	34.3	-8.22
Jul	37.0	-8.25
Aug	36.2	-8.36
Sep	33.0	-8.35
Oct	26.7	-7.97
Nov	19.8	-7.34
Dec	14.6	-6.78

Following methods outlined in Liston and Elder (2006b), the gap filled weather station data was downscaled into hourly raster grids at a 1 km resolution. While the methodology allows downscaling to whatever resolution is desired, 1 km was chosen as a middle ground between capturing terrain features and avoid portraying detail that does

not exist in the base forcing. Detailed information on the equations for the downscaling procedure are presented in Liston and Elder (2006b). The procedure contains two general steps. First, station data at every step is spatially interpolated across the domain using the Barnes objective analysis scheme (Barnes, 1994; Koch et al., 1983) to create gridded meteorological data. Second, a set of equations that ingest topological data in the form of elevation, slope, and aspect are applied to adjust the gridded data. The second step is where the localized air temperature lapse rates are incorporated. Air temperature is also used in the adjustment of other variables such as relative humidity. The topological data used the second step are based on the 1/3 arc-second DEM resampled to 1 km. The resampling and calculation of slope and aspect were completed in ArcGIS.

3.3 Simulation Experiments

Model experiments were completed by applying a set of simple climate change experiments and adjusted vegetation inputs that represent the change in forest properties due to forest thinning. An outline of the model experiments is presented in Table 6. It should be noted that the goal of these experiments is not to provide an exact representation of future conditions but instead to provide insight into the sensitivity of hydrologic processes in the Beaver Creek watershed to these disturbances.

Table 6. Summary of model simulation experiments with acronyms and descriptions.

Scenario	Acronym	Description
Base Case	BC0	No forest treatment or warming with calibrated parameters
Base Case + Warming	BC1, BC2, BC4, BC6	No forest treatment and +1, 2, 4, 6^{o}C of warming with calibrated parameters
Post Treatment	PT0	Forest treatment, no warming with calibrated parameters
Post Treatment + Warming	PT1, PT2, PT4, PT6	Forest treatment and +1, 2, 4, 6^{o}C of warming with calibrated parameters

3.3.1 Climate Change

A set of climate change experiments were constructed that represent the general increases in global temperature from the range of emission scenarios in Coupled Model Intercomparison Project Phase 5 (CMIP5) (IPCC, 2013). Specifically, CMIP is a project developed by the World Climate Research Program to look at projections of future climate and CMIP5 is the 5th phase of the project. CMIP5 contains four scenarios of potential future emissions of greenhouse gases called representative concentration pathways (RCP). Each of these scenarios has a standardized set of emissions that are used to force general circulation models (GCM). For this study, we used the general range of global mean surface temperature increases from long-term simulations up to 2100, +1 to +6°C to modify the original model forcing developed for the model calibration. To do so, the temperature changes outlined in Table 6 were added to the hourly air temperature forcing as a change factor. This method has been used in the past (Nemec and Schaake, 1982; Xu and Halldin, 1997; Zhang et al., 2013; Liu et al., 2019) and is a simple upward

shift in the diurnal cycle of air temperature. Changes in other meteorological variables such as relative humidity or precipitation were not considered in this study.

3.3.2 Forest Thinning

Forest thinning was conducted to examine the aggregated impact of changes in forest structure. Research has shown that the patchy distribution and degree of canopy closure in ponderosa pine forests play an important role in hydrologic dynamics (Moir et al., 1997). However, incorporating these distinct features into the model were outside of the study scope. The methodology applied here uses data from multiple sources to derive modified vegetation parameter values to the model that mimic the effect of thinning.

Spatially distributed data of pre- and post-treatment basal area for areas in and around Beaver Creek were provided by 4FRI staff as a shapefile (personal communication, May 9, 2020). Pre-treatment conditions from the 4FRI dataset are based on forest stand estimates from 2010. The post-treatment conditions are a model output from the Forest Vegetation Simulator (FVS) using the pre-treatment conditions and treatment type as an input (Crookston et al., 2005). The data provided by 4FRI staff only covers the ponderosa pine forest within the Dry Beaver Creek as the Beaver Creek lies on the boundary of two separate phases of the 4FRI study. The pre- and post-treatment distribution of basal area from the 4FRI data is shown as the black and red lines in Figure 10. A separate dataset from Wilson et al. (2013) provides basal area as rasters at 250 m resolution for different tree species, derived using field plot measurements and satellite imagery. As the ponderosa pine basal area, shown in Figure 11, from Wilson et al. (2013) represents conditions from 2011 the dataset was treated as pre-treatment conditions in the

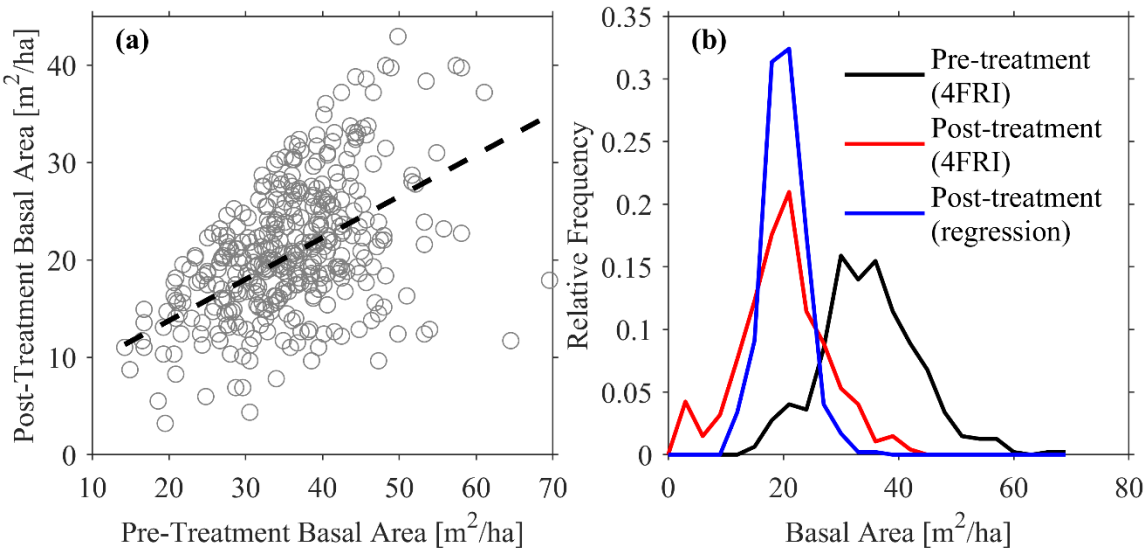

Figure 10. (a) Scatter plot of pre- and post-treatment basal area from 4FRI dataset with a dashed line showing the linear regression. (b) Relative frequency distributions of basal area from 4FRI and linear regression.

study. In order to acquire post-treatment basal area as a raster, a simple model was developed to relate pre- and post-treatment basal area from the 4FRI dataset using linear regression, shown in Figure 10.

Figure 10b highlights the differences between the distribution of basal area in the pre- and post-treatment dataset from 4FRI. It also shows the general ability of the linear regression to model the post-treatment 4FRI data, but it does not capture the tails of the distribution. In addition to linear regression, three methods of curvilinear regression were examined (exponential, power law, and 2nd order polynomial). All four regression methods produced similar results with Pearson correlation coefficients approximately equal to 0.5. Next, the linear regression was applied to the pre-treatment basal area raster in order to get a raster of pre-treatment basal area. Following 4FRI standards outlined in Hampton et al. (2011), basal area values less that approximately 12 m^2/ha (52 ft^2/ac) were

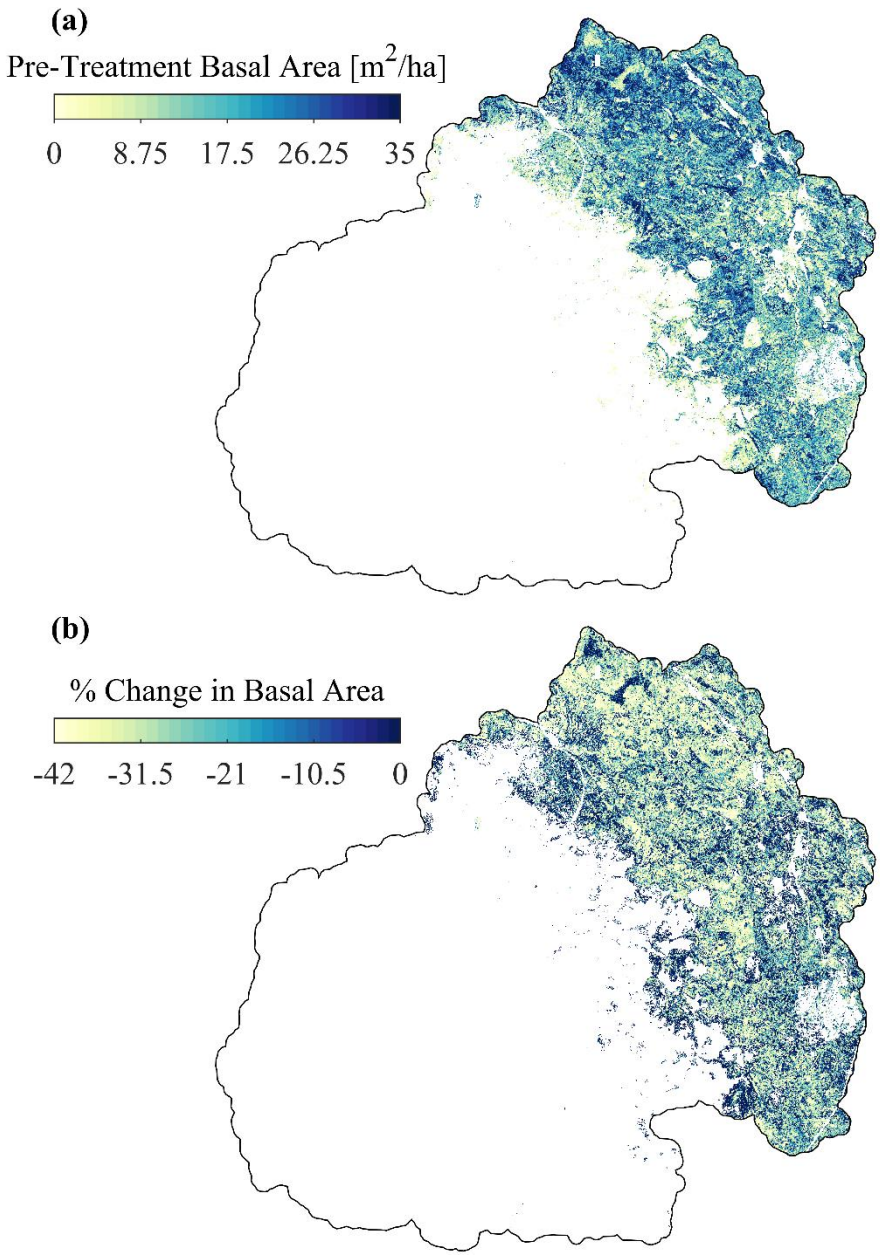

Figure 11. (a) Pre-treatment basal area for the ponderosa pine forest in the Beaver Creek at 30 m resolution. (b) Percent change in ponderosa pine basal area from modeled forest thinning using linear regression.

not thinned. For example, Robles et al. (2014) documented a set of constraints to forest thinning such as areas with extreme slopes, erodible soils, protected wildlife habitats, and wildland-urban interface zones in the Salt-Verde River watershed. The latter constraints

were found to have little to no impact on the total amount of thinned forest in regard to the Beaver Creek and were not accounted for. The result from this work is shown in Figure 11b with the percent change in basal area from the modeled forest thinning.

Following Moreno et al. (2016), basal area maps along with empirical relations were used to calculate vegetation parameters that represent pre- and post-treatment conditions. The functional forms of the empirical relationships are outlined below:

$$VF = \frac{BA + 2.794}{2.898}, \tag{6}$$

where *VF* is the vegetation fraction (%) and *BA* is the basal area in ft^2/acre. This relation was derived in Moreno et al. (2016) from data presented in Hampton et al. (2011). Similarly, the empirical relation for leaf area index (LAI) was developed with field measurements in Moreno et al. (2016):

$$LAI = |-0.00003738369BA^2 + 0.01683112155BA - 0.03539819521|, \tag{7}$$

where *LAI* is a unitless parameter that accounts for the area that the canopy leaves cover in relation to the ground surface area. Based on LAI, tRIBS model parameters such as free throughfall coefficient, canopy storage capacity, and optical transmission coefficient were calculated. Free throughfall coefficient is calculated following Pitman (1989):

$$p = \exp(-1.5LAI), \tag{8}$$

The free throughfall coefficient controls the fraction of liquid precipitation that is not captured by vegetation. Canopy storage capacity is calculated following Pitman (1989):

$$S = 0.5LAI, \tag{9}$$

The canopy storage capacity controls the maximum amount liquid precipitation that can be held within the vegetation canopy. Optical transmission coefficient is calculated following the Beer-Lambert Law:

$$k_t = \exp(-kLAI), \quad (10)$$

where *k* is the canopy extinction coefficient. The value for *k* used in this study is 0.45 for needle leaf plants (Zhang et al., 2014). Using these equations, VF, LAI, p, S, and k_t maps were created for both pre- and post-treatment. Although tRIBS accepts spatially distributed vegetation inputs, the parameter raster were not directly substituted into the model for two main reasons. First, the Beaver Creek model only uses distributed vegetation data for *h* and *VF*, the other parameters are single values based on land cover polygons. To account for this, the parameter rasters were averaged across the land cover polygons for ponderosa pine. Second, as described in section 2.2.4, there are key vegetation parameters that control the snow model simulations which we wanted to have the ability to calibrate. The calibrated vegetation parameters (Table 10) and *VF* raster were treated as pre-treatment conditions as none of the proposed forest thinning has been completed by 4FRI. To calculate the post-treatment vegetation parameters, ratios between post- and pre-treatment parameter values were calculated. The ratios, referred to as change factors, were multiplied by the calibrated parameters to get the post-treatment parameters. *VF* follows a modified procedure in that change factors were computed for each raster cell of the vegetation fraction grids computed using equation 6 and multiplied against the *VF* grid displayed in Figure 5. The post-treatment vegetation parameter values for LAI, p, S, and k_t along with the change factors are shown in Table 16 and the post-treatment raster of *VF* is displayed in Figure 12.

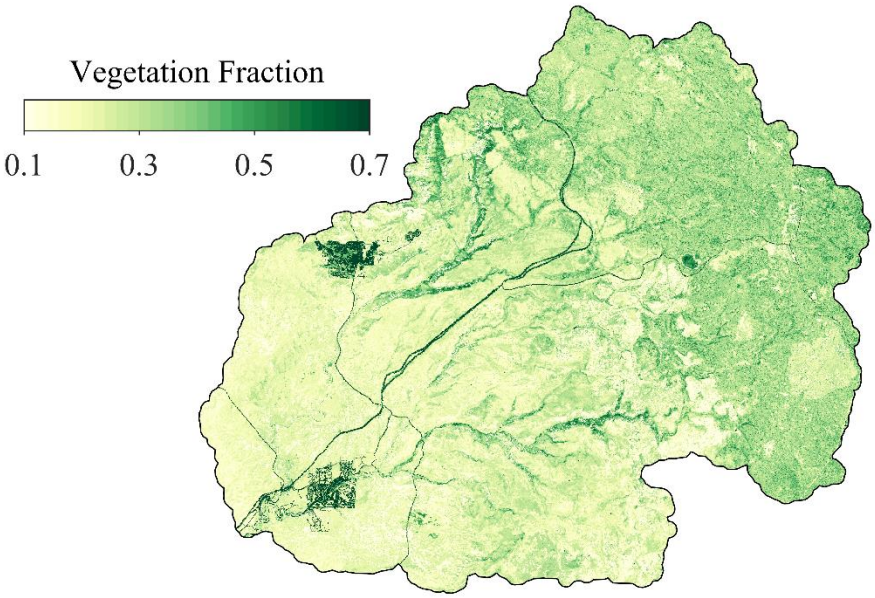

Figure 12. Map of vegetation fraction after thinning in the ponderosa pine forest.

3.4 tRIBS Model Overview

The TIN-based Real-time Integrated Basin Simulator is a fully-distributed, physically-based hydrologic model that was developed at the Ralph M. Parsons Laboratory at the Massachusetts Institute of Technology. tRIBS possess capabilities that makes the model an attractive alternative to other hydrologic models developed in the research community. For example, tRIBS model domains are based on Voronoi polygons derived from a Triangulated Irregular Network (TIN) which allows a variable resolution across the model domain. In Vivoni et al. (2004), the authors developed an algorithm that places focus on areas of importance to hydrologic processes. The latter allows for high resolution in and around stream channels, while having a lower resolution in areas of low slope, significantly speeding up computational time in watersheds larger than 1000 km^2 (Hawkins, 2012). The formulation of tRIBS allows for simulating channel transmission,

plant interception, evapotranspiration, soil moisture dynamics, and runoff production. The capabilities of tRIBS were expanded in Rinehart et al. (2008) who implemented a single-layer snow model that accounts for topographic effects on snow processes.

The tRIBS model representing the Beaver Creek was initially developed by Hawkins (2012) with the computational domain consisting of approximately 78,000 voronoi polygons that represent the domain with an average resolution of 120 m^2. Due to the high resolution and size (1100 km^2) of the Beaver Creek model was separated into 52 different subbasins based on the reach partitioning scheme for parallel simulations (Vivoni et al., 2011). Parallel simulations were completed on the Agave High Performance Computing Cluster (HPCC) at Arizona State University. The total length of real-world time for each 16 year simulation on Agave took approximately 30 hours with an additional 18 hours to merge the spatial outputs using Perl and processing the model outputs using Matlab all completed on Agave.

Due to the emphasis of this work a detailed overview of the tRIBS snow model is provided along with general overviews of runoff production and infiltration, canopy interception of rainfall, evapotranspiration, and the energy balance. For details on the groundwater and channel routing models implemented into tRIBS the reader is referred to Ivanov et al. (2004) for a detailed description of these components.

3.4.1 Snowpack Model

The distributed snow model implemented in tRIBS is a single layer, energy and mass balance model. The model was developed by assembling components of multiple different snow models (Rinehart et al., 2008). Snow simulations begins with the

determination of precipitation phase, a portion of snowfall can be intercepted in the canopy which follows a mass balance with snow unloading controlled by air temperature. Snowfall onto the ground surface will form snowpacks that contain both solid and liquid precipitation. Snowpack ablation can occur through melt, sublimation, or evaporation based on the energy balance and the amount of liquid water in the snowpack. A detail description of these processes is described in the following sections.

3.4.1.1 Governing Equations

The snowpack energy balance in the distributed snow model is a combination of Wigmosta et al. (1994) and Tarboton and Luce (1996). The state equations that control the snowpack mass balance is as follows:

$$\frac{dW_i}{dt} = P_i + F_i + M_{ji}, \tag{11}$$

$$\frac{dW_j}{dt} = P_j + F_j + M_{ij} - R_{liq}, \tag{12}$$

where *i* and *j* refer to the phases ice and liquid respectively, W is the water equivalent in phase *i* or *j*, *P* is the precipitation falling as phase *i* or *j*, *F* is the turbulent flux that is either sublimation for phase *i* or evaporation for phase *j*, *M* is the water equivalent that transformed from one phase to the other in the snowpack, and R_{liq} is the amount of liquid water routed from the snowpack. The state equation that controls the development of internal energy in the snowpack is as follows:

$$\frac{dU}{dt} = L + H + P + R_S + R_L^{in} + R_L^{out}. \tag{13}$$

where U is the internal energy of the snowpack, L is the latent heat flux, H is the sensible heat flux, P is the precipitation heat flux, R_S is the incoming shortwave radiation, R_L^{in} is

the incoming longwave radiation, and R_L^{out} is the outgoing longwave radiation. The calculation of the variables above will be discussed in the following sections.

3.4.1.2 Precipitation and Snow Ablation

Snow model simulation begins with the determination of the precipitation phase falling to the surface. The methods for determining precipitation phase are known as phase partitioning methods (PPM). These methods use the meteorological conditions at the land surface for determining phase. A variety of PPM exist for snow models, the simplest being a single temperature threshold that separates rain and snow. The methods increase in complexity from a two-temperature threshold that accounts for a mixture of rain and ice (Wigmosta et al., 1994) to methods that use relative humidity and air temperature to compute the wet bulb temperature (Wang et al., 2019). The PPM used in the model is intermediate in complexity, where precipitation is linearly portioned between two temperature thresholds:

$$f_s = \begin{Bmatrix} 1, if\ T_a < T_s \\ 0, if\ T_a > T_r \\ \dfrac{T_a - T_s}{T_r - T_s}, otherwise \end{Bmatrix}. \quad (14)$$

where f_s is the fraction of precipitation that is snow, T_s (°C) is the temperature below which all precipitation is snow, and T_r (°C) is the temperature above which all precipitation is liquid. Default values for these thresholds in tRIBS are -1.1 and 3.3 (°C) for T_s and T_r respectively (Allard, 1957).

Water can leave an established snowpack in the form of liquid routed to the ground surface, sublimated from snow to vapor, or evaporated from liquid to vapor.

Liquid water is routed out of the snowpack if its amount exceeds the liquid water holding capacity of the snowpack, following Wigmosta et al. (1994):

$$R_{liq} = W_{liq} - \varphi_{liq} W \;\; if \;\; W_{liq} > \varphi_{liq} W. \tag{15}$$

where W_{liq} is the depth of liquid water in the snowpack, φ_{liq} is the liquid water holding capacity, W is the snow water equivalent of the snowpack, and R_{liq} is the depth of the liquid water being routed to the ground surface. The default value for φ_{liq} is 0.06, but this value ranges widely based on snowpack characteristics like density (Goto et al., 2012). Sublimation and evaporation from the snowpack is controlled by the latent heat flux, the calculation of which is shown in equation 17. Sublimation of ice occurs if the temperature of the snowpack is below $0^o C$, conversely evaporation occurs if the snowpack temperature is above $0^o C$. This method works because for the snowpack temperature to be above $0^o C$ there must be liquid water present in the snowpack. Additionally, deposition of mass into the snowpack is possible if the necessary conditions are met. Sublimation/evaporation and deposition is calculated as follows:

$$F_i = \frac{L_i}{\rho_{liq} \lambda_i}. \tag{16}$$

where F_i is the depth of sublimation or deposition for phase i, L_i is the latent heat flux for phase i, and λ_i is the latent heat of freezing. Equation 16 is also used for the calculation of evaporation using the latent heat of evaporation.

3.4.1.3 Energy Fluxes

The snowpack energy balance, shown in equation 13, is composed of six different energy fluxes. Both the latent and sensible heat fluxes are described in Wigmosta et al. (1994):

$$L = \frac{0.622\lambda_i \rho_{air}(e(T_a) - e_s(T_a))}{P_a r_a}, \quad (17)$$

$$H = \frac{\rho_{air} c_{p,air}\ (T_a - T_a)}{r_a}. \quad (18)$$

where ρ_{air} is the density of air, $e(T_a)$ is the vapor pressure at the snow surface at air temperature T_a, P_a is the air pressure, r_{as} is the aerodynamic resistance with calculations outlined in Wigmosta et al., (1994), and $c_{p,air}$ is the specific heat capacity of air at constant pressure. Sensible heat flux, *H*, plays an important role in the total energy balance of the snowpack across a winter season. The latent heat flux, *L*, plays a less important role but controls the amount of sublimation/evaporation occurring in the snowpack. The precipitation heat flux, *P*, in equation 13 is calculated as:

$$P = \rho_{liq} P_{net}((1 - f_s)\lambda_f + f_s c_p T_a), \quad (19)$$

where P_{net} is the net precipitation after canopy interception. The last three components of the energy balance deal with incoming radiation. The model contains multiple methods of varying complexity that account for sheltering of the ground surface from incoming shortwave radiation. The method use in this study accounts for only local sheltering of shortwave radiation due to topography and vegetation. Incoming shortwave radiation at the snowpack surface is calculated as follows:

$$R_s = I_{ds} v_{local}(1 - a_{sn})\big(K_t VF + (1 - VF)\big), \quad (20)$$

where I_{ds} is the incoming direct shortwave radiation, v_{local} is the local sheltering factor, $a_{sn}$is the snow albedo, K_t is the optical transmission coefficient, and *VF* is the vegetation fraction. The local sheltering factor is calculated as a function of the Voronoi polygon slope following Dozier and Frew (1990):

$$v_{local} = 0.5 * \left(1 + cos(S)\right), \quad (21)$$

where *S* is the slope of the Voronoi polygon. Snow albedo depends on the age of the snowpack surface since the last snowfall event and the presence of liquid water in the snowpack (Wigmosta et al., 1994):

$$a_{sn} = \begin{cases} 0.85(0.94)^{N^{0.58}} & if\ W_{liq} = 0 \\ 0.85(0.82)^{N^{0.46}} & otherwise \end{cases}. \quad (22)$$

where *N* is the number of days since the last snowfall event. Incoming and outgoing longwave radiation is based on adjusted black body radiation theory where incoming longwave also account for cloud that is approximated using relative humidity (Bras, 1990). Incoming longwave radiation is calculated using gray-body Stefan-Boltzmann equation that includes adjustments that account for cloud cover based on relative humidity (Bras, 1989). Outgoing longwave radiation is calculated based on snow emissivity and temperature of the snowpack following Tarboton and Luce (1996).

3.4.1.4 Canopy Snow Model

Vegetation canopy can play an important role in snow dynamics through the interception of falling snow. The amount of intercepted snow varies widely between tree species with deciduous trees intercepting much less snow due to the loss of leaves in the fall compared to evergreen trees, such as ponderosa pines that dominate the upper elevations of the Beaver Creek watershed. The canopy mass balance is simpler the ground snowpack model, adapted from Liston and Elder (2006a):

$$I^t = I^{t-1} + L_{loading} + Q_{cs} + L_m, \quad (23)$$

where I^t is the mass of snow in the canopy at time *t*, $L_{loading}$ is the mass of snow loaded into the canopy, Q_{cs} is the mass of snow sublimated from the canopy, and L_m is the mass of snow unloaded from the canopy. The amount of snow loaded into the canopy is a function of snow already in the canopy I^{t-1} and canopy snow holding capacity, I_{max}:

$$L_{loading} = 0.7(I_{max} - I^{t-1})\left(1 - \exp\left(-\frac{P}{I_{max}}\right)\right), \quad (24)$$

The canopy holding capacity is a function of the canopy leaf area index, *LAI*:

$$I_{max} = 4.4LAI, \quad (25)$$

Leaf area index is a vegetation parameter that is unique to each vegetation class. Unloaded snow from the canopy is determined using an air temperature index method:

$$L_m = 5.8 * 10^{-5}(T_a - 273.15)\Delta t, \quad (26)$$

where Δt is the snow model timestep (1 hour). The calculation of canopy sublimation is more involved than the ground snowpack and is a function of the amount of intercepted snow in the canopy, relative humidity, and incoming shortwave radiation:

$$Q_{cs} = C_e I^t \psi_s \Delta t. \quad (27)$$

where C_e is the canopy exposure coefficient, and ψ_s is the sublimation rate loss coefficient for an ice sphere. The calculation of these two parameters is described in Rinehart et al. (2008).

3.4.2 Runoff Production and Infiltration

The soil column is characterized as a sloped, layered soil column that extends to bedrock. Layering of the soil column is not explicit and is instead characterized using anisotropy ratio for both the saturated and unsaturated zones along with a relation that

describes the decay of hydraulic conductivity with depth from the surface. Infiltration into the soil column leads to the formation of wetting fronts in the soil that can saturate the soil leading to runoff production, consumed for evaporation, routed laterally between neighboring cells, or recharge to the groundwater table. The most important of these processes to this study is the production of runoff and the role saturated hydraulic conductivity plays in controlling runoff production. For a detailed description of the other processes occurring in the soil column the reader is referred to Ivanov et al. (2004).

tRIBS simulates four main runoff generation mechanisms: infiltration excess, saturation excess, perched return flow, and ground water exfiltration. The most dominant of these types in this work are infiltration and saturation excess. Infiltration excess in the model will occur under two conditions, first is when the soil surface becomes saturated due rainfall intensity is greater than the surface saturated hydraulic conductivity. Under this condition ponded infiltration will occur which is calculated using a modified version of the Green-Ampt model (Beven, 1984):

$$q_n(N_f) = K_{eff}(N_f)\cos(\alpha) + \psi_{is}(N_f), \tag{28}$$

where $q_n(N_f)$ is the infiltration rate normal to the soil surface, N_f is the depth to the wetting front, K_{eff} is the harmonic mean of conductivity of the saturated depth, α is the slope of the soil column, and ψ_{ie} accounts for capillary forces in the soil. The dominant component behind infiltration is gravity, controlled by the conductivity. K_{eff} decays exponentially from the soil surface, calculated as follows:

$$K_{eff}(N_f) = K_{0n}\frac{fN_f}{e^{fN_f} - 1}, \tag{29}$$

where K_{0n} is the surface hydraulic conductivity, and f is the exponential decay rate. As the wetting front moves down the soil column under these conditions the rates of infiltration will no longer be controlled by the surface conductivity but the conductivity at the wetting front. This leads into second way infiltration excess runoff can occur: unsaturated infiltration at the soil surface leads to formation of a perched zone due to reduced conductivity at the wetting front:

$$q_n(N_f, N_t) = K_{eff}(N_f, N_t)\cos(\alpha) + \psi_{ie}(N_f), \tag{30}$$

where N_t is the depth to the top of the wetting front. Here, K_{eff} represents the harmonic mean of conductivity but modified to calculate the mean over wetting front depth:

$$K_{eff}(N_f, N_t) = K_{0n}\frac{f(N_f - N_t)}{e^{fN_f} - e^{fN_t}}, \tag{31}$$

If the rate of infiltration above the wetting from is large enough then the soil above the wetting front will become saturated leading to infiltration excess runoff.

Runoff production through saturation excess occurs when the wetting front reaches the ground water table and the top of wetting front is at the soil surface, also known as the fully saturated state. This runoff mechanism is less prominent in semiarid regions like the southwestern US but can still occur in areas with shallow depths to bedrock. The final two runoff generation mechanism, perched return flow and ground water exfiltration can occur with the formation a perched zone or ground water table that is near the soil surface. One case of these mechanism is if the slope is high then water will leave the soil column laterally and generated runoff on adjacent cells.

3.4.3 Surface Energy Balance

The surface energy balance plays an important role in determining the amount of evaporative moisture losses from the soil after net radiation R_n is partitioned into sensible H, latent λE, and ground G heat fluxes:

$$R_n - G = \lambda E + H, \tag{32}$$

Similar to the snowpack energy balance, net radiation is composed of three components: incoming shortwave and longwave radiation, and outgoing longwave radiation. The calculation of these three components is nearly identical to how the components are calculated in the snowpack energy balance. For more details refer to Ivanov et al., (2004). In this study the most important component of the surface energy balance is latent heat flux for its role in calculating evapotranspiration. The model has multiple different methods for determining the latent heat flux, the method used in this study is the Penman-Monteith approach (Penman, 1948; Monteith, 1965):

$$\lambda E = \frac{\Delta(R_n - G) + \gamma \frac{\rho_m \lambda_v \delta q_a}{r_a}}{\Delta + \gamma \left(1 + \frac{r_a}{r_s}\right)} \tag{33}$$

where Δ is the slope of the Clausius-Clayperon relationship, γ is the psychometric constant, r_s is the stomatal resistance, δq_a is the specific humidity deficit, and λ_v is the latent heat of vaporization. The ground heat flux is calculated using the force-restore model, outlined in Hu and Islam (1995).

3.4.4 Canopy Interception and Evapotranspiration

tRIBS contains multiple different options for representing canopy interception and evapotranspiration. The method used in this study is the canopy water balance which is based on Rutter et al. (1971) and described in the following equation:

$$\frac{dC}{dt} = (1-p)P - D - \frac{C}{S}E_p, \tag{34}$$

where *C* is the canopy storage, *p* is the free-throughfall coefficient, *D* is the canopy drainage, *S* is the canopy storage parameter, and E_p is the potential evapotranspiration. Canopy drainage is calculated using an empirical equation that represent dripping from leaves or stemflow using an exponential relationship (Shuttleworth et al., 1997). The final term in in equation 34 describes the amount of wet canopy evaporation occurring based on the potential ET and the relative amount of water stored in the canopy.

Potential evapotranspiration along with other components of evapotranspiration are calculated following Wigmosta et al, (1994):

$$E_p = E_a\left(\frac{\Delta + \gamma\left(1 + \frac{r_a}{r_s}\right)}{\Delta + \gamma}\right), \tag{35}$$

where E_a is the actual evapotranspiration computed from the latent heat flux in equation 33. Using potential evapotranspiration, the soil evaporation and canopy transpiration are computed. The soil evaporation, E_s, takes on the following functional form:

$$E_s = (1-v)\beta_e E_p, \tag{36}$$

where β_e is the soil moisture stress. β_e represent the amount of soil moisture in the upper layer of the soil column, calculated using the following relationship:

$$\beta_e = \min\left(1, \frac{\theta_{100}}{0.75\theta_s}\right), \tag{37}$$

where θ_{100} is the soil moisture in the top 100 mm of the soil column, and θ_s is the soil moisture at saturation. The canopy *ET* has two components, transpiration, E_{dc}, and evaporation from the wet canopy E_{wc}. Evaporation rates are controlled by potential ET and the amount of water stored in the canopy:

$$E_{wc} = \begin{Bmatrix} vE_p \ \ if\ C \geq S \\ \dfrac{vE_pC}{S} \ \ if\ 0 \leq C \leq S \end{Bmatrix}, \tag{38}$$

Transpiration rate from the canopy is calculated as follows:

$$E_{dc} = \beta_t v(E_P - E_{wc}) \left[\frac{\Delta + \gamma}{\Delta + \gamma \left(1 + \frac{r_{as}}{r_s}\right)} \right], \tag{39}$$

where β_t represents the current soil moisture stress in the root zone (top 1 m). β_t controls the amount of transpiration that occurs and is a function of soil properties:

$$\beta_e = \min\left(1, \frac{\theta_{top} - \theta_r}{0.75\theta_s - \theta_r}\right). \tag{40}$$

where θ_{top} is the soil moisture in the top 1 m of the soil column, and θ_r is the residual soil moisture.

4 RESULTS AND DISCUSSION

This chapter begins by outlining the model calibration and validation procedure. First, an overview is presented of the calibrated soil and land cover parameters and the role that those parameters have in controlling the model results is discussed. Then the results from point scale modelling at two SNOTEL stations are presented along with a discussion of the snow model parameters and their importance for the basin scale modelling. Next, the model calibration and validation results are presented from basin scale modelling in the Beaver Creek over the 16 year simulation period and compared to estimates of SWE and streamflow observations. Additionally, an examination of model performance and the influence of cascading effects that the model forcings have on the simulation of hydrologic processes. The calibrated model is then used to assess an additional nine simulation experiments encompassing climate change and forest thinning.

4.1 Model Calibration and Validation

The calibration procedure starts with long-term point scale simulation at the Happy Jack SNOTEL to derive an initial set of snow model parameters which are then applied as model verification at Bar-M SNOTEL. Subsequently, calibration in the Beaver Creek was broken down into two main components: snowpack and streamflow model calibration. As shown in section 3.4.1, the connection between snowpack and streamflow processes in tRIBS is the linkage of snowmelt and the soil column surface. In order to properly calibrate streamflow, the snowpack model must be calibrated first. Furthermore, calibration and validation were broken down into two seasons, cold and warm seasons (November to April and May to October, respectively). These seasons are defined by the months with consistent snow coverage or lack thereof over the historical record.

Table 7. tRIBS soil parameter descriptions.

Parameter	Description	Units
K_s	Saturated Hydraulic Conductivity	[mm/hr]
θ_s	Soil Moisture at Saturation	[ ]
θ_r	Residual Soil Moisture	[ ]
λ	Pore distribution index	[ ]
ψ	Air Entry Bubbling Pressure	[mm]
f	Decay parameter	[mm^{-1}]
a_s	Saturated Anisotropy Ratio	[ ]
a_u	Unsaturated Anisotropy Ratio	[ ]
N	Porosity	[ ]
k_s	Volumetric Heat Conductivity	[J/msK]
C_s	Soil Heat Capacity	[J/m^3K]

4.1.1 Soil Parameters

tRIBS requires a set of 11 soil parameters to describe the soil classes in the Beaver Creek (Figure 3). Most importantly, the soil parameters control the amount of vertical infiltration into the soil along with lateral fluxes of water in the saturated and unsaturated zones. Soil parameters also constrain the amount of evapotranspiration that can occur through soil moisture since both soil evaporation and plant transpiration depend on the water availability. Soil parameters in tRIBS are shown in Table 7.

Due to the extensive efforts of establishing the Beaver Creek model by Hawkins (2012), the initial parameter values for all soil classes, key parameters that control watershed runoff, and dominant soil classes were already established. Nevertheless, alterations made to the meteorological forcing, land cover classification, and bedrock depth along with the incorporation of cold season processes required that additional calibration of soil parameters be completed. The 13 soil classes and their respective parameter values are presented in Table 8.

Table 8. Soil parameter values for the Beaver Creek watershed. Soil classes that span both Wet and Dry Beaver Creek were separated into unique types for each watershed.

	Soil Parameters										
	K_s	θ_s	θ_r	λ	ψ	f	a_s	a_u	N	k_s	C_s
Silty Loam	36.3	0.42	0.07	0.3	-15	0.01	300	900	0.49	0.7	1400000
Clay Loam (WBC)	22.3	0.39	0.08	0.35	-11	0.01	300	900	0.47	0.7	1400000
Unweathered Bedrock (WBC)	2.5	0.4	0.1	0.3	-7.5	0.01	300	900	0.48	0.7	1400000
Sandy Loam	65	0.41	0.05	0.4	-15	0.01	300	900	0.46	0.7	1400000
Clay (WBC)	3	0.4	0.1	0.35	-7.5	0.04	300	900	0.48	0.7	1400000
Water	3.2	0.51	0.1	0.4	-15	0.01	300	900	0.61	0.7	1400000
Loamy Sand	45	0.41	0.05	0.4	-15	0	300	900	0.46	0.7	1400000
Sand	106	0.42	0.02	0.4	-15	0.01	300	900	0.44	0.7	1400000
Silty Clay Loam	3.2	0.51	0.1	0.4	-15	0.01	300	900	0.61	0.7	1400000
Clay Loam (DBC)	22.3	0.39	0.08	0.35	-11	0.01	300	900	0.47	0.7	1400000
Clay (DBC)	3	0.39	0.09	0.4	-7.5	0.02	300	900	0.48	0.7	1400000
Unweathered Bedrock (DBC)	2	0.39	0.09	0.3	-7.5	0.03	300	900	0.48	0.7	1400000
Loam	28.2	0.43	0.03	0.3	-8	0	300	900	0.46	0.7	1400000

The dominant soil classes as provided by Hawkins (2012) are: Clay Loam, Unweathered Bedrock, and Clay for both the Wet and Dry Beaver Creek. Little calibration of soil classes that are not present in the Wet or Dry Beaver Creek was carried out due to the lack of streamflow data at the watershed outlet. After the changes to

bedrock depth were implemented, extremely high rates of soil evaporation were occurring in all soil classes due to the presence of more water near the soil surface. Using parameter sensitivity tests, air entry bubbling pressure was found to be a factor in controlling the high rates of soil evaporation. Thus, air entry bubbling pressure was reduced proportionally from Hawkins (2012) values based on how much the depth to bedrock changed in each soil class. The low values for decay of hydraulic conductivity parameters used in Hawkins (2012) led to little or no decay of hydraulic conductivity over the shallower depth to bedrock. Thus, the decay parameter was decreased across all soil classes and was also a main calibration parameter for the dominant soil classes. Saturated hydraulic conductivity is the second main calibration parameter. The largest changes in saturated hydraulic conductivity from Hawkins (2012) were in the unweathered bedrock soil classes. The bedrock lined channels of the Beaver Creek contain sinks and areas for water to accumulate during a precipitation event which are not represented with a uniform conductivity. Increasing saturated hydraulic conductivity served to represent these natural features and improved model performance.

After achieving adequate snowpack model performance and extensive testing of the soil parameter space in attempt to find a set of physically realistic parameters that represent both warm and cold season streamflow, we found that calibration for one season negatively impacted the other. The large amounts of cold season runoff from either rain or snowmelt events in the observed streamflow data led us to believe that soil properties are not time invariant in northern Arizona. Indeed, the efforts of the National Resource Conservation Service indicate that high elevation portions of the Beaver Creek can experience frost depths ranging from 18-30 inches (NRCS, 2010).

Changes in soil properties due to cold season processes in hydrological models is not a new concept. A technical report from the National Weather Service provides a literature review of how frozen soil effects can be incorporated into hydrological models using physically based or empirical methods (Koren et al., 2014). Additionally, Koren et al. (2006) found that soils with high clay fractions are the most sensitive to the impacts of frozen soil which coincides with four of the dominant soil classes in the Beaver Creek Watershed. The methods outlined in the technical report rely on the simulation of soil temperature. Lack of observed soil temperature (only one station in the watershed) and the current model version not accounting for exchange of ground heat flux between the soil surface and snowpack lead us to take a simpler approach to account for frozen soil effects. Specifically, linear relationship between air temperature and saturated hydraulic conductivity was implemented into the model as:

$$K_{sa} = \begin{Bmatrix} K_s, & if\ T_a > T_{max} \\ \alpha K_s, & if\ T_a < T_{min} \\ \dfrac{T_a - T_{min}}{T_{max} - T_{min}}(K_s - \alpha K_s) + \alpha K_s, & otherwise \end{Bmatrix}. \quad (41)$$

where K_{sa} is the adjust saturated hydraulic conductivity for cold season processes, T_{max} is the maximum air temperature at which frozen soil effects occur, T_{min} is the air temperature at which the soil is frozen, and α controls the minimum saturated hydraulic conductivity of frozen soil. The implementation of the equation above provides three calibration parameters for controlling runoff. Through sensitivity testing, we found that model is not overly sensitive to the parameter α with the value set 0.004. The model was

Table 9. tRIBS land cover parameter descriptions.

Parameter	Description	Units
P	Free Throughfall Coefficient - Rutter	[ ]
S	Canopy Field Capacity - Rutter	[mm]
K	Drainage Coefficient - Rutter	[mm/hr]
g	Drainage Exponential Parameter - Rutter	[mm^{-1}]
Al	Albedo	[ ]
h	Vegetation height	[m]
K_t	Optical Transmission Coefficient	[ ]
R_s	Canopy-average Stomatal Resistance	[s/m]
V	Vegetation Fraction	[ ]
LAI	Canopy Leaf Area Index	[ ]
Θ_s^*	Stress threshold for Soil Evaporation	[ ]
Θ_t^*	Stress threshold for Plant Transpiration	[ ]

found to be more sensitive to the two temperature thresholds which were calibrated to be (4°C, 7.5°C) for T_{min} and T_{max}, respectively. The reduction of cold season saturated hydraulic conductivity allowed us to adjust K_s to reduce runoff during the warm season from monsoon storm events while preserving runoff amounts during the cold season.

4.1.2 Land Cover Parameters

Land cover parameters control the amount of evapotranspiration and canopy intercepting that occur. tRIBS allows the user to choose between different methods for the simulations of evapotranspiration and canopy interception. The methods used in the study are Penman-Monteith and canopy water balance for evapotranspiration and

Table 10. Land cover parameter values for Beaver Creek watershed.

	Land Cover Parameters									
	P	***S***	***K***	***g***	***Al***	K_t	R_s	***LAI***	Θ_s^*	Θ_t^*
Desert Shrub	0.75	1.7	0.1	4	0.19	0.55	18.8	1.9	0.32	0.32
Desert Riparian	0.5	1.2	0.12	3.5	0.15	0.5	52.5	3.31	0.29	0.29
Grassland	0.9	1	0.12	4.7	0.14	0.8	30	1.65	0.30	0.30
Pinyon-Juniper	0.55	2	0.1	4	0.18	0.3	18.8	1.8	0.31	0.31
Developed	0.9	0.5	0.05	3.9	0.23	0.8	15	2	0.30	0.30
Ponderosa Pine	0.3	2.5	0.12	3	0.3	0.4	25	2	0.38	0.38
Water	1	1	0.01	3.7	0.07	1	0	0.1	0.31	0.31
Desert	0.9	0.2	0.05	3.7	0.25	0.9	22.5	0.4	0.32	0.32

interception, respectively. In total, these methods require the input of 11 parameters, the names of these are shown in Table 9.

Similar to the soil parameters, values from calibration preformed in Hawkins (2012) were used to parameterize the model application initially. As outlined in section 2.2.4, spatially distributed values of vegetation fraction and height were used in place of discrete values for each land cover class as performed with the other parameters. The parameter values for the eight land cover classes in the Beaver Creek model are shown in Table 10.

Three land cover classes cover approximately 93% of the entire Beaver Creek watershed: desert shrub, pinyon-juniper, and ponderosa pine. Parameter calibration focused on these three classes. Parameters that are important to the calibration process in the study are stomatal resistance, stress thresholds for plant transpiration/soil evaporation, leaf area index, and optical transmission coefficient. Stomatal resistance and the two stress thresholds are key parameters in controlling the evapotranspiration and turbulent fluxes from land cover. Lower stomatal resistance for vegetation reduces the amount of

transpiration that will occur. The two stress thresholds are used in determining the soil moisture stress, where higher values mean that the soil column is more easily stressed, which limits the water available for evapotranspiration. These three parameters were calibrated to reduce total evapotranspiration such that the average annual ratio of ET/P was not greater than 1 over the 16 year simulation period, a summary of the annual ET/P ratios is shown in Table 15.

LAI and optical transmission coefficients are important parameters in calibrating the snowpack simulations. LAI is a physical characteristic of vegetation that represent that canopy leaf area that is projected over the ground surface. In the snow model, LAI controls the snow holding capacity of the canopy. The optical transmission coefficient limits how much incoming solar radiation can penetrate the forest canopy and reach the snowpack. Decreasing the optical transmission coefficient results in the snowpack persisting longer into the spring when solar radiation is increasing after the low winter rates.

4.1.3 Model Initialization

In physically based models, the groundwater depth is critical in the proper simulation of soil dynamics at the start of the simulation period. Past studies using tRIBS (Vivoni et al., 2005; Hawkins, 2012) with deeper depths to bedrock than used here were based on drainage experiments to create the initial groundwater depth. These experiments consist of setting the water table level at the ground surface across the entire watershed and running the model with all meteorological and land surface fluxes turned off. The model is run until simulated streamflow matches that of the observed at the start of the

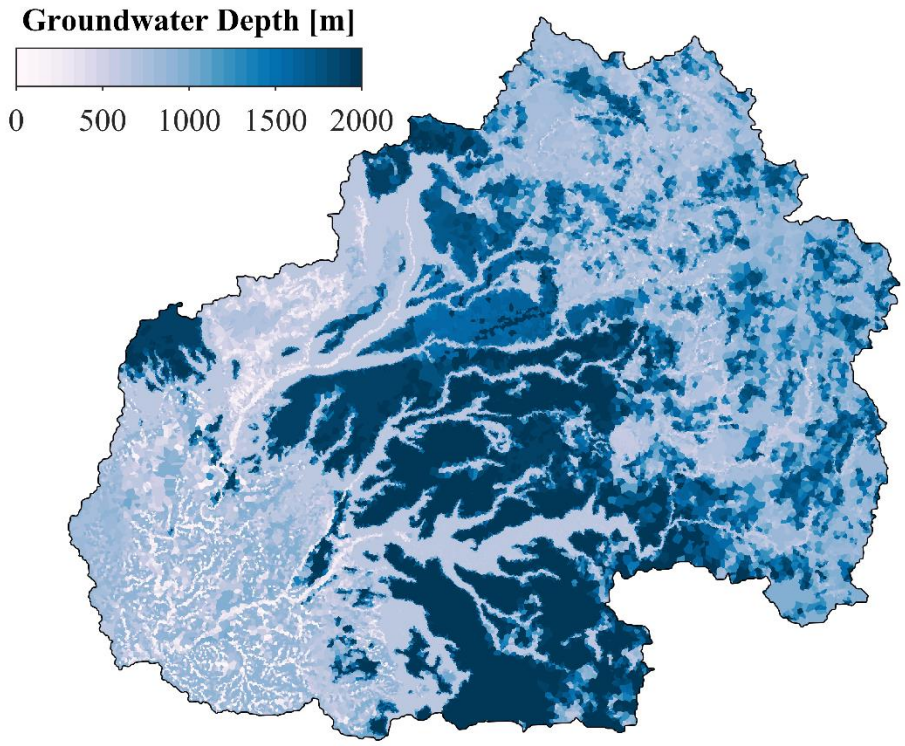

Figure 13. Map of initial groundwater depth at the start of the calibration period (October 1st, 2002) after 4 years of model spin-up using raw 12 km resolution forcing from the NLDAS-2 dataset.

simulation period of interest. Another common method is to run the model for a certain number of years before the simulation period of interest so that the soil moisture and groundwater depth reach a quasi-equilibrium at the start of the simulation period.

In the Beaver Creek model, a spin up period of 4 years, from October 1st, 1997 to September 30th, 2002 was used. An eight year spin up period was tested initially but due to the shallow bedrock depths in the watershed longer spin up periods had little to no impact on the soil water state at the start of the calibration period. Figure 13 shows a map of the initial groundwater depths at the start of the calibration period. tRIBS possesses the functionality to write restart files that contain values for all model state variables. From these restart files, the model can continue on exactly from where the model last ended.

These restart files were used separate the spin up and calibration period in order to start to start the model on October 1st, 2002.

4.1.4 Performance Metrics

Simulated streamflow and snow water equivalent (SWE) are compared to independent datasets using both qualitative (visual) and quantitative (metrics) methods. Streamflow is compared against observations from the USGS at two internal stream gauges in the watershed. Simulated SWE is compared against estimated SWE from the Snow Water Artificial Neural Network Modeling System (SWANN). Three performance metrics were selected that give a comprehensive overview of model performance. The metrics are root mean squared error (RMSE), bias, and correlation coefficient (CC). The mathematical definitions of these metrics are shown in the following equations:

$$RMSE = \sqrt{\frac{1}{N}\sum_{t=1}^{N}\left(Q_{o,t} - Q_{s,t}\right)^2}, \tag{42}$$

$$bias = \frac{\overline{Q_s}}{\overline{Q_o}}, \tag{43}$$

$$CC = \frac{\frac{1}{N-1}\sum_{t=1}^{N}\left((Q_{s,t} - \overline{Q_s}) * (Q_{o,t} - \overline{Q_o})\right)}{\sqrt{\frac{1}{N-1}\sum_{t=1}^{N}\left((Q_{s,t} - \overline{Q_s})^2\right)} * \sqrt{\frac{1}{N-1}\sum_{t=1}^{N}\left((Q_{o,t} - \overline{Q_o})^2\right)}}. \tag{44}$$

4.1.5 Point Scale Modelling

tRIBS can simulate scales ranging from regional watersheds (Ko et al., 2019) to single weather stations (Rinehart et al., 2008). When located within the watershed of interest, single point models are useful for some initial testing of model parameters and

Table 11. Distributed snow model parameters adjusted during the calibration process. Note that initial parameters are those derived from Rinehart et al., (2008).

Parameter	Units	Symbol	Initial Values	Calibrated Values
Minimum Liquid Prec. Temperature	[°C]	T_s	-1.1	0
Maximum Solid Prec. Temperature	[°C]	T_r	3.3	4.4
Liquid Water Holding Capacity	[ ]	φ_{liq}	0.06	0.08
Accumulating Snow Albedo	[ ]	α_a	0.85	0.88
Melting Snow Albedo	[ ]	α_m	0.85	0.82
Accumulating Albedo Decay Coefficient	[ ]	λ_a	0.94	0.94
Melting Snow Albedo Decay Coefficient	[ ]	λ_m	0.82	0.84

develop confidence in the model to expand simulations to the watershed scale. As outlined in section 2.1, there are two SNOTEL stations within the Beaver Creek. Hawkins (2012) developed a point scale model for Happy Jack SNOTEL and used it to compare simulated soil moisture and temperature to observations for one summer. Using the same model, I expanded the simulation period to 16 full years including snowpack dynamics.

Due to missing data on soil moisture and temperature at Happy Jack, the purpose of the point scale simulation was to the isolate key parameters that control snowpack accumulation, ablation, and canopy interception. An overview of the soil and land cover parameters for Happy Jack is shown in Table 11. The snow model parameter set

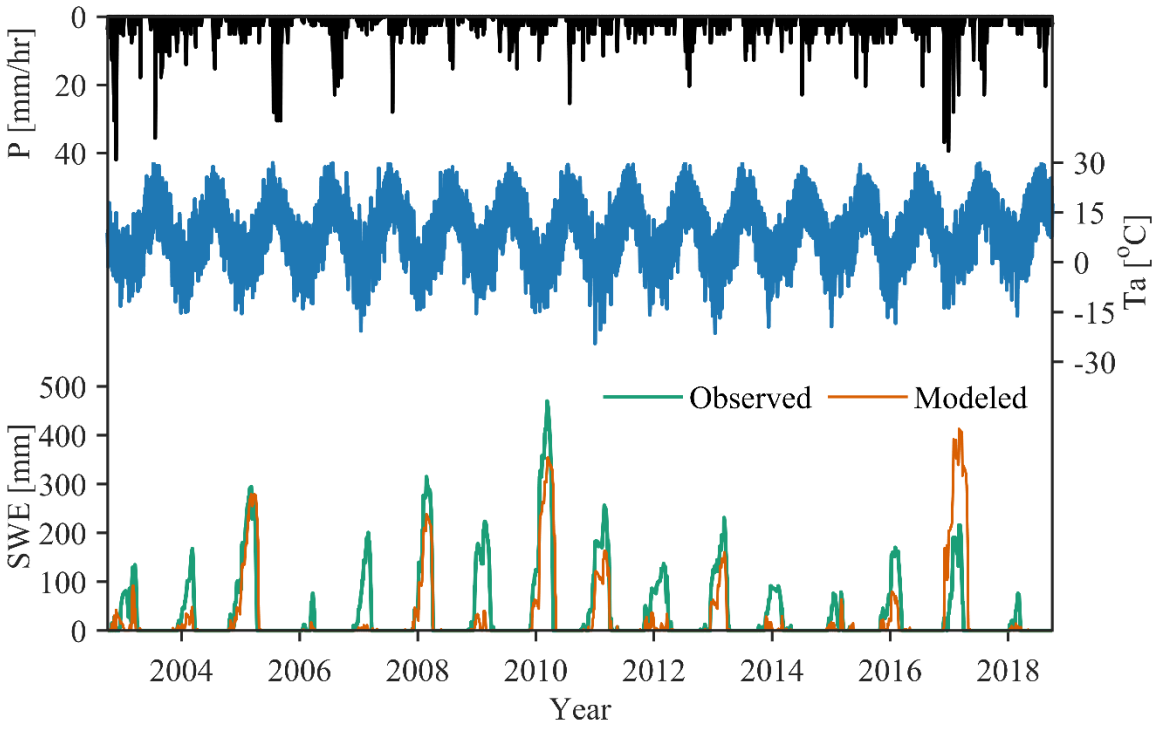

Figure 14. Hourly time series of precipitation, air temperature, and modeled versus observed snow water equivalent at Happy Jack SNOTEL.

developed at Happy Jack were then incorporated into the single point model for Bar-M SNOTEL for an independent validation of the model. These parameter values along with the initial values are shown in Table 11. These parameters are the final values from the model calibration and validation that were re-incorporated into the SNOTEL models to prepare the simulation results for the point scale models.

Sensitivity testing at Happy Jack yielded a set of parameters that snowpack simulations are the most sensitive to: liquid water holding capacity, temperature thresholds for precipitation partitioning, and coefficients for snowpack albedo decay. Increasing liquid water holding capacity of the snowpack aids in retaining the snowpack longer into the spring when increased temperatures result in phase transition from ice to liquid during the day. At night, if the temperature drops back below zero, the liquid water

can transition back into the ice phase. Similarly, high liquid water holding capacity can aid in snowpack retention during mixed phase precipitation events. Liquid water holding capacity values that are too large will result in unnaturally high retention of the snowpack into the early summer. The temperature thresholds are critical for simulating the amount snowfall that reaches the canopy or land surface. I found that the model is more sensitive to the maximum temperature at which snow can fall which is in agreement with other applications (Sun et al., 2019). The coefficients for decay of snow albedo with time are important for controlling how long the snowpack persists into the late spring when solar radiation is rapidly increasing. Sun et al. (2019) calibrated albedo coefficients at SNOTEL stations across the western United States and aggregated the results into the eight ecoregions. The calibrated values for AZ-NM ecoregion provided improved results over the default values and were incorporated into the model. Figure 14 displays the time series of observed and modeled SWE, along with air temperature and precipitation.

Happy Jack SNOTEL is located in a forest clearing surrounded by ~16 m tall ponderosa pine trees. Canopy interception of snowfall before reaching the snow pillow measurement station is predicted to be close to zero. Modelling Happy Jack as an open

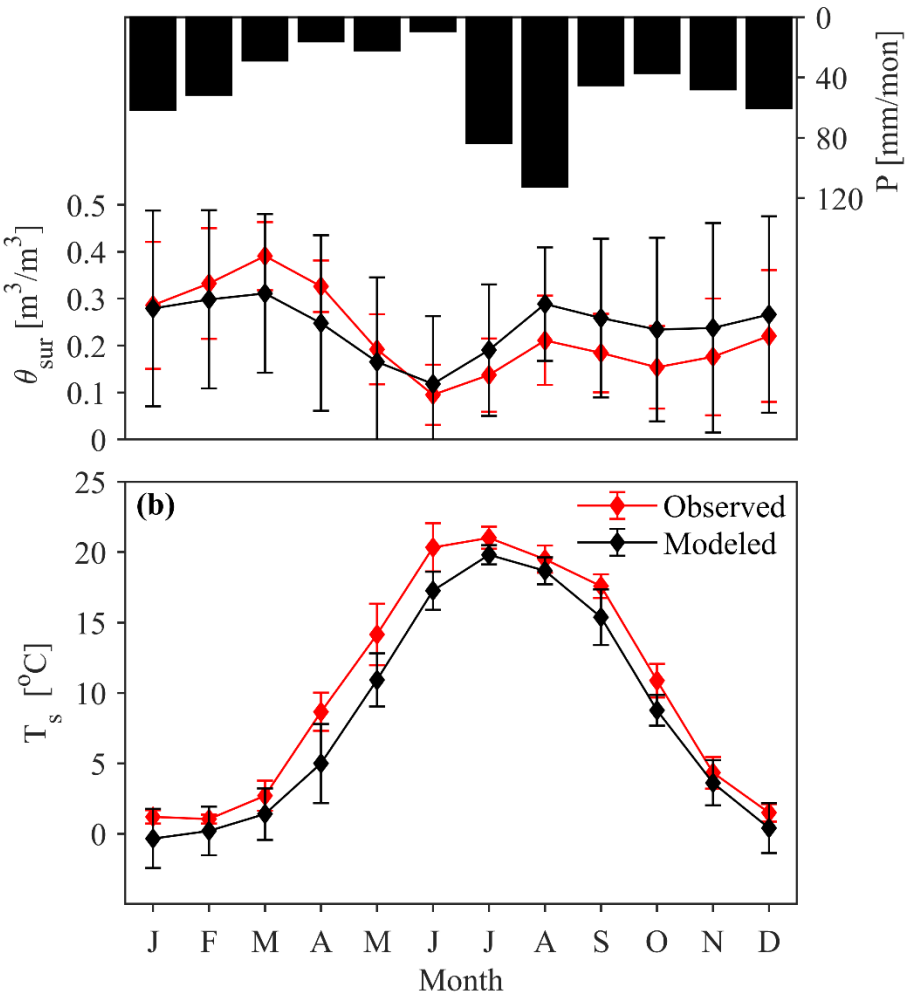

Figure 15. (a) Monthly mean time series of precipitation, modeled versus observed volumetric soil moisture, $\theta_{sur.}$ (b) Monthly mean modeled versus observed soil temperature, T_s. Monthly standard deviations are shown as error bars.

clearing (changing land cover type to grassland), however, would result in no shading from solar radiation by the canopy or reduction in sub-canopy windspeed. The latter two factors were found to be more important in the simulation of SWE as compared to canopy interception of snowfall. Thus, the model treated the station as ponderosa pine forest. Overall, the model captures well the timing of snow accumulation and melt when compared to the observations. Water years with observed snowpacks below 150 mm of

maximum SWE proved difficult for the model to simulate due to the sensitivity of the energy balance of small snowpacks to small changes in meteorological conditions like air temperature. Adjusting key parameters that affect the snow model to better simulate underperforming years would disrupt performance in other years. Thus, a balance was struck to not over-simulate years with large snowpacks, but still simulate less active snow years reasonably well.

Figure 15 shows the point scale simulation results of surface soil moisture (θ_{sur}) and temperature (T_s) versus observations at 50 mm sensor depth. Observations were aggregated to monthly mean values due to missing data and erroneous values. Modeled surface soil moisture are average values over the top 100 mm of the soil column. The model is able to capture the annual trends in soil moisture and temperature. Soil moisture conditions reaching values close to saturation during the late winter/early spring were not achievable in the model. In addition, model results showed increased deviation from the mean values compared to the observed soil moisture. The snowpack soil moisture simulations shown above provided confidence in the model and led to the development of a second point scale model for the Bar-M SNOTEL.

As highlighted in section 2.1, Bar-M SNOTEL data collection began in the fall of 2012. Soil and land cover parameters required for simulations were acquired from the watershed scale model, displayed in Table 11. Bar-M is situated ~400 m below Happy Jack in elevation and experiences smaller snowpacks compared to corresponding years at Happy Jack. Figure 16 shows that the model setup at Bar-M is able to better simulate the smaller snowpacks. Like at Happy Jack, the model is able replicate well the timing of snow accumulation and melt, as shown with the 0.88 correlation coefficient. In addition,

Table 12. Model land cover and soil parameters from calibration at Happy Jack and validation at Bar-M SNOTEL stations. Parameter values for Bar-M were retrieved from the watershed scale model.

Station	Land Cover Parameters											
	P	***S***	***K***	***b***	***Al***	***h***	***Kt***	***Rs***	***VF***	***LAI***	θ_s^*	θ_t^*
Happy Jack	0.3	2.5	0.12	3.5	0.3	16	0.4	25	0.43	2.2	0.38	0.38
Bar-M	0.3	2.5	0.12	3	0.3	11	0.4	25	0.5	2.2	0.38	0.38

	Soil Parameters										
	K_s	θ_s	θ_r	λ	ψ	f	a_s	a_u	N	k_s	C_s
Happy Jack	29.3	0.48	0.02	0.44	-15.3	0.126	200	300	0.44	0.7	1400000
Bar-M	25.3	0.39	0.08	0.35	-3.4	0.008	300	300	0.47	0.7	1400000

Table 13. Performance metrics for Happy Jack and Bar-M snowpack simulations. Metrics were calculated using daily average SWE for the cold season (NOV. to APR.).

	Metrics		
	RMSE [mm]	**Bias [ ]**	**CC [ ]**
	Calibration		
Happy Jack	76.9	0.71	0.69
	Validation		
Bar-M	15.8	0.72	0.88

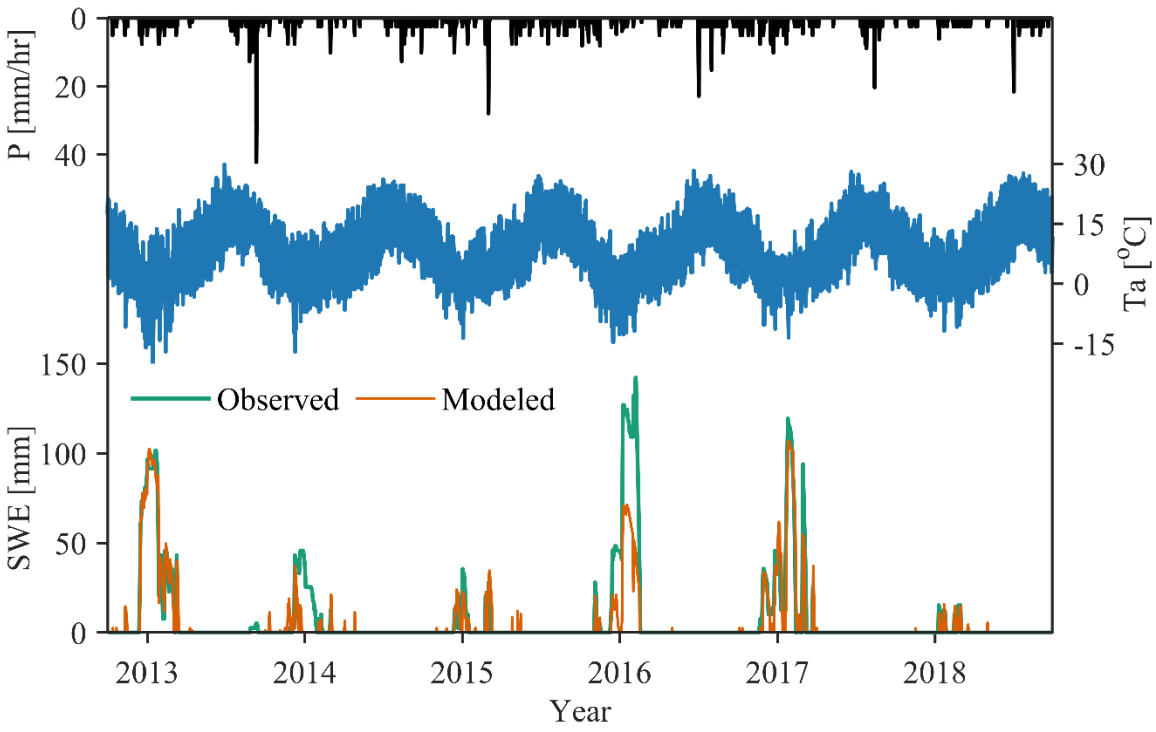

Figure 16. Hourly time series of precipitation, air temperature, and modeled versus observed snow water equivalent at Bar-M SNOTEL.

Bar-M is able to better represent the maximum SWE, even in years with smaller snowpacks. The bias, shown in Table 12 for both stations are similar and indicate ~30% under simulation of SWE. Simulating the same maximum SWE at SNOTEL sites proved difficult without degrading performance in drier years. This is not surprising because SNOTEL sites are known to be in location that accumulate large amounts of snow compared to their surrounding areas (Bales et al., 2006).

4.1.6 Basin Scale Modelling

Data available from NEXRAD ST4 began in 2002 which corresponds with the time at which most of the weather stations used to prepare model forcings were

established. The complete simulation period for the study was chosen to be water years (WY) 2003 to 2018, 16 years of simulations in total. This was separated into two halves, WY2003-2010 and WY2011-2018 for the calibration and validation period, respectively. Calibration of the snow model parameters took place before streamflow due to the nature of needing snowmelt to be correct before streamflow.

Multiple iterations of precipitation and meteorological forcing were tested during the model calibration process. Initial bias correction of NEXRAD followed Robles-Morua et al. (2012) using annual mean areal precipitation (MAP) across the watershed, but this led to a miss characterization of the elevation-precipitation relationship in the watershed. Meteorological forcings were originally developed by downscaling raster cell values from the NLDAS-2 that fall within the watershed, but this method poorly represented air temperature within the watershed which is a key component for snowpack simulations. The inclusion of localized air temperature lapse rates, outlined in section 3.2.1, led to advantageous improvements in the model forcing.

Figure 17 shows the visual performance of snowpack simulations in the Beaver Creek using daily basin average SWE and scatter plots of cold season average SWE versus elevation for the calibration and validation periods. Peak SWE magnitude is generally lower in the modeled case compared to SWANN (estimated). Nonetheless, the model still captures the overall trends in timing of snow accumulation and melt. Water years with large, modeled winter snowpacks (WY2005 and 2010) yielded calibration difficulties as SWE at high elevation would persist into the late spring and early summer, which has cascading effects on streamflow generated from snowmelt. A balance was struck that improved melt timing for wet winter years, but did not negatively impact drier

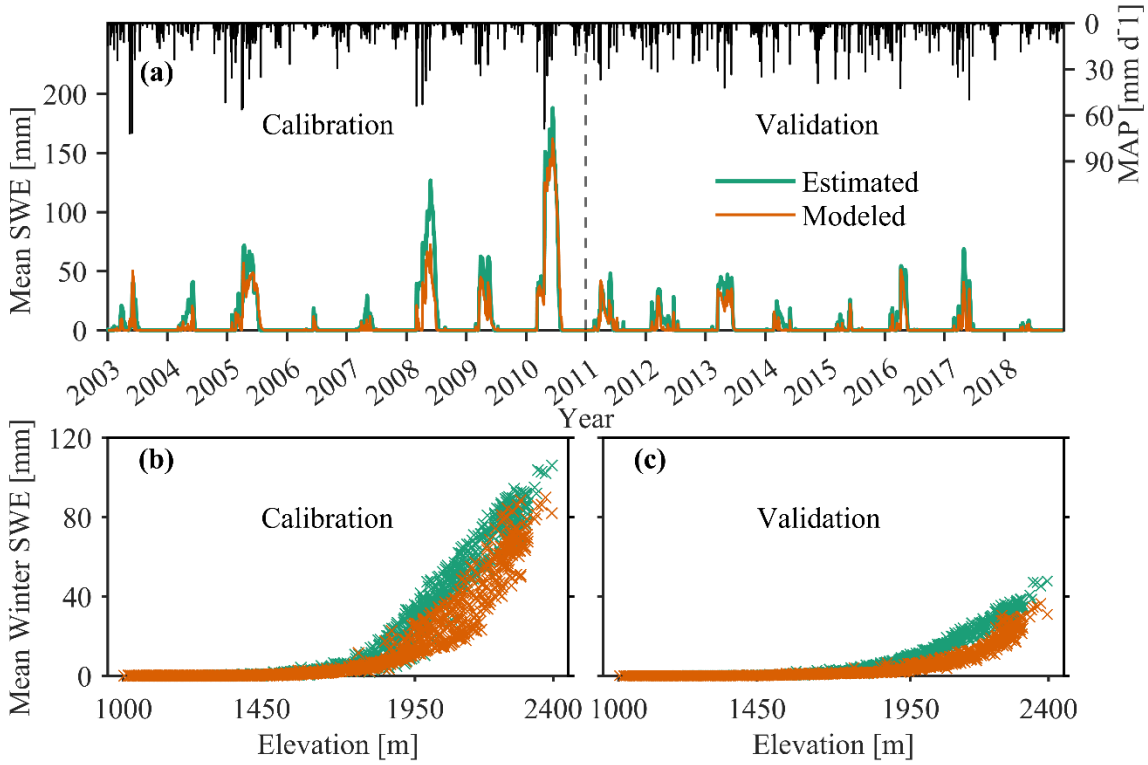

Figure 17. (a) Modeled and estimated mean snow water equivalent timeseries from calibration (WY2003-2010) and validation (WY2011-2018). Mean winter (NOV.-APR.) snow water equivalent from 1km raster cells for (b) calibration and (c) validation.

years in the calibration period. Less than ideal performance in certain years can be due to a number of factors, but the main contributors are the air temperature and precipitation forcings and their interaction with the phase partitioning method in the model. In order to simulate snowfall to the land surface, both hourly forcings have to be in agreement. If the timing between P and T_a is out of phase, then no snowfall or mix phased precipitation will occur, either of which can result in liquid water passing through the snowpack to the soil surface. An example of this is January of WY2008, where several large snow accumulation events in the SWANN estimates are missed in the simulations. This results in under simulation of SWE for the entire winter, even though events later in the season are better modeled. For these accumulation events, the precipitation forcing was checked

Table 14. Performance metrics between estimated and modeled basin average SWE for the calibration and validation periods. Metrics computed at a daily resolution during only months within the cold season.

RMSE [mm]	Bias [ ]	CC [ ]
Calibration		
14.8	0.7	0.95
Validation		
7.2	0.58	0.92

and there are indeed large events, but the air temperature is not cold enough for snow to fall in the model.

Table 13 contains the performance metrics outlined in section 4.1.4 between the estimated and modeled basin average SWE time series (Figure 17a) for the calibration and validations periods during cold seasons months. Values for the metrics are similar to other applications of the same model (Mahmood et al., 2014; Moreno et al., 2016). While the metrics show good agreement with the SWANN dataset, note that the comparison is not to observational data. SWANN itself is a model output and subsequently was not taken as the ground truth throughout the calibration process. The larger under simulation of SWE in the validation period indicated by the bias is not immediately visually present in the time series. Figure 17c indicates that largest under simulation of SWE occurring in the 1950 to 2200 m elevation band in the watershed. Under simulation at these mid elevations in the model are attributed to the quality of the air temperature forcing to the model. The stations used to derive the air temperature forcing (Figure 1) are not located near or at the same elevations where the poor performance occurs. Therefore, air temperature forcing for these areas are populated using interpolation of the closest

stations. If more stations were available in these areas, model metrics such as bias are expected to improve for both calibration and validation periods. Figure 17b,c highlight the model ability to match average SWE estimations at low to mid elevations. The formation of small, shallow snowpacks at low elevations is common in any given year but they will quickly melt due to low vegetation fraction and warmer air temperature. For the calibration period, the modeled average SWE generally has the same pattern of SWE versus elevation but the elevation at which average SWE begins to rapidly increase is at a higher elevation in the modeled case. The general pattern of the estimated SWE versus elevation for calibration and validation period are considerably different. The reason behind the difference is attributed to the three years with larger than average snowpack from WY2003 to 2010. Although the model was not able to reproduce the same pattern as SWANN for the validation period, the timeseries of mean SWE shows good performance.

Figure 18 displays the mean difference across water years for maximum SWE for both the calibration and validation periods. Both calibration and validation show the largest difference in maximum SWE occurring at the upper elevations, where most snowfall occurs. In addition, the larger difference in maximum SWE for calibration period is expected because larger snowpacks during those years. Lower elevations show maximum SWE near or slightly above zero. Over simulation of average maximum SWE difference during the calibration at low elevations is attributed to a large snow accumulation event during WY2002 which rapidly melted.

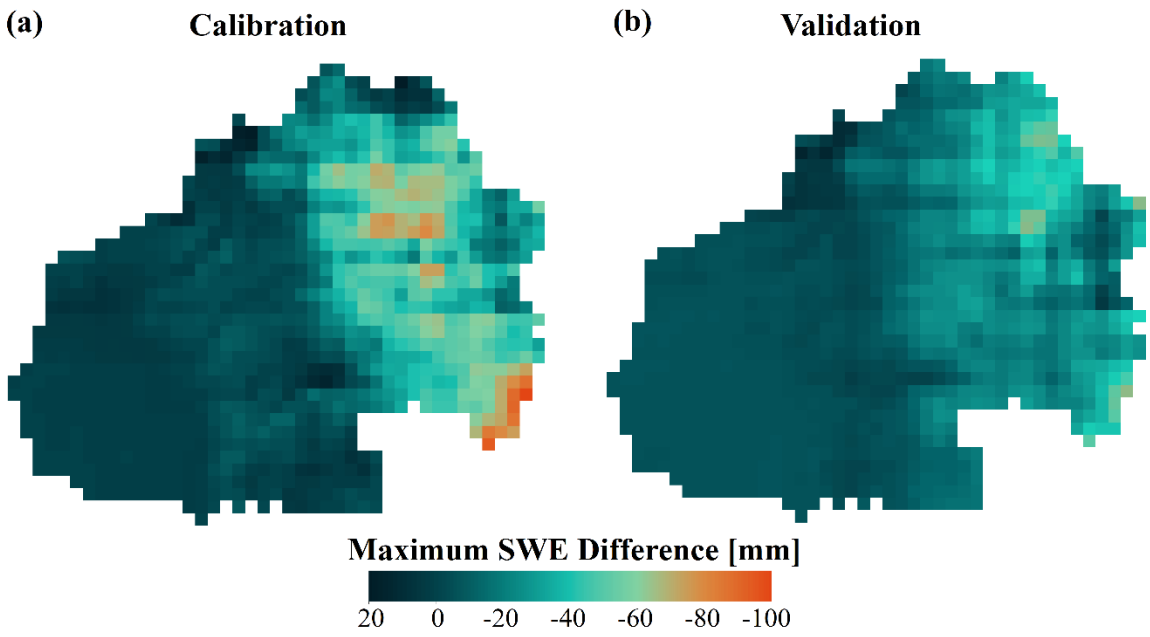

Figure 18. Maps of average difference in SWE between modeled and estimated (modeled minus estimated) across water years for (a) calibration and (b) validation periods.

Following the snowpack model calibration in the Beaver Creek, efforts shifted towards the calibration of streamflow. As highlighted in section 2.2.6, the streamflow gauge at the model outlet has large swaths of missing data along with an improper rating curve in recent years. Thus, calibration focused on simulating the two nested streamflow gauges in the watershed. Observations from the Wet and Dry Beaver Creek streamflow gauges were aggregated from 15 minute to hourly averages using Matlab timetables.

Figure 19 shows the visual performance of modeled hourly streamflow compared to observations for the two streamflow gauges. The largest magnitude stream flow events in both the Wet and Dry Beaver Creek occur during the cold season. Peak discharges from snowmelt and rainfall events are generally much larger in the Dry Beaver Creek. Wet Beaver Creek sees a small but sustained baseflow throughout the year due to the

Table 15. Model performance metrics for quantifying modeled hourly streamflow performance for Wet and Dry Beaver Creek broken down by season of the year. Cold season corresponds to November to April while warm season is May to October.

Season	Stream Gauge	Metric		
		RMSE [m^3/s]	**Bias [ ]**	**CC [ ]**
	Calibration			
Cold Season	Wet Beaver Creek	3.91	0.84	0.52
	Dry Beaver Creek	5.47	0.73	0.50
Warm Season	Wet Beaver Creek	2.82	0.87	0.53
	Dry Beaver Creek	3.90	0.81	0.51
All	Wet Beaver Creek	3.36	0.86	0.52
	Dry Beaver Creek	4.68	0.77	0.51
	Validation			
Cold Season	Wet Beaver Creek	1.96	1.19	0.54
	Dry Beaver Creek	3.60	0.94	0.60
Warm Season	Wet Beaver Creek	1.54	1.25	0.52
	Dry Beaver Creek	2.61	1.16	0.60
All	Wet Beaver Creek	1.75	1.22	0.53
	Dry Beaver Creek	3.10	1.05	0.60

presence of springs. In its current formulation, this spring-based baseflow is not represented in the tRIBS model. Figure 19 highlights that the model is able to simulate the large cold season streamflow events from the observations but is unable to match the magnitude of these events during specific water years such as 2005. The magnitude of simulated cold season streamflow events is close for both the Wet and Dry Beaver Creek, but Dry Beaver Creek is farther from the observations due to the larger events present in those observations. The timeseries of hourly streamflow were used to calculate the three model performance metrics, shown in Table 14. The metrics show that the model preforms marginally better during the warm season compared to the cold season but overall, there is good performance, with undersimulation and oversimulation of ~15% during the calibration and validation periods, respectively.

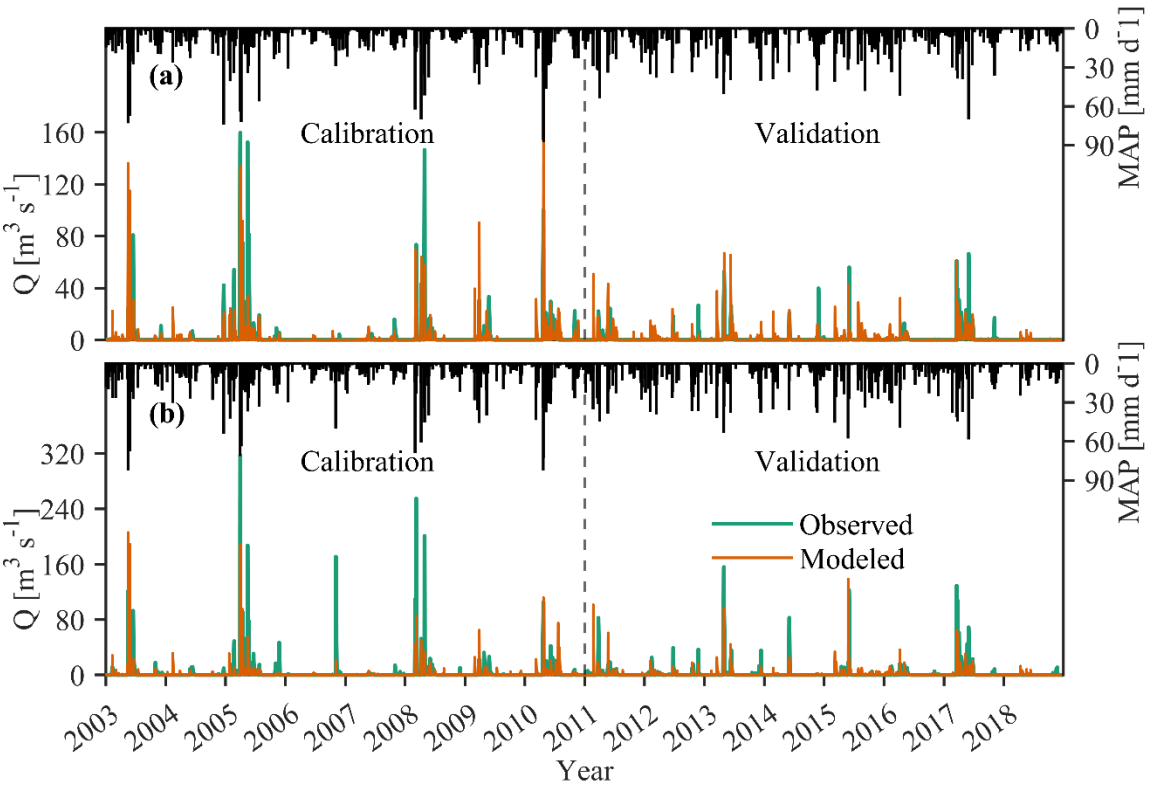

Figure 19. Hourly time series of mean areal precipitation and modeled versus observed streamflow for (a) Wet Beaver Creek and (b) Dry Beaver Creek.

In addition to the hourly streamflow, mean monthly streamflow was used for visual calibration of streamflow, as shown in Figure 20 with shaded curves representing ±1 standard deviations. The monthly mean streamflow highlights the variation in observed streamflow between the calibration and validation periods. The model is able to simulate well the unimodal pattern of streamflow, with peaks generally occurring earlier in the cold season for the calibration period. There is also a pattern of larger, early cold season streamflow for the simulations due to the simple method by which saturated hydraulic conductivity is adjusted based on air temperature. The latter also leads to the well simulated average streamflow during the warm season. The monthly averaged streamflow observations also highlight the large variation in magnitude and shape of the

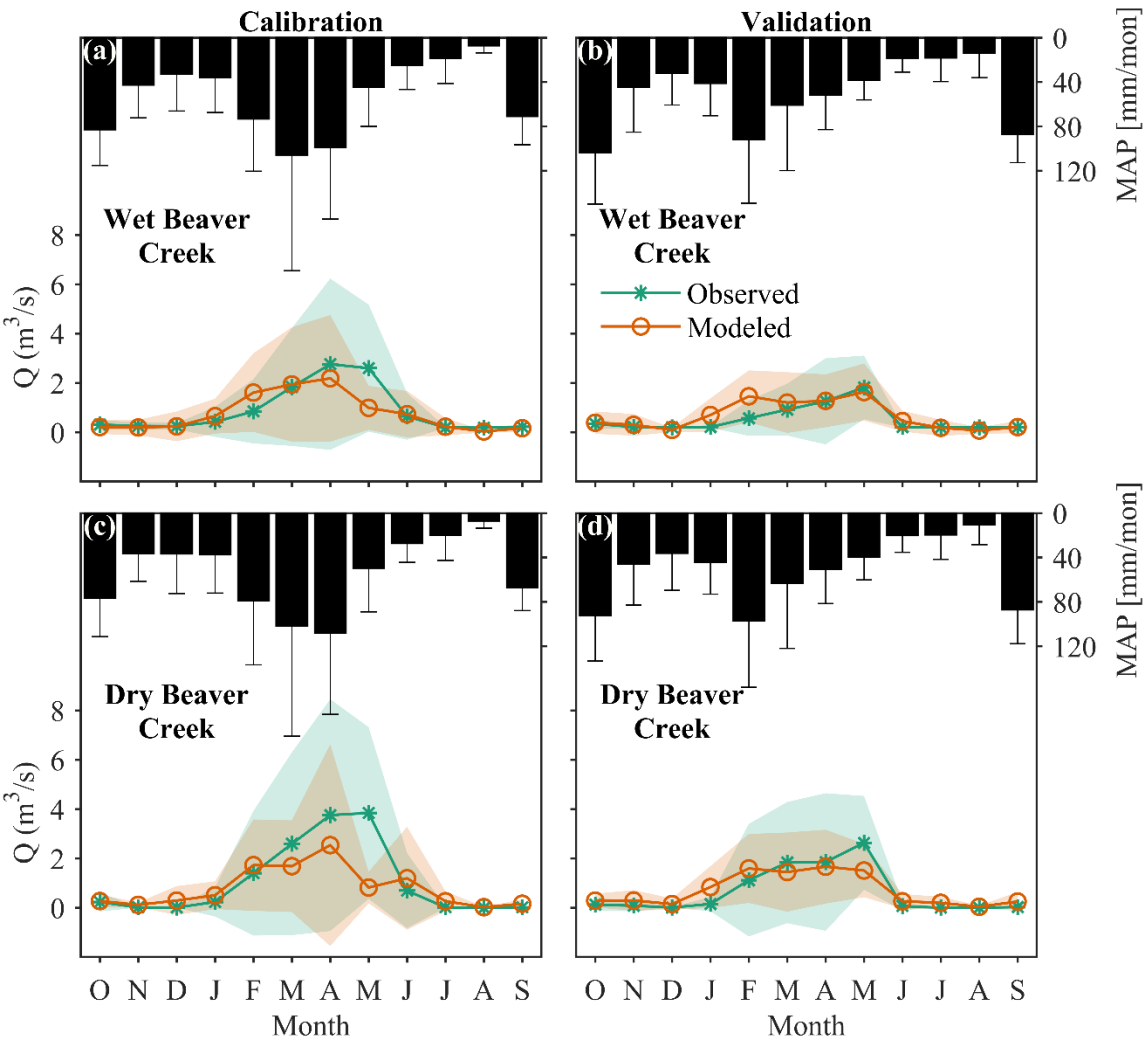

Figure 20. Modeled versus observed streamflow for calibration and validation periods in the (a, b) Wet Beaver Creek and (c, d) Dry Beaver Creek. Results are shown as monthly totals for precipitation and monthly means for streamflow with shaded curves and error bars showing ±1 standard deviations.

annual streamflow hydrograph between calibration and validation periods, both of which the model is able to simulate well.

Figure 21 shows the cumulative hourly streamflow for the simulations and observations along with precipitation model forcing in the Wet and Dry Beaver Creek. For both subwatersheds, the model is able to capture the rise in cumulative streamflow

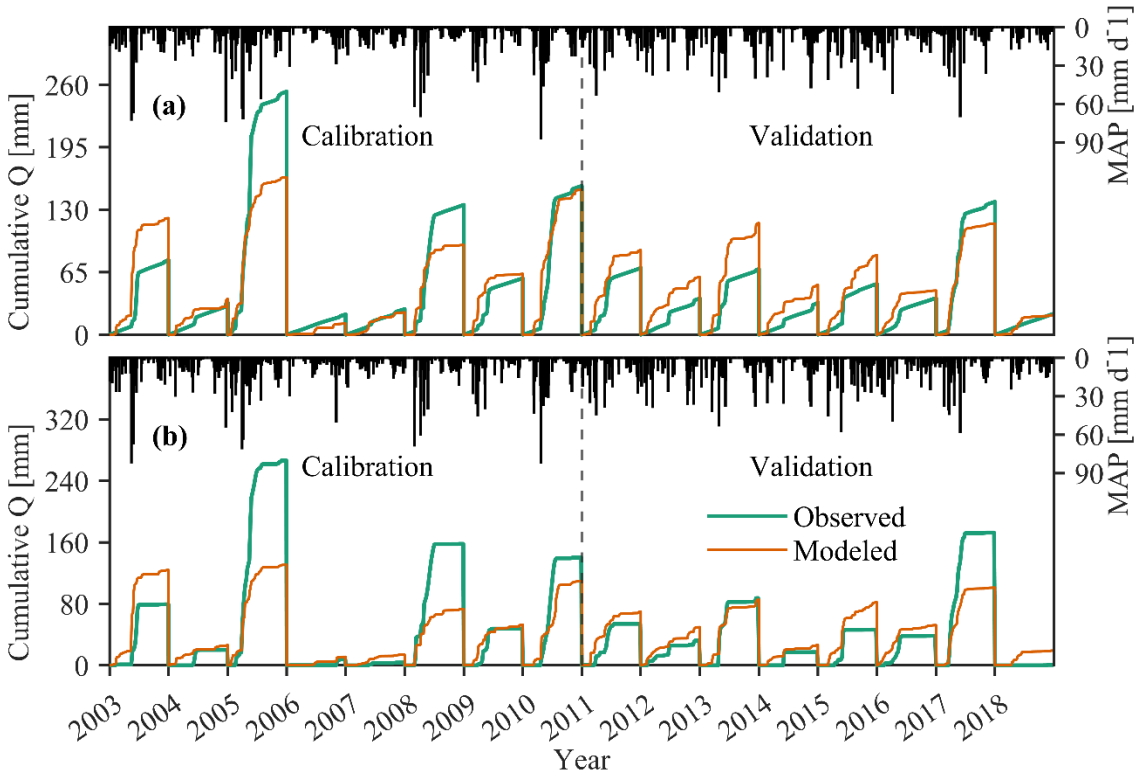

Figure 21. Hourly cumulative streamflow from observations and modeled for (a) Wet and (b) Dry Beaver Creek along with mean areal precipitation.

that occurs in the middle of the cold season, typically starting in January or February. During the calibration period, Wet Beaver Creek performs well compared to Dry Beaver Creek which under simulates four of the water years. Overall, model performance in terms of streamflow volume for both subwatersheds is good considering the drastic variance in precipitation regimes that occurs over a 16-year simulation period. Over or underestimation of streamflow in the Beaver Creek watershed is not unexpected, the area is known for complicated subsurface geology that contributes to the constant baseflow observed at Wet Beaver Creek. In addition, certain hydrologic processes such as channel losses were not accounted for in the version of tRIBS used in the study. Most of the Wet and Dry Beaver Creek has channels that are lined with bedrock, but at upper elevations

bedrock lined channels are not as prominent. Under simulation during extremely wet years like WY2005 is attributed to the unique precipitation regime that occurred that year. WY2005 is the wettest winter in the simulation period but had average snowfall. Due to this outlier, the majority of the precipitation that year was added to the subsurface which is visible with the change in subsurface storage for that year.

Table 15 shows the annual water balance for the Beaver Creek watershed model. Here, ET_{tot} includes both warm season ET from soil evaporation, dry canopy transpiration, and wet canopy evaporation along with canopy (Sub_C) and ground (Sub_G) sublimation when there is snow present. Due to the robust outputs from tRIBS, we are able to directly compute every component of the basin scale water balance. The change in subsurface storage, dS/dt, is the summation of the water stored in the saturated and unsaturated zones (below or above the groundwater table). Computing dS/dt is accomplished using the basin average hydrologic timeseries file (*.mrf) using the following equations:

$$\frac{ds}{dt} = \frac{dMu}{dt} + \frac{dMs}{dt}, \tag{45}$$

$$\frac{dMs}{dt} = (MGW_S - MGW_E)M\theta_s, \tag{46}$$

$$\frac{dMu}{dt} = (MSMU_E MGW_E - MSMU_S MGW_S)M\theta_s. \tag{47}$$

where Mu is the depth of water above the water table, Ms is the depth of water in the water table, MGW_S and MGW_E are the mean depth to the groundwater table at the start and end of the water year respectively, $M\eta$ is the spatially averaged porosity, $MSMU_S$ and $MSMU_E$ are the mean soil moisture above the groundwater table at the start and end of the water year respectively, and $M\theta_s$ is the spatially averaged soil moisture at

Table 16. Watershed scale water balance for the entire Beaver Creek. Note that Q_{sim} is the simulated streamflow at the model outlet.

Water Year	Q_{sim}	P	ET	S_G	S_C	ET_{tot}	dS/dt	Q_{sim}/P	ET_{tot}/P
				[mm/yr]					
2003	134	692	409	31	29	469	105	0.19	0.68
2004	26	406	344	27	26	396	-18	0.06	0.98
2005	125	888	419	29	29	476	295	0.14	0.54
2006	10	363	383	14	13	410	-64	0.03	1.13
2007	19	403	373	29	16	417	-63	0.05	1.03
2008	76	557	356	52	32	440	19	0.14	0.79
2009	54	438	341	34	23	397	-26	0.12	0.91
2010	119	627	321	59	24	403	80	0.19	0.64
2011	67	529	384	43	23	450	19	0.13	0.85
2012	49	543	391	36	27	454	50	0.09	0.84
2013	84	589	398	41	33	472	122	0.14	0.80
2014	32	433	351	14	9	374	55	0.07	0.86
2015	60	549	415	5	5	426	68	0.11	0.78
2016	39	490	444	38	22	504	-112	0.08	1.03
2017	80	593	451	25	24	500	0	0.14	0.84
2018	17	277	371	12	8	392	-165	0.06	1.41
Mean	62	524	385	31	21	436	23	0.11	0.88

saturation. The goal of looking at the basin scale water balance is to ensure closure of the water balance. Table 15 shows that indeed the model is closed or very close to with closure indicated by the mean values of the water balance ($dS/dt = P - ET_{tot} - Q_{sim}$). Due to code limitations, the precipitation shown in the table was calculated from the precipitation grids fed into the model rather than from the outputs.

The effect of using subsurface storage to meet evaporative demands in dry years is commonly referred to as the carryover effect. Wang and Alimohammadi (2012) found that specifically in arid regions of the United States that the carryover effect reduced the variability of *ET* due to variability of the climate. Table 15 highlights the model's ability to simulate the carryover effect through patterns of extremely wet years adding large

amounts of water to subsurface storage (WY 2005), while subsequent dry years with low precipitation withdraw subsurface storage (WY 2006). Furthermore, from Table 15 one can see the difference in variability between *P* and *ET* with *ET* having lower variability which is attributed to the subsurface storage added in wet years. While WY2005 shows a carryover effect lasting potentially two years up to WY2007, WY2010 is also a wet year that does not add as much to the subsurface and has a smaller carry over effect. This is attributed to difference in climate between the years, WY2005 was extremely wet and warm while WY2010 is wet and cold. Furthermore, WY2005 precipitation during the cold season was many smaller events over the cold season which allowed large amounts of infiltration to occur. WY2010 precipitation is largely attributed to one atmospheric river event that resulted in the formation of a large snowpack rather. Soils are saturated in the late cold season when snowmelt begins thus more runoff rather than infiltration occurs.

4.2 Simulation Experiments

The goal of the simulation experiments is to analyze the changes in the basin scale water balance due to climate change and forest thinning. To accomplish this, the modified model inputs and parameters, described in section 3.3, were used to run the Beaver Creek model over the entire 16-year simulation period. In total, the simulation experiments add an additional 306 years of simulations or approximately 16,000 hours of computational time. Table 6 in summarizes the nine additional simulations experiments and the acronyms that will be used to reference them. The forest thinning experiments are

Table 17. Summary of pre- and post-treatment differences in LAI, p, S, and k_t and change factors used derive post-treatment values.

	P [ ]	S [mm]	K_t [ ]	LAI [m^2/m^2]
Change Factor	1.54	0.77	1.13	0.77
Pre-treatment	0.3	2.5	0.4	2.2
Post-treatment	0.46	1.92	0.45	1.69

represented using a set of five vegetation parameters, four of which are shown in Table 16, the fifth parameter, vegetation fraction is provided to the model in raster format.

4.2.1 Water Balance Impacts

Following Vivoni et al. (2005), changes in the basin scale water balance were examined as percent changes from the Base Case and as annual totals. Figure 22 shows the relative change in components of the water balance using percent change from the Base Case. While Figure 23 shows annual totals for fluxes and average SWE. Looking only at the Base Case plus warming scenarios, we can see that streamflow increase by a small amount at +1°C of warming, approximately 1.5% or 1 mm annually over the base case. At +2°C and above of warming, the total *ET* starts to dominate, reducing annual average streamflow in the Base Case. Interestingly, the curve for percent change in streamflow is not linear, with little to no changes in *Q* up to +2°C of warming, but the rate of decrease in streamflow increases rapidly at +4°C of warming with a 10% reduction compared to the Base Case. The increase in *Q* at +1°C is attributed to reduction in total sublimation with warming which is discussed in a later section. The forest thinning experiments in Figures 22 and 23 show that the change in components of the water balance follow generally the same pattern but shifted upward or downward

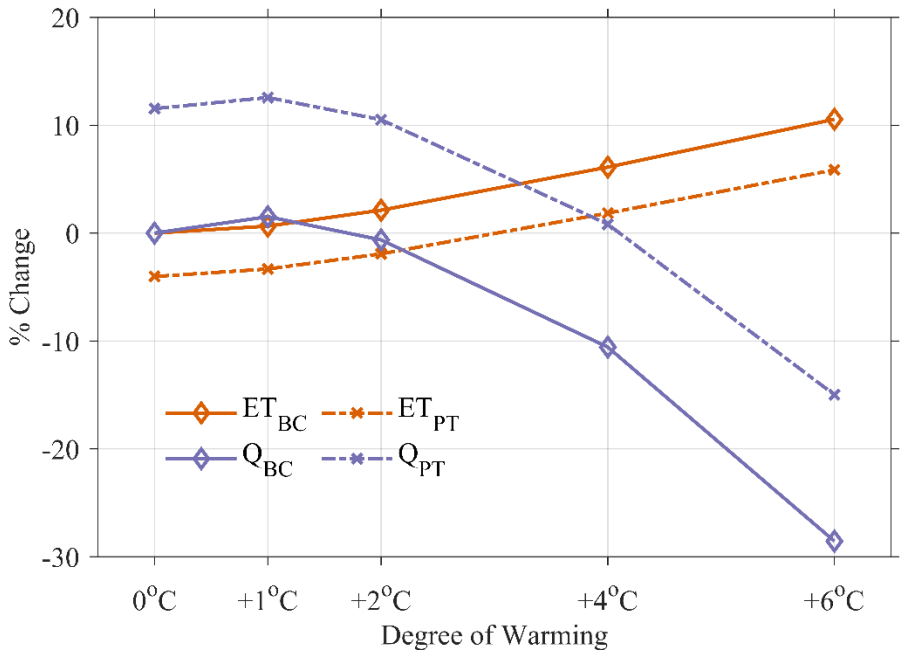

Figure 22. Percent change in components of the basin scale water balance for the climate change and forest thinning experiments.

depending on the variable. Across all post-treatment experiments, streamflow is approximately 12% higher than the Base Case counterpart. Difference between the Base Case and Post-treatment increases slightly as warming increases, making thinning more valuable at higher levels of warming. Thus, the threshold at which the increase in total *ET* takes over the increased *Q* occurs at around +4°C of warming. The increase in streamflow is largely attributed to the decrease in evapotranspiration after thinning. The thinning experiments also reinforce the importance of the ponderosa pine ecosystem on the hydrological fluxes in the watershed. Specifically, changes in only the vegetation properties of ponderosa pine leads to considerable change in the basin water balance. Annual water balance totals for the nine simulation scenarios are available in Tables F.1 through F.9 in Appendix F.

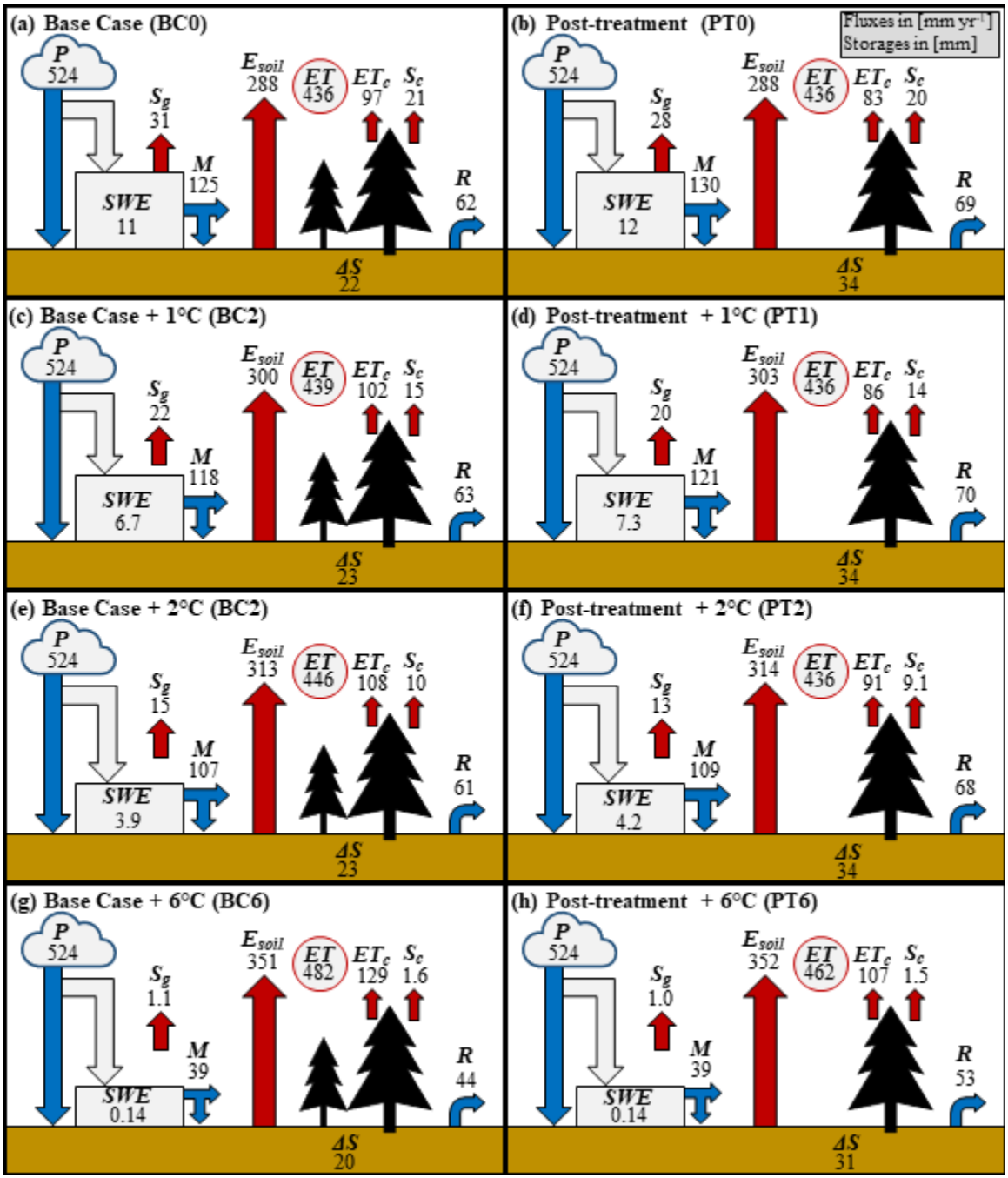

Figure 23. (a – h) Average annual components of the basin scale water balance for Base Case and Post-treatment simulation experiments at +0, +1 +2, and +6°C of warming. Where P is precipitation, SWE is snow water equivalent, M is snowmelt, S_g is ground sublimation, S_c is canopy sublimation, ET is total evapotranspiration, E_{soil} is bare soil evaporation, ET_c is canopy evapotranspiration, ΔS is change is subsurface storage, and R is runoff.

4.2.3 Changes in Snowpack

The changes in snow accumulation along with ablation due to climate change and forest thinning were examined in order to determine their impacts on other hydrologic processes. Critically important to the model simulations of snowpack is the partitioning of precipitation into ice or liquid. The climate change experiments have a direct effect on this partitioning because of the method implemented into the model. Figure 24 highlights these impacts of increasing temperatures on the average annual winter snowfall fraction using the model forcings and the precipitation phase model. The rapid progression of low snowfall fraction only at lower elevations without warming to covering most of the watershed at +2°C is interesting. From +0°C to +2°C of warming, the spatial average snowfall fraction decreases by 35%, while at +6°C this decrease is 80%. These changes in the amount of snowfall are most realized at higher elevations in the ponderosa pine forest where the majority of cold season precipitation falls. Ground snowpacks at lower elevations experience increased solar radiation due to lower vegetation coverage and air temperatures which results in negligible amounts of snow accumulation at these elevations even without warming. Snowpacks act as natural reservoirs of precipitation that delay the transformation of precipitation into runoff. Therefore, transitioning from snowfall to rain is expected to alter the timing and magnitude of streamflow. While Figure 24 is based on the model forcings and not outputs from the model, simulations show a similar story.

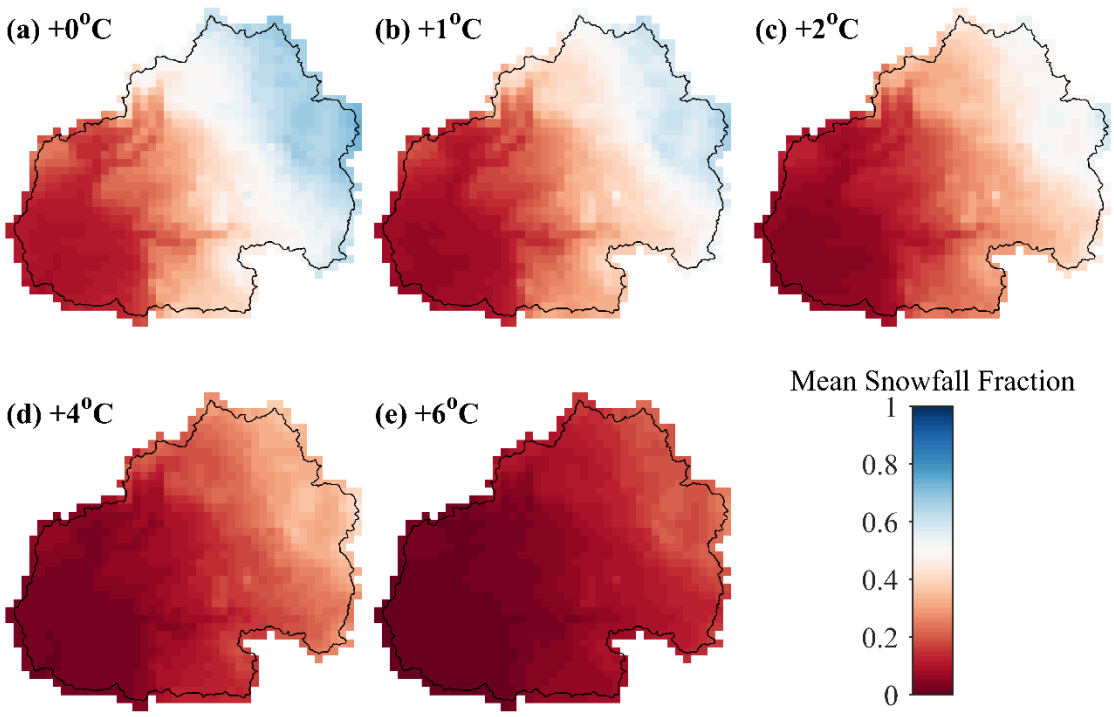

Figure 24. Annual mean snowfall fraction during the cold season for +0, 1, 2, 4, and 6°C of warming (a, b, c, d, and e respectively).

Figure 25 shows the mean monthly snow covered area and snow melt for climate change and forest thinning experiments. Figure 25a shows a large decrease in the magnitude and temporal extent of snow covered area as warming increases. Additionally, the peak snow covered area without warming occurs in January, but after warming the peak is dampened, and is shifted earlier to December. The difference in snow covered area between forest thinning experiments is negligible with small differences at +0°C and +2°C and no discernable difference at +6°C. Although the large decrease in snow covered area with warming the change in snowmelt is not as straightforward. Figure 25b highlights the changes in the volume and timing of snowmelt with both climate change and forest thinning experiments. Peak snowmelt at +0°C occurs in March, but the peak is shifted two months earlier after +2°C of warming, while the shift from +2 to +6°C is only

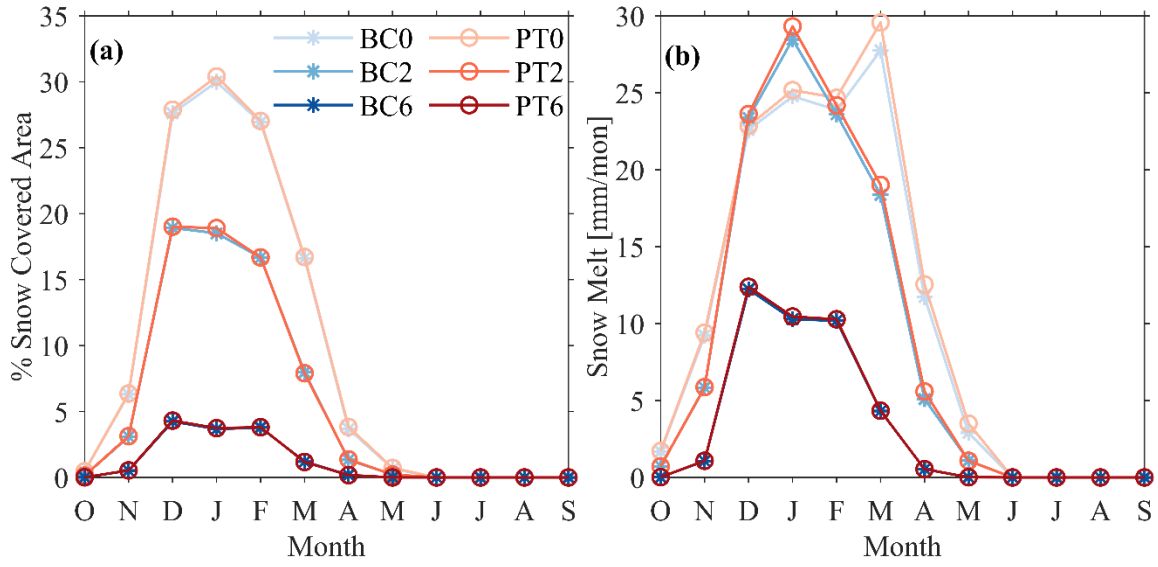

Figure 25. (a) Mean monthly percent snow covered area and (b) mean monthly total snowmelt for the Base Case and Post-treatment scenarios at +0, 2, and 6° of warming.

one month earlier. Interestingly, the magnitude of peak snowmelt is approximately the same at +0°C and +2°C, but the change in snowmelt volume from +0°C to +2°C is a loss of approximately 20 mm annually. Only considering snow covered area, one might expect a loss of snowmelt volume greater than 20 mm, but snowmelt is not indicator of snowpack formation. After warming, snowfall still occurs but is more likely to experience rapid melt shortly after reaching the ground surface. Peak winter precipitation in the Beaver Creek occurs in December and January for the cold season and the warming scenarios shorten time between peak precipitation and peak snowmelt. This shifts peak snowmelt away from the late cold season (March and April) when energy-driven evaporative losses are higher. Forest thinning scenarios do show an increase in snowmelt, specifically with no warming. As warming increases, the differences between the Base Case and Post-treatment snowmelt is reduced. The increase

in the post-treatment scenario can be attributed to reductions in canopy and ground sublimation and increased exposure to solar radiation after the removal of canopy cover which can speed up snowmelt. These changes in snow processes are critical to understanding how subsequent hydrologic processes like evapotranspiration and streamflow are changing.

4.2.2 Changes in Evapotranspiration

Figure 22 showed that total evapotranspiration is decreased in the post-treatment experiments for all levels of warming but does increase with warming in a fashion similar to the Base Case. To understand these changes, I first looked at the relative change in the components that make up total evapotranspiration, shown in Figure 26. Figure 26 shows that for both forest treatment experiments, the percent change in canopy *ET* increases at faster rate with respect to warming than soil E. Soil E is controlled by the soil moisture in the top 100 mm of the soil column and when the soil moisture is low the soil becomes stressed reducing evaporation rates, although the potential *ET* might be high. Comparatively, vegetation can withdraw from the top 1000 mm of the soil column, allowing for vegetation access water stored within the saturated zone. At higher levels of warming this effect is accelerated as the surface soil becomes drier, constraining soil evaporation. The reduction in canopy *ET* in the post-treatment scenario is attributed mainly to the reduction of vegetation fraction which reduces the total area over which ET from the canopy can occur. In addition, the reduction in the free throughfall coefficient and canopy storage reduce the amount of precipitation that can be intercepted in the canopy, reducing the amount of wet canopy evaporation.

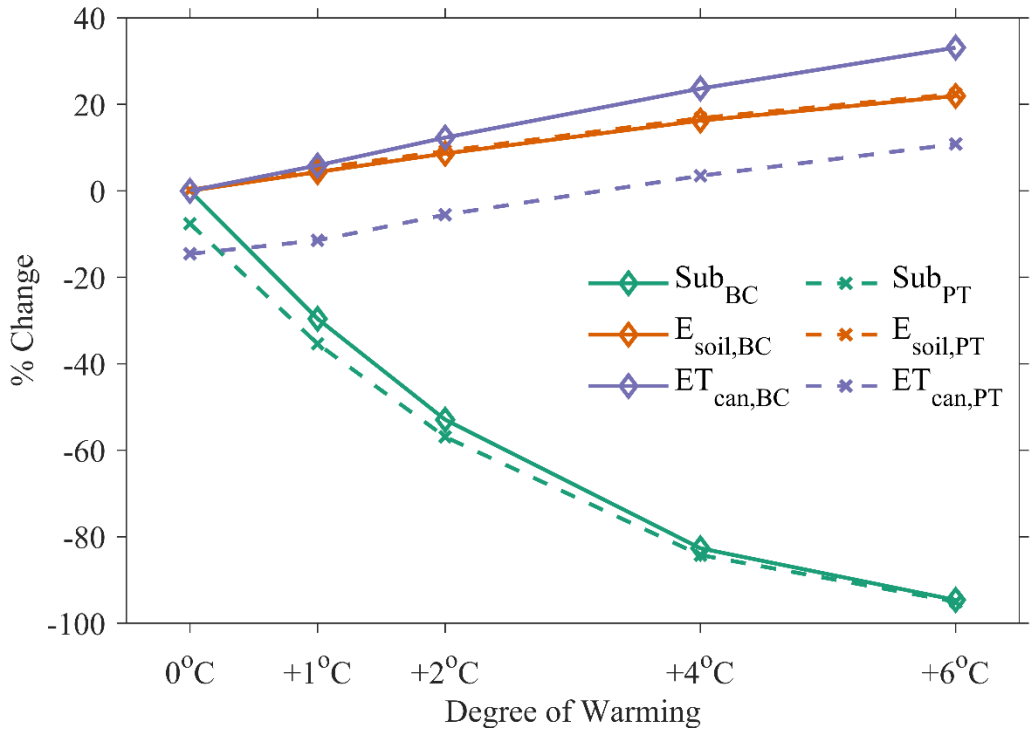

Figure 26. Percent change in components of basin scale total evapotranspiration for the climate change and forest thinning experiments.

In addition, Figure 26 shows that the largest relative change of the *ET* components due to warming is total sublimation. This is due to warming decreasing the total amount of snowfall into the canopy or onto ground, but also speeding up snowmelt at lower levels of warming, reducing time where sublimation can occur. Although the relative change is large, total sublimation only accounts for approximately 12% of the average annual *ET* across the watershed but at higher elevations can become a more important component of total *ET*. The reduction in total sublimation in the post-treatment scenario is due to two factors. First, the reduced vegetation fraction results in more snowfall reaching the ground surface. Ground sublimation rates are much lower than the rates in the canopy. Second, lower vegetation fraction and optical transmission coefficient result

in less sheltering of the ground snowpack from solar radiation which in turn speeds up snow melt, reducing the amount of time when sublimation can occur.

The effect of reduced snow sublimation is also visible in the time series of monthly ET, shown in Figure 27. The difference in the mid-cold season *ET* (DEC-FEB) between the Base Case and Post-treatment does not change significantly as warming increases. However, during the warm season, when peak *ET* rates occur is where the largest difference between the Base Case and Post-treatment occurs. Considering only the climate change experiments, the lowest monthly *ET* occurring in November is shifted up after warming. December and January *ET* rates at +2°C are lower than +0°C by a small amount while +6°C is an increase over all months. The lower cold season rates at +2°C indicate that although less snow is falling, because energy-driven evaporative demands are lower during those months the net effect is reduced overall *ET*. This can explain why BC1 shows a small increase in streamflow over BC0 (Figure 22). During the warm season, total *ET* shows larger increases compared to the cold season due to warming which enforces the idea that the reduced cold season *ET* at +1 and +2°C is a consequence of reduced snow sublimation. Furthermore, months March, April and May *ET* rates show the largest increase across any months with respect to warming, as shown in Figure 27d. Interestingly, this increase only becomes meaningful at +4 and +6°C of warming. At +4 and +6°C such small amount of snow coverage is happening during these months that soil evaporation can now occur when previously at lower levels of warming there was snow coverage until late April (Figure 25b).

Although *ET* increases with warming not all of the watershed shows increasing *ET* with respect to warming, illustrated by the spatial maps in Figure 28.

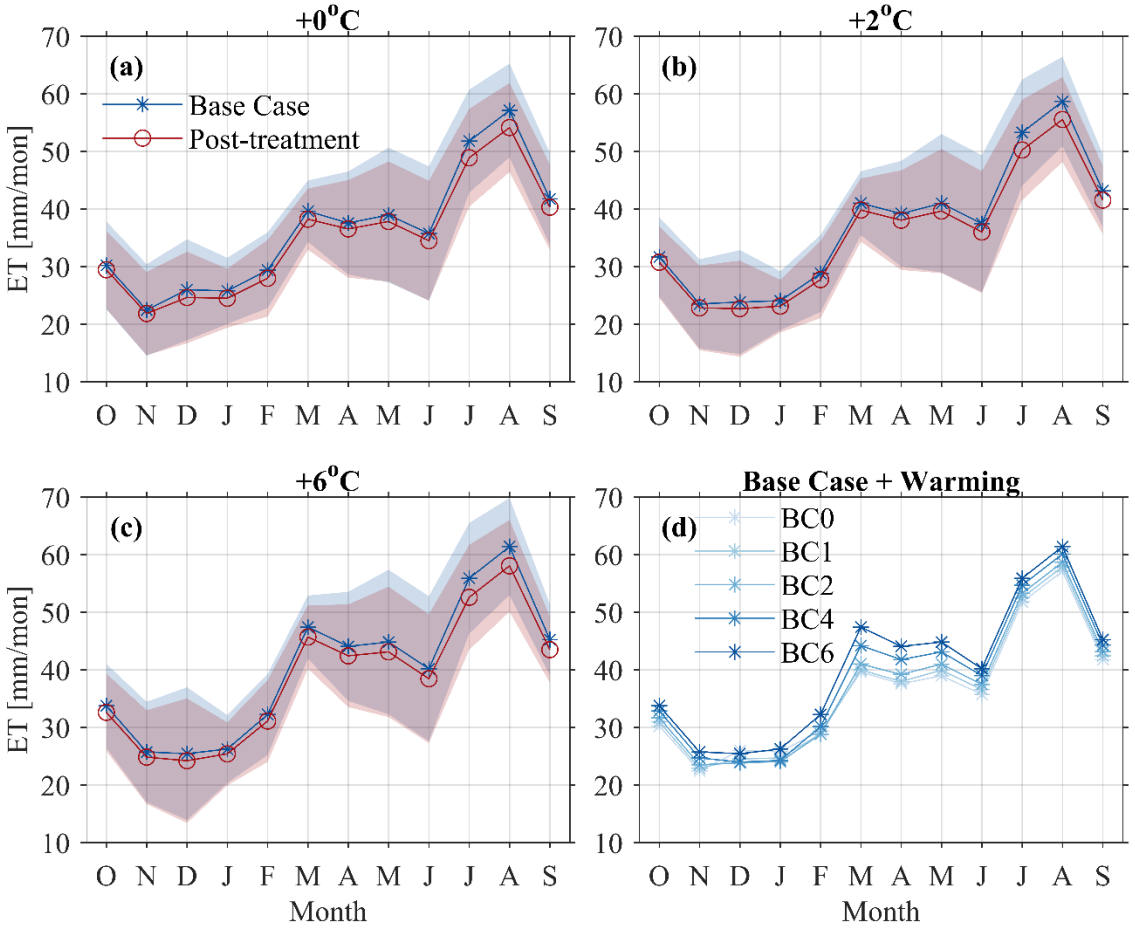

Figure 27. Total evapotranspiration results for warming and forest thinning experiments in the Beaver Creek for 16 years for +0, +2, and +6°C of warming (a, b, and c respectively) and (d) Base Case with warming experiments. Results are shown as monthly means with shaded curves representing ±1 standard deviation from the mean.

Subplots b and c show that from +0 to +1°C total *ET* at higher elevations actually decreases with warming while the areas below increase. The areas that have the greatest decreases are primarily ponderosa pine and receive the most snow. At higher levels of warming, *ET* increases across the entire watershed (Subplot d and e) because at these levels of warming there is little to no continuous snow covered area (Figure 25). Thus, the effect of reduced sublimation is missing at higher levels of warming. Considering

only the forest thinning scenarios, Figure 28a shows that total *ET* decreases in the ponderosa pine forest as expected but not uniformly across the watershed. Locations near and around channels within and downstream of the ponderosa pine forest show increases in total *ET*. This topographic control on *ET* can be explained by the additional runoff that is reaching the channel post-treatment. Another finding from Figure 28a is the lateral connectivity between land cover classes, indicated by the reduction of post-treatment *ET* downstream from the ponderosa pine in the desert shrubland land cover class.

A commonly used way to look at how hydrologic processes are controlled by topography is the Topographic Index (TI) (Beven & Kirkby, 1979). TI is a measure of flow accumulation at a point and is a function of upstream catchment area and slope. Figure 29 shows the total *ET* versus the TI along with the relative frequency of TI for the ponderosa pine forest. Lower values of TI correspond to higher slope areas that have low contributing area (hillslopes near basin boundary), while higher values of TI represent flatter areas with large contributing areas near channels. The relative frequency of TI shows that within the ponderosa pine, the majority of the area has low contributing area and is away from channels, which is expected from the map of elevation (Figure 1). The key takeaway from Figure 25 is that as TI increases the difference between the Base Case and Post-treatment experiment total *ET* decreases. This is in agreement with the spatial maps shown in Figure 28, subplot a that show an increase in *ET* in and around channels after thinning and large reductions in *ET* in hillslopes with low contributing area. Not shown here but if sublimation is removed from the calculation of total *ET* Figure 29 would show higher *ET* at TI values above 15. Although, overall total *ET* is reduced across the ponderosa pine as more areas have lower TI.

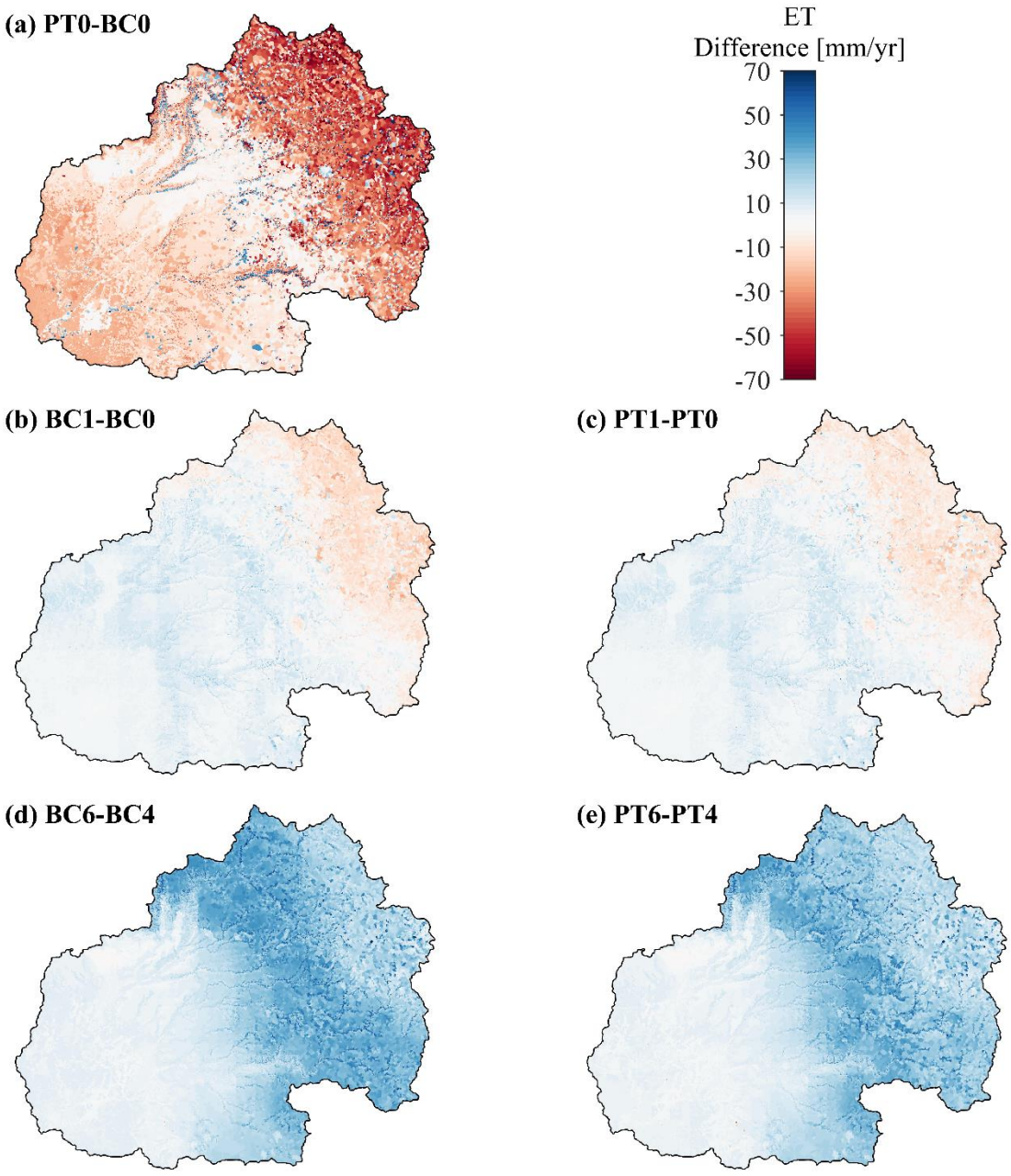

Figure 28. Difference maps of mean annual total evapotranspiration between (a) forest thinning experiments and (b, c, d, and e) climate change scenarios.

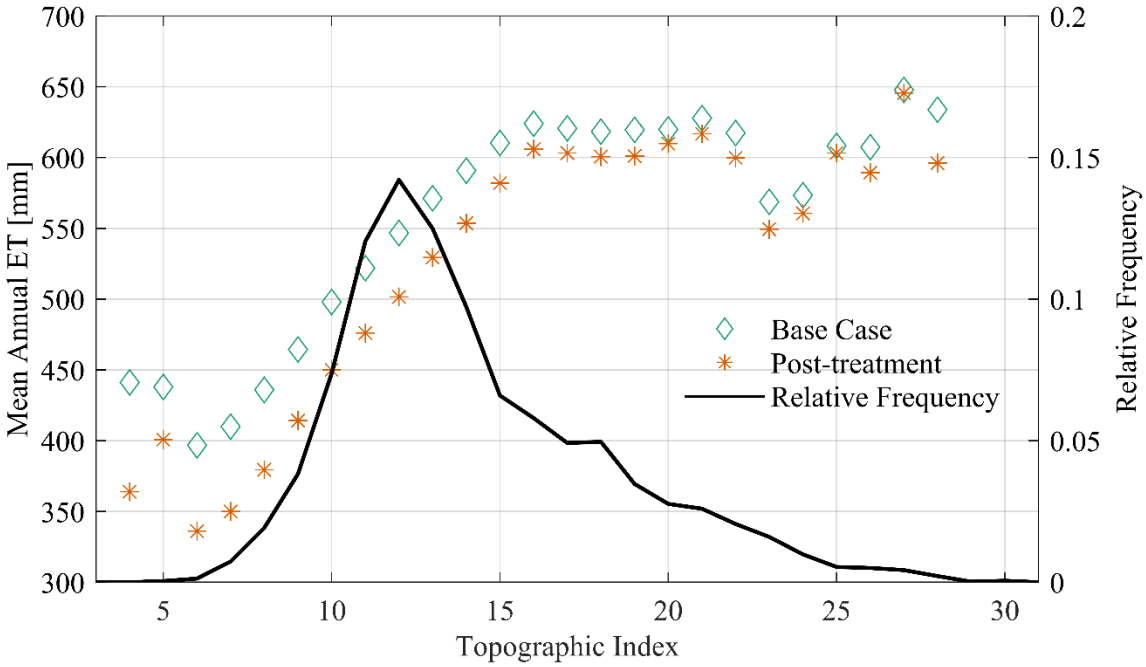

Figure 29. Modeled total evapotranspiration in the ponderosa pine forest compared to topographic index along with relative frequency of topographic index. Results shown for total evapotranspiration were averaged to integer values of topographic index.

4.2.4 Changes in Streamflow

Figure 30 shows that annual streamflow decreased with respect to warming and increased after forest thinning across all levels of warming when compared to the Base Case. A commonly used method of showing differences in streamflow volume due to forest thinning is the use of double mass curves (Searcy and Hardison, 1960; Biederman et al., 2015). Double mass curves in Figure 30 show how cumulative annual streamflow depth from the scenarios change over the 16 year simulation period. Note that each marker represents an individual water year streamflow. Interestingly, PT0, PT1, and PT2 all show very similar values of cumulative streamflow with PT1 have the largest value, 125mm more streamflow over BC0. The forest thinning experiment with the highest level

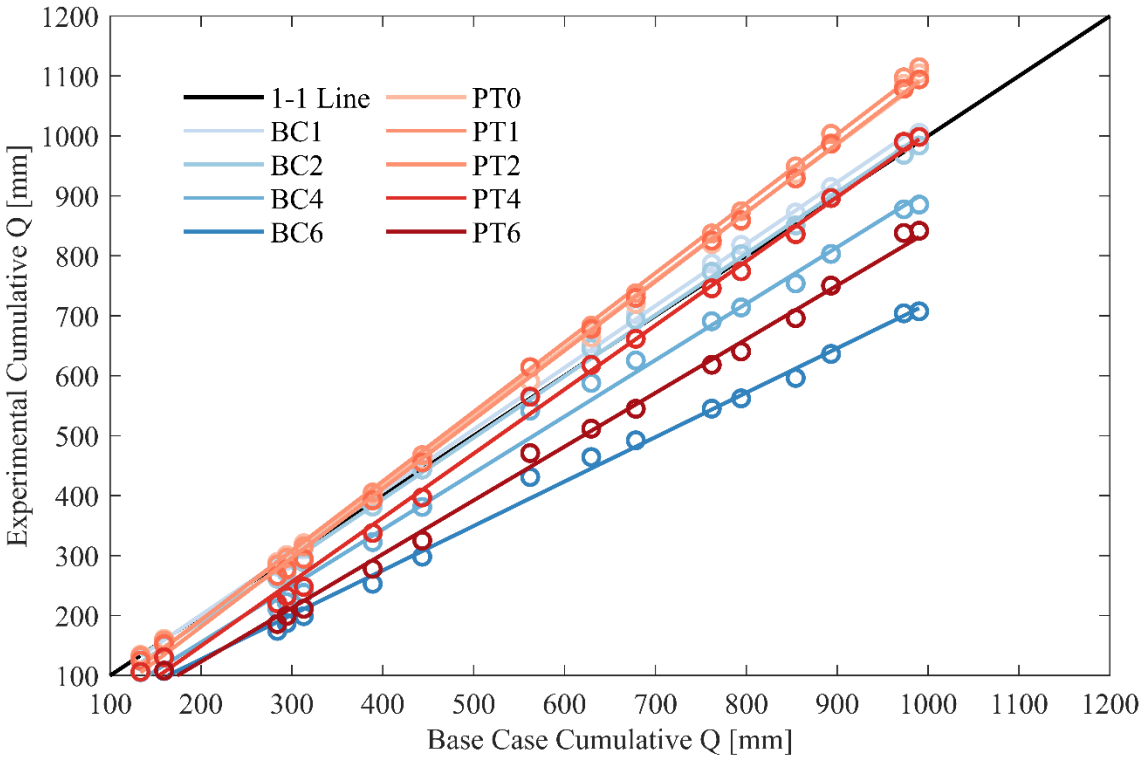

Figure 30. Double mass curves of cumulative annual streamflow for experiments as compared to Base Case. Solid lines are linear regressions for each simulation experiment.

of warming where is no loss in streamflow compared to BC0 is PT4 but initially PT4 had lower cumulative streamflow until WY2010. The most significance difference between two experiments at the same level of warming is BC6 and PT6 with PT6 experiencing 135 mm of additional streamflow.

As noted above increases in annual streamflow are not uniform across all water years. To further examine this, annual streamflow is plotted against annual precipitation, shown in Figure 31. The relationship between annual streamflow and precipitation shows some interesting results. First, water years with low precipitation show little to no difference from the base case for climate change and forest thinning experiments. The majority of water leaving the watershed during these years is from evapotranspiration. As

annual precipitation increases, the difference between the experiments becomes noticeable. Water years near the mean annual precipitation of 520 mm show the greatest difference in streamflow between the experiments. This can also be seen from the regression lines on the plot that are the average across the climate change experiments for the Base Case and Post-treatment. As precipitation increases, the differences between forest thinning experiments are reduced. Furthermore, the largest annual precipitation of the 16 year period, WY2005 shows a decrease in streamflow compared to other years. This year was considered an outlier, WY2005 was an extremely wet year but warm thus had an average snowpack with a lot of rain. There are two main explanations for this behavior. first, the precipitation events during the cold season in WY2005 are smaller in magnitude but spread out temporally which results in less infiltration excess runoff being generated and more infiltration occurring. Second, due to the warmer temperatures in WY2005 and the method for reducing saturated hydraulic conductivity using air temperatures allowed large amount of infiltration to occur. Another interesting year is WY2010 with 627 mm of precipitation which shows that the lowest streamflow is from BC0. Under warming conditions, the atmospheric river event is shifted from snow to rain, resulting in overall increased streamflow. Most of the precipitation that fell during WY2010 is the result of an atmospheric river event which Robles et al. (2021) highlights as able to generate large amounts of streamflow even under climate change. This plot is useful for water managers who can use predictions of future climate to estimate the amount of streamflow under warming or the potential benefits of forest thinning.

Another important aspect of streamflow to water managers is the timing of peak flows from snowmelt. Figure 32 shows mean monthly streamflow for the climate change

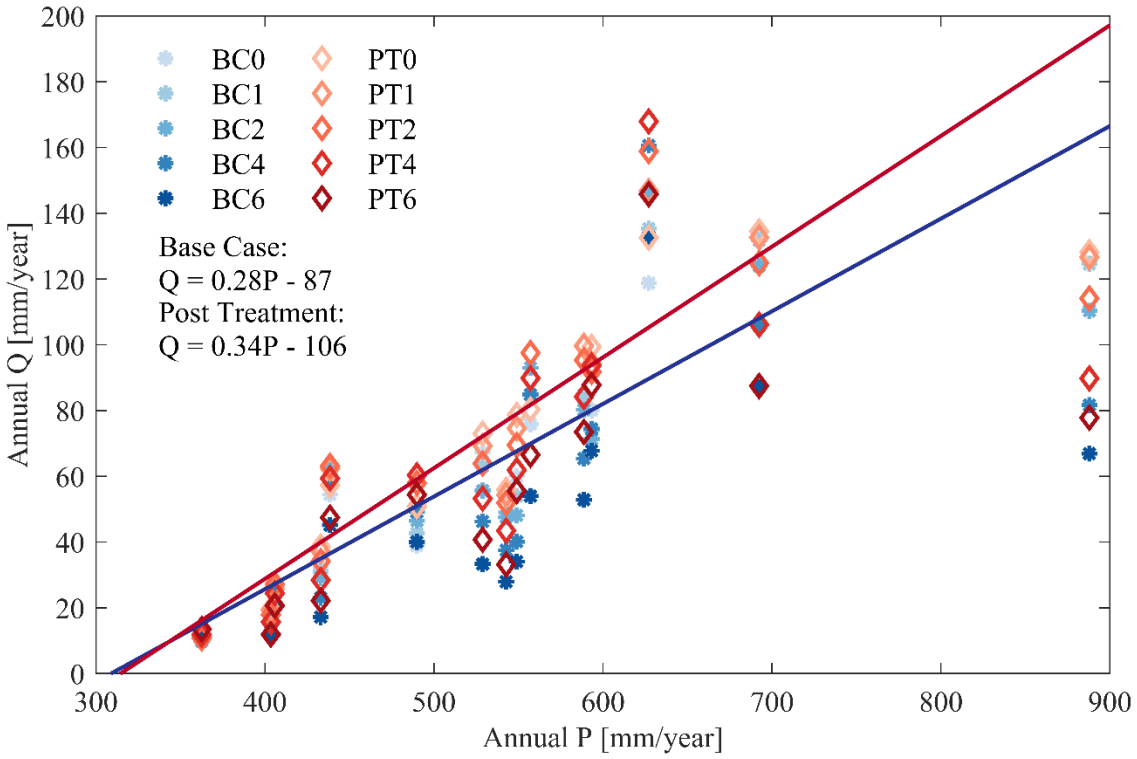

Figure 31. Annual modeled streamflow compared against annual precipitation over a 16 year period for the 10 simulation experiments. Solid lines represent linear regressions across the climate change scenarios for the Base Case and Post-treatment experiments. Note that WY2005 was not used in the calculation of the regression equations due to the large under simulation during that year.

experiments and after forest thinning. Peak streamflow timing during the cold season shifts earlier in the season where the majority of cold season precipitation falls in December and January as warming increases. Furthermore, the magnitude of peak streamflow increases under warming although mean annual streamflow decreases (Figure 22). The temporal shift of streamflow does not occur during the warm season because streamflow production during these seasons is the result of high intensity precipitation events from the North American Monsoon. However, the magnitude and variability of streamflow during the warm season does decrease with warming which can be attributed

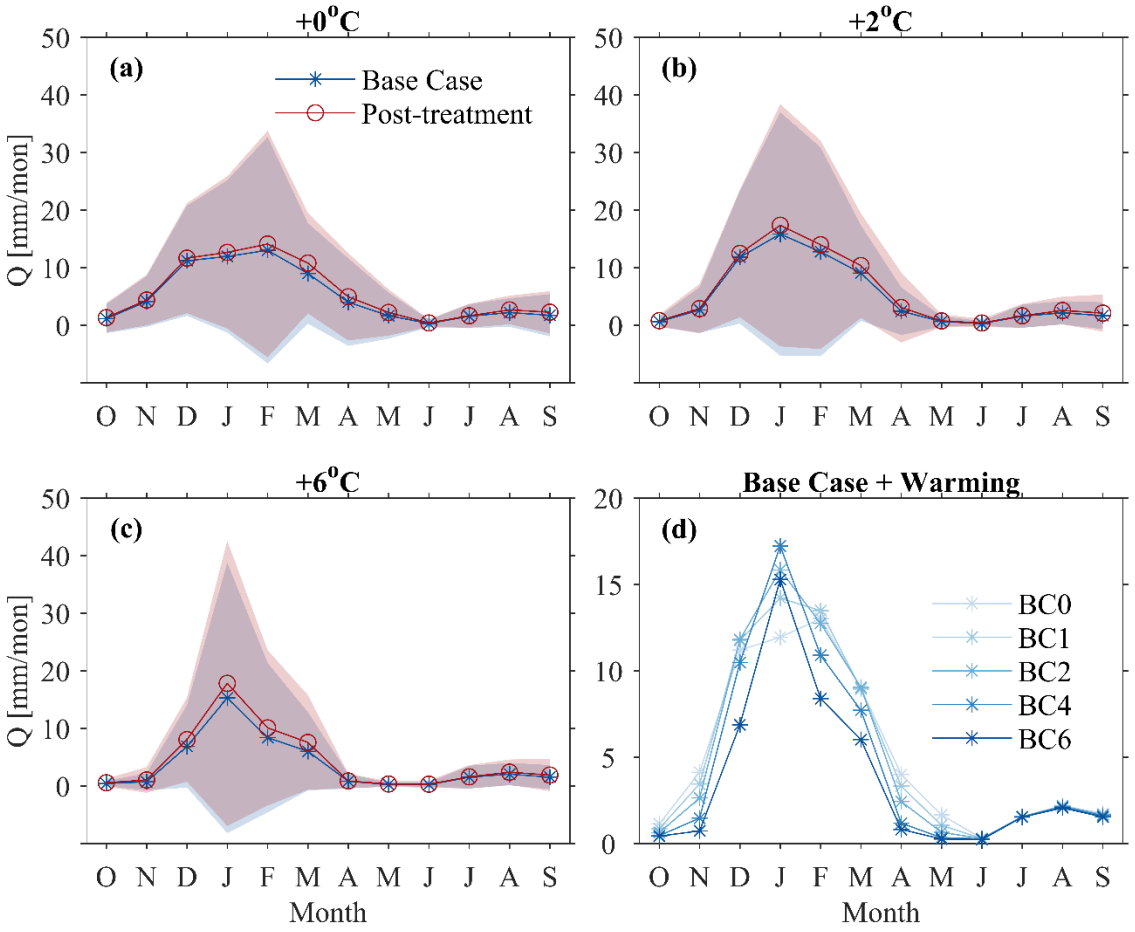

Figure 32. Streamflow results for warming and forest thinning experiments in the Beaver Creek for 16 years for +0, +2, and +6°C of warming (a, b, and c respectively) and (d) Base Case with warming experiments. Results are shown as monthly means with shaded curves representing ±1 standard deviation from the mean.

to higher rates of evapotranspiration. Forest thinning has little to no effect on monthly streamflow during the warm season across warming scenarios. Surprisingly, the greatest difference between the Base Case and Post-treatment experiments occurs at +6°C of warming during the cold season. These results indicates that at least for cold season streamflow the benefit of forest thinning increases with warming.

5 CONCLUSIONS & FUTURE WORK

This study investigated the impacts of climate change and forest thinning on a watershed in Central Arizona. The study consisted of three parts: (1) preparation of a set of model forcings that account for the controls of complex terrain on meteorological conditions, (2) expansion of an established model to long term simulations of both warm and cold seasons with good to excellent model performance in those seasons, and (3) employment of the model to simulate warming due to climate change and forest thinning.

In this study, model forcings were prepared using multiple methods and a combination of station observations and raster-based datasets. Precipitation forcing was composed of a base dataset, NEXRAD weather radar, that was bias corrected using localized lapse rates computed from gauges in the watershed. Meteorological forcings were prepared by applying spatial interpolation methods that account for topography using weather stations within and near the study area. Special importance was placed on the interpolation of air temperature due to its importance to the modelling of snowpack dynamics. To accomplish this, localized air temperature lapse rates from the PRISM dataset were used in the spatial interpolation algorithm.

Model calibration and validation in this work began with the simulation of snow water equivalent at two SNOTEL stations within the watershed. These simulations demonstrated the model ability to simulate the temporal and spatial variability among the stations and provided a set of initial snow model parameters for basin scale simulations. The model performed well in simulating small snowpacks at Bar-M SNOTEL when using the same parameter set derived from Happy Jack SNOTEL. Modelling efforts expanded to basin scale simulations of SWE by comparison of modeled results to a an

estimated SWE based on remote sensing observations. Comparisons evaluated the model ability to simulate the temporal and spatial patterns of SWE. The model demonstrated good performance in simulating the unique temporal patterns of snow accumulation and ablation during any given water year over a 16 year period. tRIBS also showed the ability to model the SWE versus elevation relation in the watershed as compared to SWANN. However, model performance of overall SWE magnitude for both the calibration and validation periods showed an average undersimulation of SWE by ~30%. The reason for this undersimulation is due mainly to the quality of precipitation and air temperature forcing. Specifically, a lack of weather stations in the mid-elevations of the watershed.

Streamflow simulation at the basin scale used two interior streamflow gauges within the watershed for calibration and validation. Model results showed good performance in capturing the high variability of streamflow at both the intra-annual and interannual scales. Specifically, performance for distinct cold and warm season streamflow improved after the incorporation of methods to account for the effects of frozen soil on runoff. However, the wettest years in the simulation period showed the largest undersimulation of streamflow volume due to large amounts of infiltration. Nonetheless, the model showed good performance in the volume and timing of streamflow for the majority of water years in the 16 year simulation period for both Wet and Dry Beaver Creek.

Simulation experiments were developed that account for the separate and combined effects of warming due to climate change and forest thinning. Warming experiments used a simple method of adding uniform temperature increases to the forcing data without the consideration of other meteorological variables. While forest thinning

was accounted for by incorporating a dataset from the 4FRI to calculate adjusted land cover parameters for the model. The goal of these experiments was not to provide an exact representation of the future conditions but to provide insight into the sensitivity of hydrologic processes in the Beaver Creek to these changes.

Warming experiments showed a large decrease in the annual average snowfall fraction across the watershed accompanied by decreases in the watershed average snow covered area and snowmelt. Total evapotranspiration increased overall with the largest increases occurring during March, April, and May. These increases were not spatially uniform, at lower levels of warming total evapotranspiration decreased in the ponderosa pine forest due to the reduction of snowfall and faster snowmelt which reduced the amount of time in which sublimation could occur. Earlier snowmelt and less snowfall also had significant impacts on streamflow volume and timing. At +6°C of warming total annual streamflow decreased by 28% annually while the timing of peak streamflow shifted from March and February to January.

Forest thinning showed generally the same pattern of changes with respect to climate change. After thinning, the watershed experienced increased snowmelt volume accompanied by decreased in evapotranspiration and increased streamflow. Flatter regions with low contributing area within the ponderosa pine forest experienced the greatest reduction in evapotranspiration, while channels downstream and within the ponderosa pine forest showed the increases in annual evapotranspiration. While not addressed in this study, these results suggest that the increased presence of water in channels could promote vegetation growth in those areas overtime, reducing the net effect of thinning. Across all levels of warming, streamflow increased by approximately

12% after thinning which shifted the point at which streamflow is reduced below the Base Case until +4°C of warming. In years with low annual precipitation the difference between scenarios is negligible but as precipitation nears the annual average forest thinning shows increased streamflow volumes.

The limitations to these modeling efforts should be noted. For model calibration of SWE the calibration relied on the use of SWANN which in itself is the output from a model but was necessary due to the lack of observational datasets. Furthermore, streamflow was calibrated using the two interior stream gauges which left a subsection of soil parameters near the outlet of the model relatively uncalibrated. The simulation experiments while based on predicted (warming) and planned (4FRI) changes to the environment, the representation of these in the model used simpler methods that were feasible to complete.

This study showed the ability of the tRIBS model to simulate a semi-arid regional watershed in Central Arizona while accounting for both cold and warm season processes over the long-term. The novelty lies in the ability for distributed, physically-based models to simulate the high temporal and spatial resolution hydrologic processes at the watershed scale with relatively short simulation times. Other commonly used hydrologic model like WRF-HYDRO or HEC-HMS could be used to complete similar studies but they lack the physically-based parameterization that simulate hydrologic processes within tRIBS. Furthermore, lumped model like HEC-HMS lack the ability to look at fine spatial scale changes that aid in characterizing the response to stressors like warming due to climate change and forest thinning

While the Beaver Creek is characteristic of the surrounding Mogollon rim transition zone there is value in expanding the work done here to the greater region like the Verde River watershed due to its importance to the Phoenix Metro Area's water supply. A similar set of experiments to the work here could be examine that incorporate the most recent estimates of future changes in climate from the Couple Model Intercomparison Project Phase 6. Applying a fully-distributed, physically based in a project of this scope has yet to be done in this region and would require the use of spatially distributed datasets for the parameterization of the model like the work in Ko et al., (2019). Such work has potential to yield novel results and advance the state of knowledge of climatic impacts on the hydrologic response in the southwest.

On a similar note, expanding modelling efforts to a larger watershed like the Verde River could yield an experimental design of forest thinning that better represents how forest thinning would be conducted in the real world. Post-treatment conditions are not static in time and forest thinning does not occur at one uniform timestep. Therefore, while one area is undergoing thinning the previously thinned areas have begun to regrow, potentially reducing the net effect of thinning. Completing large scale projects like 4FRI takes decades and couple this with the idea that the transformation of precipitation to streamflow is much more complex in a watershed such as the Verde River than in the Beaver Creek. Furthermore, work needs to be done on assessing the hydrologic impacts of the vegetation types that will replace the removed vegetation after thinning like native grasses. These ideas highlight the fact that the results shown here in this study are not directly scalable to larger watersheds in the region but due to the importance of the Salt-Verde system to Phoenix's water supply they warrant their own study.

REFERENCES

Adam, J. C., Hamlet, A. F., & Lettenmaier, D. P. (2009). Implications of global climate change for snowmelt hydrology in the twenty-first century: Moutain hydroclimatology and snow seasonality. Hydrological Processes, 23(7), 962–972.

Allard, W. (1957). Snow Hydrology: Summary Report of the Snow Investigations. Published by the North Pacific Division, Corps of Engineers, U.S. Army, Portland, Oregon, 1956. 437 pages, 70 pages of plates, maps and figs., 27 cm. Journal of Glaciology, 3(22), 148–. https://doi.org/10.1017/S0022143000024503

Allen, C. D., Savage, M., Falk, D. A., Suckling, K. F., Swetnam, T. W., Schulke, T., Stacey, P. B., Morgan, P., Hoffman, M., & Klingel, J. T. (2002). Ecological Restoration of Southwestern Ponderosa Pine Ecosystems: A Broad Perspective. Ecological Applications, 12(5), 1418–1433. https://doi.org/10.1890/1051-0761(2002)012[1418:EROSPP]2.0.CO;2

Baker, M. B. (1986). Effects of Ponderosa Pine Treatments on Water Yield in Arizona. Water Resources Research, 22(1), 67–73. https://doi.org/10.1029/WR022i001p00067

Baker, M. B. (1982). Hydrologic regimes of forested areas in the Beaver Creek watershed. Rocky Mountain Forest and Range Experiment Station, Forest Service, Forest Service, U.S. Dept. of Agriculture.

Bales, R. C., Molotch, N. P., Painter, T. H., Dettinger, M. D., Rice, R., & Dozier, J. (2006). Mountain hydrology of the western United States. Water Resources Research, 42(8), W08432–n/a. https://doi.org/10.1029/2005WR004387

Barnes, S. L. (1994). Applications of the Barnes Objective Analysis Scheme. Part I: Effects of Undersampling, Wave Position, and Station Randomness. Journal of Atmospheric and Oceanic Technology, 11(6), 1433–1448. https://doi.org/10.1175/1520-0426(1994)011<1433:AOTBOA>2.0.CO;2

Beven, J. K., & Kirkby, J. M. (1979). A physically based, variable contributing area model of basin hydrology. Hydrological Sciences Bulletin, 24:1, 43-69. https://doi.org/10.1080/02626667909491834

Beven, J. K. (1984). Infiltration into a class of vertically non-uniform soils. Hydrological Sciences Journal, 29(4), 425–434. https://doi.org/10.1080/02626668409490960

Biederman, J. A., Harpold, A. A., Gochis, D. J., Ewers, B. E., Reed, D. E., Papuga, S. A., & Brooks, P. D. (2014). Increased evaporation following widespread tree mortality limits streamflow response. Water Resources Research, 50(7), 5395–5409. https://doi.org/10.1002/2013WR014994

Biederman, J. A., Somor, A. J., Harpold, A. A., Gutmann, E. D., Breshears, D. D., Troch, P. A., Gochis, D. J., Scott, R. L., Meddens, A. J. H., & Brooks, P. D. (2015). Recent tree die-off has little effect on streamflow in contrast to expected increases from historical studies. Water Resources Research, 51(12), 9775–9789. https://doi.org/10.1002/2015WR01740

Bras, R. L., (1989). Hydrology: An Introduction to Hydrologic Science. Addison-Wesley, Inc.: New York; 660.

Brown, E., Baker, M. B., Rogers, J. J., Clary, P., Kovner, J. L., Larson, F. R., Avery, C., & Campbell, R. E. (1974). Opportunities for increasing water yields and other multiple use values on ponderosa pine forest lands. U.S. Dept. of Agriculture, Forest Service, Rocky Mountain Forest and Range Experiment Station.

Brown, A. E., Zhang, L., McMahon, T. A., Western, A. W., & Vertessy, R. A. (2005). A review of paired catchment studies for determining changes in water yield resulting from alterations in vegetation. Journal of Hydrology (Amsterdam), 310(1), 28–61. https://doi.org/10.1016/j.jhydrol.2004.12.010

Broxton, P. D., Dawson, N., & Zeng, X. (2016). Linking snowfall and snow accumulation to generate spatial maps of SWE and snow depth. Earth and Space Science (Hoboken, N.J.), 3(6), 246–256. https://doi.org/10.1002/2016EA00017

Broxton, P. D., Leeuwen, W. J. D., & Biederman, J. A. (2017). SWANN: The Snow Water Artificial Neural Network Modelling System. American Geophysical Union, Fall Meeting 2017, abstract #C43B-01. https://ui.adsabs.harvard.edu/abs/2017AGUFM.C43B..01B

Broxton, P. D., Leeuwen, W. J. D., & Biederman, J. A. (2019a). Improving Snow Water Equivalent Maps with Machine Learning of Snow Survey and Lidar Measurements. Water Resources Research, 55(5), 3739–3757. https://doi.org/10.1029/2018WR024146

Broxton, P., X. Zeng, & N. Dawson (2019b). Daily 4 km Gridded SWE and Snow Depth from Assimilated In-Situ and Modeled Data over the Conterminous US, Version 1. [Dataset]. NASA National Snow and Ice Data Center Distributed Active Archive Center. https://doi.org/10.5067/0GGPB220EX6A

Cannon, A. J., Sobie, S. R., & Murdock, T. Q. (2015). Bias Correction of GCM Precipitation by Quantile Mapping: How Well Do Methods Preserve Changes in Quantiles and Extremes? Journal of Climate, 28(17), 6938–6959. https://doi.org/10.1175/JCLI-D-14-00754.1

Christensen, N. S., Wood, A. W., Voisin, N., Lettenmaier, D. P., & Palmer, R. N. (2004). The Effects of Climate Change on the Hydrology and Water Resources of the Colorado

River Basin. Climatic Change, 62(1), 337–363. https://doi.org/10.1023/B:CLIM.0000013684.13621.1f

Chojnacky, D., Bentz, B. J., & Logan, J. A. (2000). Mountain Pine Beetle Attack in Ponderosa Pine: Comparing Methods for Rating Susceptibility, RMRS-RP-26. Ogden, UT: U.S. Department of Agriculture, Forest Service, Rocky Mountain Experiment Station.

Cosgrove, B. A., Lohmann, D., Mitchell, K. E., Houser, P. R., Wood, E. F., Schaake, J., & Meng, J. (2003). Real-time and retrospective forcing in the North American Land Data Assimilation System (NLDAS) project. Journal of Geophyscical Research, VOL. 108, 8842.

Crookston, N. L., & Dixon, G. E. (2005). The forest vegetation simulator: A review of its structure, content, and applications. Computers and Electronics in Agriculture, 49(1), 60–80. https://doi.org/10.1016/j.compag.2005.02.003

Department of Water Resources. (2021). Annual Report. Arizona Department of Water Resources. https://new.azwater.gov/sites/default/files/media/7-1_ANNUALREPORT2021_Final.pdf

Desjardins, M., Koch, S. E., & Kocin, P. J. (1983). An Interactive Barnes Objective Map Analysis Scheme for Use with Satellite and Conventional Data. Journal of Climate and Applied Meteorology, 22(9), 1487–1503. https://doi.org/10.1175/1520-0450(1983)022<1487:AIBOMA>2.0.CO;2

Dozier, J., & Frew, J. (1990). Rapid calculation of terrain parameters for radiation modeling from digital elevation data. IEEE Transactions on Geoscience and Remote Sensing, 28(5), 963–969. https://doi.org/10.1109/36.58986

Du, J. (2011). GCIP/EOP Surface: Precipitation NCEP/EMC 4KM Gridded Data (GRIB) Stage IV Data. Version 1.0. UCAR/NCAR - Earth Observing Laboratory. https://doi.org/10.5065/D6PG1QDD.

Elsner, M. M., Cuo, L., Voisin, N., Deems, J. S., Hamlet, A. F., Vano, J. A., Mickelson, K. E. B., Lee, S.-Y., & Lettenmaier, D. P. (2010). Implications of 21st century climate change for the hydrology of Washington State. Climatic Change, 102(1), 225–260. https://doi.org/10.1007/s10584-010-9855-0

Fatichi, S., Vivoni, E. R., Ogden, F. L., Ivanov, V. Y., Mirus, B., Gochis, D., Downer, C. W., Camporese, M., Davison, J. H., Ebel, B., Jones, N., Kim, J., Mascaro, G., Niswonger, R., Restrepo, P., Rigon, R., Shen, C., Sulis, M., & Tarboton, D. (2016). An overview of current applications, challenges, and future trends in distributed process-based models in hydrology. Journal of Hydrology (Amsterdam), 537, 45–60. https://doi.org/10.1016/j.jhydrol.2016.03.026

Fritze, H., Stewart, I. T., & Pebesma, E. (2011). Shifts in Western North American Snowmelt Runoff Regimes for the Recent Warm Decades. Journal of Hydrometeorology, 12(5), 989–1006. https://doi.org/10.1175/2011JHM1360.1

GDAL/OGR contributors (2020). GDAL/OGR Geospatial Data Abstraction software Library. Open Source Geospatial Foundation. https://gdal.org

Gooch, R. S., Cherrington, P. A., & Reinink, Y. (2007). Salt River Project experience in conversion from agriculture to urban water use. Irrigation and Drainage Systems, 21(2), 145–157. https://doi.org/10.1007/s10795-007-9026-2

Goto, H., K. Kikuchi, and M. Kajikawa (2012). Influence of different surface soils on snow-water content and snow type of the snow cover. Japanese Journal of Snow and Ice 74:145–158.

Hammond, J. C., & Kampf, S. K. (2020). Subannual Streamflow Responses to Rainfall and Snowmelt Inputs in Snow-Dominated Watersheds of the Western United States. Water Resources Research, 56(4). https://doi.org/10.1029/2019WR026132

Hampton, H. M., Sesnie, S. E., Bailey, J. D., & Snider, G. B. (2011). Estimating regional wood supply based on stakeholder consensus for forest restoration in Northern Arizona. Journal of Forestry, 109(1), 15–26. https://doi.org/10.1093/jof/109.1.15

Harpold, A. A., Kaplan, M. L., Zion Klos, P., Link, T., McNamara, J. P., Rajagopal, S., Schumer, R., & Steele, C. M. (2017). Rain or snow: Hydrologic processes, observations, prediction, and research needs. Hydrology and Earth System Sciences, 21(1), 1–22. https://doi.org/10.5194/hess-21-1-2017

Hawkins, G. (2012). Assessing the effects of climate change in a semiarid basin utilizing a fully distributed hydrologic model: a case study of Beaver Creek, Arizona. [Masters Thesis, Arizona State University]. https://hdl.handle.net/2286/R.I.15198

Hu, Z., & Islam, S. (1995). Prediction of Ground Surface Temperature and Soil Moisture Content by the Force-Restore Method. Water Resources Research, 31(10), 2531–2539. https://doi.org/10.1029/95WR01650

Huffman, D. W., Zegler, T. J., Fulé, P. Z. (2015) Fire history of a mixed conifer forest on the Mogollon Rim, northern Arizona, USA. International Journal of Wildland Fire 24, 680-689. https://doi.org/10.1071/WF14005

Hussein, A. (2020). Process-Based Calibration of WRF-Hydro Model in Unregulated Mountainous Basin in Central Arizona. [Masters Thesis, Arizona State University]. https://hdl.handle.net/2286/R.I.57310

IPCC. (2021). Climate Change 2021: The Physical Science Basis. Contribution of Working Group I to the Sixth Assessment Report of the Intergovernmental Panel on Climate Change [Masson-Delmotte, V., P. Zhai, A. Pirani, S.L. Connors, C. Péan, S. Berger, N. Caud, Y. Chen, L. Goldfarb, M.I. Gomis, M. Huang, K. Leitzell, E. Lonnoy, J.B.R. Matthews, T.K. Maycock, T. Waterfield, O. Yelekçi, R. Yu, and B. Zhou (eds.)]. Cambridge University Press. In Press.

Ivanov, V. Y., Vivoni, E. R., Bras, R. L., & Entekhabi, D. (2004). Catchment hydrologic response with a fully distributed triangulated irregular network model. Water Resources Research, 40(11), W11102–n/a. https://doi.org/10.1029/2004WR003218

Ko, A., Mascaro, G., & Vivoni, E. R. (2019). Strategies to Improve and Evaluate Physics-Based Hyperresolution Hydrologic Simulations at Regional Basin Scales. Water Resources Research, 55(2), 1129–1152. https://doi.org/10.1029/2018WR023521

Koren, V. (2006). Parameterization of frozen ground effects: sensitivity to soil properties. Predictions in Ungauged Basins: Promises and Progress (Proceedings of Symposium S7 held during the Seventh IAHS Scientific Assembly at Foz do Iquacu, Brazil, April 2005). IAHS Publication 303, 125-133.

Koren, V., Smith, M., & Cui, Z. (2014). Physically-based modifications to the Sacramento Soil Moisture Accounting model. Part A: Modeling the effects of frozen ground on the runoff generation process. Journal of Hydrology (Amsterdam), 519, 3475–3491. https://doi.org/10.1016/j.jhydrol.2014.03.004

Leonard, J. M., Magaña, H. A., Bangert, R. K., Neary, D. G., & Montgomery, W. L. (2017). Fire and Floods: The Recovery of Headwater Stream Systems Following High-Severity Wildfire. Fire Ecology, 13(3), 62–84. https://doi.org/10.4996/fireecology.130306284

Leung, L. R., & Wigmosta, M. S. (1999). POTENTIAL CLIMATE CHANGE IMPACTS ON MOUNTAIN WATERSHEDS IN THE PACIFIC NORTHWEST. Journal of the American Water Resources Association, 35(6), 1463–1471. https://doi.org/10.1111/j.1752-1688.1999.tb04230.x

Liston, G. E., & Elder, K. (2006a). A Distributed Snow-Evolution Modeling System (SnowModel). Journal of Hydrometeorology, 7(6), 1259–1276. https://doi.org/10.1175/JHM548.1

Liston, G. E., & Elder, K. (2006b). A Meteorological Distribution System for High-Resolution Terrestrial Modeling (MicroMet). Journal of Hydrometeorology, 7(2), 217–234. https://doi.org/10.1175/JHM486.1

Liu, J., Zhou, Z., Yan, Z., Gong, J., Jia, Y., Xu, C.-Y., & Wang, H. (2019). A new approach to separating the impacts of climate change and multiple human activities on water cycle processes based on a distributed hydrological model. Journal of Hydrology (Amsterdam), 578, 124096–. https://doi.org/10.1016/j.jhydrol.2019.124096

Livneh, B., Deems, J. S., Schneider, D., Barsugli, J. J., & Molotch, N. P. (2014). Filling in the gaps: Inferring spatially distributed precipitation from gauge observations over complex terrain. Water Resources Research, 50(11), 8589–8610. https://doi.org/10.1002/2014WR015442

Lopes, A., Girona-García, A., Corticeiro, S., Martins, R., Keizer, J. ., & Vieira, D. C. . (2021). What is wrong with post-fire soil erosion modelling? A meta-analysis on current approaches, research gaps, and future directions. Earth Surface Processes and Landforms, 46(1), 205–219. https://doi.org/10.1002/esp.5020

MacDonald, G. M. (2010). Water, climate change, and sustainability in the southwest. Proceedings of the National Academy of Sciences - PNAS, 107(50), 21256–21262. https://doi.org/10.1073/pnas.0909651107

MacEachern, D., Person D. (2021). Arizona heads into Tier 1 Colorado River Shortage for 2022. Central Arizona Project, Press Release. https://library.cap-az.com/documents/public-information/ADWR-CAP-PressRelease-Arizona_Tier%201_Colorado_River_Shortage_2022-081321.pdf

Mahmood, T. H., & Vivoni, E. R. (2011). A climate-induced threshold in hydrologic response in a semiarid ponderosa pine hillslope. Water Resources Research, 47(9). https://doi.org/10.1029/2011WR010384

McCabe, G. J., Wolock, D. M., & Valentin, M. (2018). Warming is Driving Decreases in Snow Fractions While Runoff Efficiency Remains Mostly Unchanged in Snow-Covered Areas of the Western United States. Journal of Hydrometeorology, 19(5), 803–814. https://doi.org/10.1175/JHM-D-17-0227.1

Moir, W. H., Geils, B. W., Benoit, M., & Scurlock, D. (1997). Ecology of southwestern ponderosa pine forests. Gen. Tech. Rep. RM-292. U.S. Deptartment of Agriculture, Forest Service, Rocky Mountain Forest and Range Experiment Station.

Monteith, J. L. (1965). Evaporation and environment. Symposia of the Society for Experimental Biology, 19, 205-34.

Moreno, H. A., Gupta, H. V., White, D. D., & Sampson, D. A. (2016). Modeling the distributed effects of forest thinning on the long-term water balance and streamflow extremes for a semi-arid basin in the southwestern US. Hydrology and Earth System Sciences, 20(3), 1241–1267. https://doi.org/10.5194/hess-20-1241-2016

Mote, P. W., Hamlet, A. F., Clark, M. P., & Lettenmaier, D. P. (2005). DECLINING MOUNTAIN SNOWPACK IN WESTERN NORTH AMERICA. Bulletin of the American Meteorological Society, 86(1), 39–49. https://doi.org/10.1175/BAMS-86-1-39

National Resource Conservation Service. (1977). *SNOwpack TELemetry Network* [Dataset]. United States Department of Agriculture.

National Resource Conservation Service. (2010). Ground Frost Depth Map [Dataset]. Arizona National Resource Conservation Service State Headquarters. https://efotg.sc.egov.usda.gov/references/public/AZ/Frost_depth.pdf

Nayak, A., Marks, D., Chandler, D. G., & Seyfried, M. (2010). Long-term snow, climate, and streamflow trends at the Reynolds Creek Experimental Watershed, Owyhee Mountains, Idaho, United States. Water Resources Research, 46(6). https://doi.org/10.1029/2008WR007525

Nemec, J., & Schaake, J. (1982). Sensitivity of water resource systems to climate variation. Hydrological Sciences Journal, 27(3), 327–343. https://doi.org/10.1080/02626668209491113

Penman, H. L. (1948). Natural Evaporation from Open Water, Bare Soil and Grass. Proceedings of the Royal Society of London. Series A, Mathematical and Physical Sciences, 193(1032), 120–145. https://doi.org/10.1098/rspa.1948.0037

Phillips, D. H., Reinink, Y., Skarupa, T. E., Ester III, C. E., & Skindlov, J. A. (2009). Water resources planning and management at the Salt River Project, Arizona, USA. Irrigation and Drainage Systems, 23(2-3), 109–124. https://doi.org/10.1007/s10795-009-9063-0

Picotte, J. J., Dockter, D., Long, J., Tolk, B., Davidson, A., & Peterson, B. (2019). LANDFIRE Remap Prototype Mapping Effort: Developing a New Framework for Mapping Vegetation Classification, Change, and Structure. Fire (Basel, Switzerland), 2(2), 35–. https://doi.org/10.3390/fire2020035

Pitman, J. I. (1989). Rainfall interception by bracken in open habitats — Relations between leaf area, canopy storage and drainage rate. Journal of Hydrology (Amsterdam), 105(3), 317–334. https://doi.org/10.1016/0022-1694(89)90111-X

PRISM Climate Group. (1994). Parameter-elevation Regressions on Independent Slopes Model [Dataset]. Oregon State University. https://prism.oregonstate.edu/

Rasmussen, R., Baker, B., Kochendorfer, J., Meyers, T., Landolt, S., Fischer, A. P., Black, J., Thériault, J. M., Kucera, P., Gochis, D., Smith, C., Nitu, R., Hall, M., Ikeda, K., & Gutmann, E. (2012). How Well Are We Measuring Snow: The NOAA/FAA/NCAR

Winter Precipitation Test Bed, Bulletin of the American Meteorological Society, 93(6), 811-829. https://journals.ametsoc.org/view/journals/bams/93/6/bams-d-11-00052.1.xml

Rinehart, A. J., Vivoni, E. R., & Brooks, P. D. (2008). Effects of vegetation, albedo, and solar radiation sheltering on the distribution of snow in the Valles Caldera, New Mexico. Ecohydrology, 1(3), 253–270. https://doi.org/10.1002/eco.26

Robles-Morua, A., Vivoni, E. R., & Mayer, A. S. (2012). Distributed Hydrologic Modeling in Northwest Mexico Reveals the Links between Runoff Mechanisms and Evapotranspiration. Journal of Hydrometeorology, 13(3), 785–807. https://doi.org/10.1175/JHM-D-11-0112.1

Robles, M. D., Marshall, R. M., O'Donnell, F., Smith, E. B., Haney, J. A., & Gori, D. F. (2014). Effects of climate variability and accelerated forest thinning on watershed-scale runoff in southwestern USA ponderosa pine forests. PloS One, 9(10), e111092–e111092. https://doi.org/10.1371/journal.pone.0111092

Robles, M. D., Turner, D. S., & Haney, J. A. (2017). A century of changing flows: Forest management changed flow magnitudes and warming advanced the timing of flow in a southwestern US river. PloS One, 12(11), e0187875–e0187875. https://doi.org/10.1371/journal.pone.0187875

Robles, M. D., Hammond, J. C., Kampf, S. K., Biederman, J. A., & Demaria, E. M. C. (2021). Winter inputs buffer streamflow sensitivity to snowpack losses in the salt river watershed in the lower colorado river basin. Water (Basel), 13(1), 3–. https://doi.org/10.3390/w13010003

Cázares-Rodríguez, J. E., Vivoni, E. R., & Mascaro, G. (2017). Comparison of Two Watershed Models for Addressing Stakeholder Flood Mitigation Strategies: Case Study of Hurricane Alex in Monterrey, México. Journal of Hydrologic Engineering, 22(9), 5017018–. https://doi.org/10.1061/(ASCE)HE.1943-5584.0001560

Rutter, A. J., K. A. Kershaw, P. C. Robins, and A. J. Morton (1971), A predictive model of rainfall interception in forests: 1. Derivation of the model from observation in a plantation of Corsican pine, Agric. Meteorol., 9, 367–384.

Ryan, K. C., Knapp, E. E., & Varner, J. M. (2013). Prescribed fire in North American forests and woodlands: history, current practice, and challenges. Frontiers in Ecology and the Environment, 11(s1), e15–e24. https://doi.org/10.1890/120329

Sankey, J. B., Kreitler, J., Hawbaker, T. J., McVay, J. L., Miller, M. E., Mueller, E. R., Vaillant, N. M., Lowe, S. E., & Sankey, T. T. (2017). Climate, wildfire, and erosion ensemble foretells more sediment in western USA watersheds. Geophysical Research Letters, 44(17), 8884–8892. https://doi.org/10.1002/2017GL073979

Schreiner-McGraw, A. P., & Vivoni, E. R. (2018). On the Sensitivity of Hillslope Runoff and Channel Transmission Losses in Arid Piedmont Slopes. Water Resources Research, 54(7), 4498–4518. https://doi.org/10.1029/2018WR022842

Searcy, J. K., & Hardison, C. H. (1960). Double Mass Curves. Manual of hydrology: Part 1. General Surface Water Techniques. US Geological Survey, Water-Supply Paper 1541-B.

Shuttleworth, W. J. (1979), Evaporation, Rep. 56, Inst. of Hydrol., Wallingford, U. K.

Simonit, S., Connors, J. P., Yoo, J., Kinzig, A., & Perrings, C. (2015). The impact of forest thinning on the reliability of water supply in Central Arizona. PloS One, 10(4), e0121596–e0121596. https://doi.org/10.1371/journal.pone.0121596

Singh, I., Dominguez, F., Demaria, E., & Walter, J. (2018). Extreme Landfalling Atmospheric River Events in Arizona: Possible Future Changes. Journal of Geophysical Research. Atmospheres, 123(14), 7076–7097. https://doi.org/10.1029/2017JD027866

Soil Survey Staff. (2020). Gridded National Soil Survey Geographic (gNATSGO) Database for Arizona [Database]. United States Department of Agriculture, Natural Resources Conservation Service. https://nrcs.app.box.com/v/soils

Stambaugh, M. C., Guyette, R. P., & Marschall, J. M. (2011). Longleaf pine (Pinus palustris Mill.) fire scars reveal new details of a frequent fire regime: Longleaf pine (Pinus palustris Mill.) fire scars reveal fire regime. Journal of Vegetation Science, 22(6), 1094–1104. https://doi.org/10.1111/j.1654-1103.2011.01322.x

Sun, N., Yan, H., Wigmosta, M. S., Leung, L. R., Skaggs, R., & Hou, Z. (2019). Regional Snow Parameters Estimation for Large-Domain Hydrological Applications in the Western United States. Journal of Geophysical Research. Atmospheres, 124(10), 5296–5313. https://doi.org/10.1029/2018JD030140

Svoma, B. M. (2017). Canopy effects on snow sublimation from a central Arizona Basin: Canopy Effects on Snow Sublimation. Journal of Geophysical Research. Atmospheres, 122(1), 20–46. https://doi.org/10.1002/2016JD025184

Udall, B., & Overpeck, J. (2017). The twenty-first century Colorado River hot drought and implications for the future. Water Resources Research, 53(3), 2404–2418. https://doi.org/10.1002/2016WR019638

U.S. Bureau of Reclamation. (2020). Review of the Colorado River Interim Guidelines for Lower Basin Shortages and Coordinated Operations for Lake Powell and Lake Mead. https://www.usbr.gov/ColoradoRiverBasin/documents/7.D.Review_FinalReport_12-18-2020.pdf

U. S. Forest Service. (2018). Cragin Watershed Protection Project. U.S. Department of Agriculture, Forest Service, Mogollon Rim Ranger District. https://www.fs.usda.gov/nfs/11558/www/nepa/100660_FSPLT3_4301019.pdf

U. S. Forest Service. (2015). Final Environmental Impact Statement for the Four-Forest Restoration Initiative. U.S. Department of Agriculture, Forest Service, Rocky Mountain Research Station. https://www.fs.usda.gov/Internet/FSE_DOCUMENTS/stelprd3836625.pdf

U.S. Geological Survey (2016). National Water Information System data available on the World Wide Web (USGS Water Data for the Nation) [Database]. http://waterdata.usgs.gov/nwis/

Tarboton, D. G., Luce, C. H., (1996). Utah Energy Balance Snow Accumulation and Melt Model (UEB). Utah Water Research Laboratory and USDA Forest Sesvice.

Vano, J. A., Das, T., & Lettenmaier, D. P. (2012). Hydrologic Sensitivities of Colorado River Runoff to Changes in Precipitation and Temperature. Journal of Hydrometeorology, 13(3), 932–949. https://doi.org/10.1175/JHM-D-11-069.1

Vano, J. A., Udall, B., Cayan, D. R., Overpeck, J. T., Brekke, L. D., Das, T., Hartmann, H. C., Hidalgo, H. G., Hoerling, M., McCabe, G. J., Morino, K., Webb, R. S., Werner, K., & Lettenmaier, D. P. (2014). UNDERSTANDING UNCERTAINTIES IN FUTURE COLORADO RIVER STREAMFLOW. Bulletin of the American Meteorological Society, 95(1), 59–78. https://doi.org/10.1175/BAMS-D-12-00228.1

Vivoni, E. R., Ivanov, V. Y., Bras, R. L., & Entekhabi, D. (2004). Generation of Triangulated Irregular Networks Based on Hydrological Similarity. Journal of Hydrologic Engineering, 9(4), 288–302. https://doi.org/10.1061/(ASCE)1084-0699(2004)9:4(288)

Vivoni, E. R., Ivanov, V. Y., Bras, R. L., & Entekhabi, D. (2005). On the effects of triangulated terrain resolution on distributed hydrologic model response. Hydrological Processes, 19(11), 2101–2122. https://doi.org/10.1002/hyp.5671

Vivoni, E. R., Mascaro, G., Mniszewski, S., Fasel, P., Springer, E. P., Ivanov, V. Y., & Bras, R. L. (2011). Real-world hydrologic assessment of a fully-distributed hydrological model in a parallel computing environment. Journal of Hydrology (Amsterdam), 409(1), 483–496. https://doi.org/10.1016/j.jhydrol.2011.08.053

Western Regional Climate Center. (2013). Rural Automated Weather Stations [Dataset]. https://raws.dri.edu/

Wang, & Alimohammadi, N. (2012). Responses of annual runoff, evaporation, and storage change to climate variability at the watershed scale. Water Resources Research, 48(5). https://doi.org/10.1029/2011WR011444

Wang, Y.-H., Broxton, P., Fang, Y., Behrangi, A., Barlage, M., Zeng, X., & Niu, G.-Y. (2019). A Wet-Bulb Temperature-Based Rain-Snow Partitioning Scheme Improves Snowpack Prediction Over the Drier Western United States. Geophysical Research Letters, 46, 13,825–13,835. https://doi.org/10.1029/2019GL085722

Wigmosta, M., Vail, L., & Lettenmaier, D. (1994). A distributed hydrology-vegetation model for complex terrain. Water Resources Research, 32(1), 213–214. https://doi.org/10.1029/94WR00436

Wilson, Barry Tyler; Lister, Andrew J.; Riemann, Rachel I.; Griffith, Douglas M. 2013. live tree species basal area of the contiguous United States (2000-2009). Newtown Square, PA: USDA Forest Service, Rocky Mountain Research Station. https://doi.org/10.2737/RDS-2013-0013

Xiao, M. (2021). A warning of earlier snowmelt. Nature Climate Change, 11(5), 380–381. https://doi.org/10.1038/s41558-021-01024-7

Xu, C. Y., Halldin, S. (1997). The Effect of Climate Change on River Flow and Snow Cover in the NOPEX Area Simulated by a Simple Water Balance Model. Hydrology Research, 28 (4-5): 273–282. doi: https://doi.org/10.2166/nh.1998.19

Young, C., Nelson, B., Bradley, A., Smith, J., Peters-Lidard, C., Kruger, A., & Baeck, M. (1999). An evaluation of NEXRAD precipitation estimates in complex terrain. Journal of Geophysical Research. Atmospheres, 104(D16), 19691–19703. https://doi.org/10.1029/1999JD900123

Zhang, J., Qi, Y., Kingsmill, D., & Howard, K. (2012). Radar-Based Quantitative Precipitation Estimation for the Cool Season in Complex Terrain: Case Studies from the NOAA Hydrometeorology Testbed. Journal of Hydrometeorology, 13(6), 1836–1854. https://doi.org/10.1175/JHM-D-11-0145.1

Zhang, J. Y., Wang, G. Q., Pagano, T. C., Jin, J. L., Liu, C. S., He, R. M., & Liu, Y. L. (2013). Using Hydrologic Simulation to Explore the Impacts of Climate Change on Runoff in the Huaihe River Basin of China. Journal of Hydrologic Engineering, 18(11), 1393–1399. https://doi.org/10.1061/(ASCE)HE.1943-5584.0000581

Zhang, L., Hu, Z., Fan, J. et al. A meta-analysis of the canopy light extinction coefficient in terrestrial ecosystems. Front. Earth Sci. 8, 599–609 (2014). https://doi.org/10.1007/s11707-014-0446-7

Zeng, X., P. Broxton, and N. Dawson (2018). Snowpack Change From 1982 to 2016 Over Conterminous United States, Geophysical Research Letters. 45. 12940-12947. https://doi.org/10.1029/2018GL079621

APPENDIX A

A. OBSERVATIONAL DATASETS

This appendix describes the observational datasets used in this thesis which is located on a Google Drive, “Cederstrom_Thesis_Appendices” in the folder “Appendix_A.” Below is a description is of the subfolders of “Appendix_A” and the files contained within.

“USGS Stream Gauges” contains the timeseries of streamflow observations used in the study. The raw data is provided as *.txt files with the stream gauge ID shown in Table 1 as the file name. The quality-controlled data is stored in *.mat files with the same naming format. These *.mat file were used throughout the study and contains the observations and the datetimes.

“SRP Precip Gauges” contains the timeseries of precipitation observations used in the bias-correction of NEXRAD data. These gauges are not all owned by SRP but the daily data is manually quality-controlled by SRP Meteorologists. Within the folder there are two *.csv files for each gauge, one for 15 minutes data (not quality controlled) and daily data both with the units of inches. Note that the daily data is in an unusual format where the daily records are 5am to 5 am values ending on the date given. This data was loaded into Matlab as the *.csv with no further processing as the data was already quality-controlled. The 15 minute data is from tipping bucket rain gauges are prone to errors during the winter.

“SNOTEL” contains the timeseries of observations at the two SNOTEL stations referenced in this study. Within the folder there are three files for each station the first are *.csv and *.txt which is the raw data from the NRCS with the station ID shown in Table 1 as the file name. The raw data was loading into Matlab using the two scripts “HJ20022018.m” and “BM200122018.m” which were used to save the SNOTEL datasets

as *.mat files for preparation of model forcings. Note that the scripts contain the information about the original units and the unit conversions done.

"RAWS" contains all of the observational timeseries for the Rural Automated Weather Stations used to prepare the model forcings in this study. Within the folder there are one file for each station the first are *.csv which is the raw data from the USFS with the station name shown in Table 1 as the file name. These observations are hourly with the variable names and units shown in the header of each file. The precipitation data is from tipping bucket rain gauges are prone to errors during the winter.

"YCFCD" contains the precipitation observations from the Yavapai County flood Control District. This data was not used in this study but was left for posterity. The station meta data is located within the Microsoft Excel file in the folder. The subfolder contains the raw data for each of the stations data was acquired for. The datasets is raw cumulative tips of 1 mm, There are large amounts of missing data throughout the all of the datasets and winter precipitation is not to be trusted.

APPENDIX B

B. GIS DATASETS

This appendix describes the data and scripts used in this thesis which is located on a Google Drive, “Cederstrom_Thesis_Appendices” in the folder “Appendix_B”. Below is a description of the subfolders within “Appendix_B” and the files contained within. Note that all GIS data in this project is reprojected into UTM Zone 12N, North American 1983 datum coordinate system using the gdalwarp function within GDAL.

“GIS” contains the majority of the GIS project data used to complete this work. Within the folder there are subfolders dedicated to specific efforts like the folder “BarM_tRIBS_Model_Creation” which contains all the GIS datasets used to create the domain for the Bar-M SNOTEL point scale model. Another important folder is the folder “Data” which contains a number of shapefiles and rasters like shapefiles for the locations of meteorological stations and watershed outlines.

“NEXRAD” contains the NEXRAD ST4 precipitation dataset in mm/hr used to prepare the model forcing in this study. The raw NEXRAD ST4 grib files from NCEP were removed after clipping and reprojecting into GeoTiffs. The clipped and reprojected data is located in the zip file, “NEXRAD_Clipped_Projected.zip”. The clipped and reprojected data was also stored as *.mat file which was used to complete the bias-correction within Matlab. The bias-corrected forcing dataset used to run the model is located in Appendix C.3 as ASCII files.

“SWANN” contains the SWANN snow water equivalent dataset in mm downloaded from the SRP repository. This dataset is not publicly available but the clipped and reprojected rasters for the Beaver Creek watershed are provided as GeoTiffs in the zip file “SWANN_SWE_Clipped_Projected.zip”. This data was used for model calibration and validation thus the rasters were used within Matlab as *.mat files. The

*.mat file that contains all of the rasters is located within the “SWANN” folder. All other processing of the data like computing spatial averages was done within Matlab scripts.

“NLDAS” contains the NLDAS datasets used to prepare the model forcings. The raw NLDAS grib files were removed after clipping and reprojecting into GeoTiffs. The clipped and reprojected data is located in the zip file, “NLDAS_Clipped_Projected.zip”. The clipped and reprojected data was also stored as *.mat file which was used to complete the bias-correction and gap filling of station data within Matlab. The names and units of the files all correspond to the names of the meteorological variables required by tRIBS as shown in the tRIBS User Manual.

“PRISM” contains the PRISM air temperature dataset in °C used to prepare the model forcings. The raw PRISM files were removed after clipping and reprojecting into GeoTiffs. The clipped and reprojected data in the zip file, “PRISM_TA_Clipped_Projected.zip”. The clipped and reprojected data was also stored as *.mat file which was used to calculate the historical air temperature lapse rates for the Beaver Creek within Matlab.

APPENDIX C

C. MODEL SETUPS

This appendix describes the model setups and file structures for Happy Jack and Bar-M SNOTEL along with the Beaver Creek used in this thesis which is located on a Google Drive, “Cederstrom_Thesis_Appendices” in the folder “Appendix_C”. Below is a description of the subfolders of “Appendix_C” and the files contained within.

C.1 Happy Jack SNOTEL

The tRIBS model setup for the Happy Jack SNOTEL model is located in the folder “HappyJack_SNOTEL”. Within this folder there are inputs files and subfolders for model forcings (“Weather”), parameter files (“Input”), and output folders (“HJ_2002-2018_Out”). The input file for the model run over WY2013-2018 shown in this work is “HJ_2002-2018.in” which can be ran using the tRIBS model located “Appendix D”. This model was executed using Windows Subsystem for Linux (WSL) on a Windows 10 computer. The folder “Weather” contains the *.sdf and *.mdf files used to complete the annual simulations at Happy Jack. The folder “Input” contains all of the necessary model parameter and topographic data to run the model.

C.1 Bar-M SNOTEL

The tRIBS model setup for the Bar-M SNOTEL model is located in the folder “BarM_SNOTEL.” Within this folder there are inputs files and subfolders for model forcings (“Weather”), parameter files (“Input”), and output folders (“Output”). The input file for the model run over WY2013-2018 shown in this work is “BarM_2012-2018.in” which can be ran using the tRIBS model located “Appendix D.” This model was executed using Windows Subsystem for Linux (WSL) on a Windows 10 computer. The

folder “Weather” contains the *.sdf and *.mdf files used to complete the annual simulations at Bar M. The folder “Input” contains all of the necessary model parameter and topographic data to run the model.

C.3 Beaver Creek Model

The tRIBS model setup for the Beaver Creek watershed is located in the folder “BCmodel”. This model setup was originally located on the Agave High Performance Computing Cluster at ASU. Additionally, model outputs were originally not written into this folder due to storage restrictions, but the setup was adjusted to do so such that the model can be run from this folder. Within the “BCmodel” folder there are inputs files and subfolders for model forcings (“BCweather” and “BCrain”), parameter files (“BCinput”), restart files (“Restart_Files”), and output folders (“Outputs”).

Within the subfolder “BCmodel” contains the input files to the model, batch files, and a script for merging the tRIBS outputs. There are three main input files, “Calibration_WY2003-2010.in”, “Validation_WY2003-2018.in”, and Experiments_WY2003-2018.in” each one of these input files has an accompanying batch file (*.sh) which is used to initiate the job on Agave. Note that individual inputs files were not made for each simulation experiments. Instead, there was one input file and the paths within the file would be changed based on the experiment.

“BCrain” contains the bias corrected precipitation forcing for the model. Within this folder there is a readme file that contains some more general information along with the folder “NEXRAD_BC” which contains the precipitation rasters for the entire simulation period including the spin up period. The rasters are in ASCII format with units

of mm/hr as hourly rasters in the same geographic projection as all other sources of GIS data in this work.

"BCweather" contains meteorological forcings for the model that were using an algorithm to interpolate the gap-filled weather station data. Within "BCweather" there are two grid data files (*.gdf) which inform the model of the location of the meteorological forcings. These two files are for the calibration/validation simulations and the simulation experiments. The subfolder "Station_DS" contains subfolder for each of the meteorological forcings with the name corresponding to the variable. Each of these subfolders contains all of the hourly rasters entire simulation period including the spin up period in ASCII format.

"BCinput" contains all of the model inputs and parameter file for running the model. The files all use the same file types as listed in the tRIBS user manual for each of the files. The specific files are soil map and parameter table ("BCsoil_map.soi" and "BCsoil_table.sdt"), land cover map and parameter table ("BCland_map.lan" and BCland_table.ldt"), and depth to bedrock map ("BCbedrock_map.brd"). Additionally within "BCinput" there are a number of subfolder that contains model inputs. "LU_grids" contains the gridded land cover data for both vegetation fraction ("VF") and height ("VH") with the grid data files (*.gdf) for both base case and post-treatment experiments. "Parallel_Partitioning_Files" contains the *.reach files for parallel operations of the tRIBS model on Agave with the number of nodes in the file name. "PointFiles" contains the *.points file used for defining the topographic domain of the Beaver Creek model provided by Hawkins (2012).

"Restart_Files" contains the restart files for the simulations in the Beaver Creek. Restart files were necessary for this work as the simulations are long-term and a memory leak within the model causes crashes at 5 years of simulation time. Thus, restart files were written every four years and at the end of the spin up period.

"Outputs" contains all model outputs used to derive the result in this study. The spatial outputs have already been merged with the unmerged outputs removed. The naming convention is "Experiment_WY2003-2018_0C_NoThin.zip" where "0C" represents the level of warming and "NoThin" or "Thin" represent the base case and post-treatment experiments respectively.

APPENDIX D

D. tRIBS MODEL DOCUMENTATION

The tRIBS model used in this study to conduct simulations at point and watershed scales, located on Google Drive, “Cederstrom_Thesis_Appendices” in the folder “Appendix_D”. The first section provides a general overview of the tRIBS version and how to find the changes made to the code. The second section provides a more detailed overview of the various physics improvements and additions made to the code. The final section identifies and provides some initial guidance on other issues identified during the work but were not addressed.

D.1 tRIBS Model

The version of tRIBS used in this study does not include the model improvements made in Cázares-Rodríguez et al., (2017), Schreiner-McGraw et al., (2018), and Ko et al., (2019). The parent directory of the tRIBS model used for this study is located in “Cederstrom_Thesis_Appendices/Appendix_D/tribs_CJC”. A number of small adjustments were made over the course of the project and can be found within the code searching “CJC” recursively with more detailed information provided in the following sections. Additional changes were made to the model outputs in this version of the code to outputs specific variables that were used to analyze model outputs. Specifically, certain outputs were replaced with other variables, an overview of the modified outputs is provided in the Table D.1. To compile this code on the ASU’s Agave cluster first compiler must be loaded (gcc/4.4.7) then compiled using the “makeOCOTILLO_PAR” make file within the folder. Changes made to the model outputs are specific to this project and should not be implemented.

Table D.1. Summary of modifications to tRIBS outputs within the dynamic file. Changes to the outputs are highlighted in yellow.

Dynamic File Outputs		
Column	**Variable**	**Units**
1	*Node Identification, ID*	[id]
2	*Elevation, Z*	[m]
3	*Slope, S*	[|radian|]
4	*Contributing Area, CAr*	[m^2]
5	*Depth to groundwater table, Nwt*	[mm]
6	*Total moisture above the water table, Mu*	[mm]
7	*Moisture content in the initialization profile, Mi*	[mm]
8	*Wetting front depth, Nf*	[mm]
9	*Top front depth, Nt*	[mm]
10	*Unsaturated lateral flow out from cell, Qpout*	[mm/hr]
11	*Unsaturated lateral flow into cell, Qpin*	[mm/hr]
12	*Cumulative Surface Runoff, Srf*	[mm]
13	*Rainfall, Rain*	[mm/hr]
14	*Snow Water Equivalent, SWE*	[cm]
15	*Snow Temperature, ST*	[C]
16	*Ice Part of Water Equivalent, IWE*	[cm]
17	*Liquid part of Water Equivalent, LWE*	[cm]
18	*Cumulative Snow Sublimation*	[cm]
19	*Cumulative Snow Evaporation*	[cm]
20	*Cumulative Melt*	[cm]
21	*Cumulative hours Snow*	[cm]
22	*Latent Heat Flux from Snow Cover, sLHF*	[kJ/m^2]
23	*Sensible Heat Flux from Snow Cover, sSHF*	[kJ/m^2]
24	*Ground Heat Flux from Snow Cover, sGHF*	[kJ/m^2]
25	*Precipitation Heat Flux from Snow Cover, sPHF*	[kJ/m^2]
26	*Outgoing Longwave Radiation from Snow Cover, sRLo*	[kJ/m^2]
27	*Incoming Longwave Radation from Snow Cover, sRLi*	[kJ/m^2]
28	*Incoming Shortwave Radiation from Snow Cover, sRSi*	[kJ/m^2]
29	*Error in Energy Balance, Uerr*	[J/m^2]
30	*Intercepted SWE, IntSWE*	[cm]
31	*Cumulative Sublimated Snow from Canopy, IntSub*	[cm]
32	*Cumulative Unloaded Snow from Canopy, IntUnl*	[cm]
33	*Soil Moisture, top 10 cm, SoilMoist*	[ ]
34	*Root Zone Moisture, top 1 m, RootMoist*	[ ]
35	*Canopy Storage, CanStorage*	[mm]

36	*Actual Evaporation, ActEvp*	[mm/hr]
37	*Cumulative Evaporation from Bare Soil, EvpSoil*	[mm/hr]
38	*Cumulative Total Evapotranspiration, ET*	[mm/hr]
39	*Ground Heat Flux, Gflux*	[W/m^2]
40	*Sensible Heat Flux, Hflux*	[W/m^2]
41	*Latent Heat Flux, Lflux*	[W/m^2]
42	*Discharge, Qstrm*	[m^3/s]
43	*Channel Stage, Hlev*	[m]
44	*Channel Flow Velocity, FlwVlc*	[m/s]
45	*Canopy Storage Parameter, CanStorParam*	[mm]
46	*Interception Coefficient, IntercepCoeff*	[ ]
47	*Free Throughfall Coeff.- Rutter, ThroughFall*	[ ]
48	*Canopy Field Capacity – Rutter, CanFieldCap*	[mm]
49	*Drainage coefficient – Rutter, DrainCoeff*	[mm/hr]
50	*Drainage Expon. Param. – Rutter, DrainExpPar*	[mm^{-1}]
51	*Albedo, LandUseAlb*	[ ]
52	*Vegetation Height, VegHeight*	[m]
53	*Optical Transmission Coeff., OptTransmCoeff*	[ ]
54	*Canopy- Average Stomatal Resistance, StomRes*	[s/m]
55	*Vegetation Fraction, VegFraction*	[ ]
56	*Canopy Leaf Area Index, LeafAI*	[ ]

D.2 Model Changes

Unless noted otherwise the changes outline in the following section are general physics improvements or additions that allow easier use and should be considered for incorporating in the most up to date version of the code.

The first set improvements are shown in Figure B.1 that accounts for two different issues in tHydroModel.cpp. The first, shown in line 820 contains an additional “or” case that account for timesteps where the snowpack completely melted. Previous versions of the code would not have the melted snow routed to the soil surface if the snowpack disappeared in the same timestep. The second improvement, shown in line 821 the variable “Ractual” was previously “R”.

```
816           // SKY2008Snow from AJR2007
817           if (SnOpt) {
818               snWE = cn->getLiqWE() + cn->getIceWE();
819               routeWE = cn->getLiqRouted();
820               if ((snWE > 1e-3) || (routeWE > 0.)) {
821                   Ractual = 10*routeWE; //have to convert to mm // Changed from R to
                      Ractual CJC2020
822               }
823           }
```

Figure D.1. Model physics improvements for the accounting of snowmelt in tHydroModel.cpp.

```
2962            // Get Bedrock depth for computing Nwt
2963            DtoBedrock = cn->getBedrockDepth(); // added by CJC2020
```

Figure D.2. Model physics improvements for proper defining the depth to bedrock variable in tHydroModel.cpp. Note that the improvement shown in Figure D.2 also occurs in line 779 without any changes.

The previous version of the code did not properly account for the lateral transfers between adjacent cells or yield water balance issues when precipitation fell at the same timestep as snowmelt.

Figure D.2 illustrates the second set of model physics improvements made to the model in tHydroModel.cpp. Previous version of the code would not properly redefine the depth to bedrock for each Voronoi polygon, resulting in errors in the simulation of the groundwater table. Note that this fix does not impact simulations that use a constant depth to bedrock or with depths to bedrock that are extremely deep.

Figure D.3 shows the third set of model physics improvements made to the model in tHydroModel.cpp. There are numerous changes in this section of code, but they all are fixes to “Newton” function used in the unsaturated zone code when calculating the depth of the water table. Previous version of the code would had certain cases where the depth to groundwater table could be lower than the depth to bedrock. An example is shown in

```
3867        // If the flux too high, then the value of water table can numerically
3868        // go below 'DtoBedrock', just let it go down to a such depth
3869        if (PoreInd >= 5.0 || fabs(x-xinit) <= 1.0E-7  ) {
3870            for (x = xinit, i=0; i<ITMAX; x-=dx, i++) {
3871                polyn(x, fvalue, fdvalue, C1, C2, C3);
3872
3873                if (fabs(fdvalue) < DMIN) {
3874                    if (simCtrl->Verbose_label == 'Y') {
3875                        cout <<"\nWarning! NEWTON 1: derivative fell below minimum!"
3876                        <<" ID = "<<ID<<endl<<endl;
3877                        // return(x); // someone needs to look into if this should be
                            commented out CJC2020
3878                    }
3879                    Nwt_estim = x; // added by CJC2020
3880                    break; // added by CJC2020
3881                }
3882
3883                dx = fvalue/fdvalue;
3884
3885                if (fabs(dx) < DX_TOL) {
3886                    Nwt_estim = x; // added by CJC2020
3887                    break; // added by CJC2020
3888                    // return(x); // commented out by CJC2020
3889                }
3890            }
3891
3892            if (simCtrl->Verbose_label == 'Y') {
3893                cout<<"\nWarning: NEWTON 1: NO convergence in "<<ITMAX<<" steps\n";
3894                cout<<"\nERROR = "<<fvalue
3895                    <<";  Nwt_initial = "<<Nwt
3896                    <<";  dM = "<<dM
3897                    <<";  Nwt_estim = "<<x
3898                    <<";  ID = "<<ID
3899                    <<"\nInitial value is kept..."
3900                    <<endl<<endl<<flush;
3901            }
3902
3903            if (fabs(fdvalue) < DMIN) { // added by CJC2020
3904                x = Nwt_estim;
3905            }
3906            else if (fabs(dx) < DX_TOL) { // added by CJC2020
3907                x = Nwt_estim;
3908            }
3909            else { // added by CJC2020
3910                x = Nwt;
3911            }
3912        }
3913        if (x > DtoBedrock)
3914            x = DtoBedrock;
3915        return (x);
3916    }
```

Figure D.3. Model physics improvements for properly accounting for ground water fluxes and bedrock in tHydroModel.cpp. Note that multiple changes were made, denoted by CJC2020.

lines 3886-3888, which removes the “return” that would exit the entire loop and not account for the depth to bedrock in lines 3913. Someone should check for the case in line 3877. Here the original code had a “return” that returned the value of the water table depth hidden inside of a verbose labelling if-statement. This return could only ever be

```
829         // Adjust saturated hydraulic conductivity based on air
830         // temperature to account for frozen soil effects CJC2020
831         Ta_hi = 8;
832         Ta_lo = 4;
833         alphat = 0.004;
834         airTemp = cn->getAirTemp();
835         if (airTemp <= Ta_lo) {
836             Ksat = Ksat*alphat;
837         }
838         else if ((airTemp < Ta_hi) && (airTemp > Ta_lo)) {
839             Ksat = Ksat*alphat + (airTemp - Ta_lo)*((Ksat - Ksat*alphat)/(Ta_hi -
                Ta_lo));
840         }
```

Figure D.4. Model physics addition that accounts for changes in saturated hydraulic conductivity based on air temperature.

reached if verbose labelling was turned on when initially running the model. Determining whether this was a simple mistake or done on purpose was not explored in this work. If the latter was indeed a mistake, then a fix is shown in lines 3879 and 3880.

The final change in model physics within tHydroModel.cpp accounts for the effects of frozen soil on runoff generation is shown in Figure D.4. Importantly, this addition should be heavily considered or improved upon before implementation in the official release of the code. This method was implemented due to lack of data to quantify the real effects of frozen soil on runoff generation. The incorporation of a more advanced method that account for the formation of ice crystals within the soil is recommended. The latter would lead to a more rigorous implementation that accounts for changes in other soil parameters like porosity.

The next changes to the model code are no longer contained within tHydroModel.cpp, instead these fixes are involved with the simulation of snow. The first set of fixes is located tsnowPack.cpp as shown in Figure D.5. These set of fixes added the ability for the model to output snowpack sublimation and evaporation. Previous version of the code only output sublimation from the canopy snowpack. Here sections of the

```
1106          //evaporate liquid from ripe pack snWE +=
1107          if (snTempC == 0.0) {
1108        //total SWE update
1109        snWE +=  latentHFCalc(resFactCalc())*timeSteps/(rholiqkg*latVapkJ) +
1110          cmtonaught*(snUnload + mtoc*(rain))*timeSteps/3600;
1111
1112        //liq WE update
1113        liqWE += latentHFCalc(resFactCalc())*timeSteps/(rholiqkg*latVapkJ) +
1114          cmtonaught*((mtoc*rain)*(1 - snowFracCalc()))*timeSteps/3600;
1115        snEvap = latentHFCalc(resFactCalc())*timeSteps/(rholiqkg*latVapkJ)*naughttocm; //
          Calculate evaporation from snowpack in cm CJC2020
1116
1117        //solid WE update
1118        iceWE += cmtonaught*(snUnload + mtoc*(rain*snowFracCalc()))*timeSteps/3600;
1119        snSub = 0.0; // No sublimation occurs CJC2020
1120          }
1121
1122      //sublimate solid from frozen pack
1123          else {
1124
1125        //total WE update
1126        snWE +=  latentHFCalc(resFactCalc())*timeSteps/(rholiqkg*latSubkJ) +
1127          cmtonaught*mtoc*(rain)*timeSteps/3600;
1128
1129        //liq WE update
1130        liqWE += cmtonaught*(mtoc*(rain*(1 - snowFracCalc())))*timeSteps/3600;
1131        snEvap = 0.0; // No evaporation occurs CJC2020
1132
1133        //ice WE update
1134        iceWE += latentHFCalc(resFactCalc())*timeSteps/(rholiqkg*latSubkJ) +
1135          cmtonaught*(snUnload + mtoc*(rain*snowFracCalc()))*timeSteps/3600;
1136        snSub = latentHFCalc(resFactCalc())*timeSteps/(rholiqkg*latSubkJ)*naughttocm; //
          Calculate sublimation from snowpack in cm CJC2020
1137          }
```

Figure B.5. Model addition that adds the ability to the model to output snowpack sublimation and evaporation. Note that the improvement shown in Figure B.5 also occurs in lines 1106-1137 without any changes.

```
1350          // Set ET variables equal to zero CJC2020
1351          cNode->setEvapWetCanopy(0.0);
1352          cNode->setEvapDryCanopy(0.0);
1353          cNode->setEvapSoil(0.0);
1354          cNode->setEvapoTrans(0.0);
1355          cNode->setPotEvap(0.0);
1356          cNode->setActEvap(0.0);
```

Figure B.6. Model physics improvements that properly sets evapotranspiration components from tEvapoTrans.cpp.

mass balance that account for snowpack sublimation/evaporation were written to their own variable so that they can be output if necessary. This code should be implemented in the official version but before it should be considered whether to lump sublimation/evaporation into the same variable as most observations do not measure

these separately. Furthermore, care should be placed when implementing these into the variables into the model outputs. Specifically, which output files to include this in and properly updating the documentation to account for these additions.

The next set of additions to tSnowPack.cpp is shown in Figure B.6 spanning lines 1350-1356. These additions properly set the evaporative components that are normally computed in tEvapoTrans.cpp to zero when there is snow present on the Voronoi polygon. Previous versions of the code would have constant values for these components written to the outputs that were equal to the last value written to the variable for that node. The results were incorrect values of these components for the entire duration of the snowpack. While this addition should immediately be implemented into the final version of the code more work needs to be done for the evaporative components in the canopy. The current additions set the canopy components equal to zero when there is snow on the ground but does not consider snow in the canopy. Efforts need to be placed on both the physics and coding side of these changes. The physics side is understanding whether dry canopy evapotranspiration can occur if there is snow in the canopy. The coding side is also important because the canopy snow model works differently than the ground snowpack model and care should be placed when implementing the changes.

The next set of additions to the model involve adding the variable that determines the liquid water holding capacity of the snowpack to the input file (*.in) as shown in Figure D.7. Figure D.7 contains multiple sections of code within tSnowPack.cpp to account for the liquid water holding capacity. Previous versions of the code had this variable hardcoded into lines 1294 and 1298. Now the variable is read in from the input file using line 76. While this addition is important more work should be placed on doing

```
75      //parameters
76      minSnTemp = infile.ReadItem(minSnTemp,"MINSNTEMP");
77      snliqfrac = infile.ReadItem(snliqfrac,"SNLIQFRAC"); // Added by CJC 2020

1294          if (liqWE > snliqfrac*iceWE) { // Added snliqfrac by CJC2020
1295
1296            //there is enough water left over
1297            if (liqWE != snWE ) {
1298              liqRoute = (liqWE - snliqfrac*iceWE); // Added snliqfrac by CJC2020
1299              liqWE = liqWE - liqRoute;
1300              snWE = liqWE + iceWE;
1301            }
```

Figure D.7. Model additions that add the ability to specify the liquid water holding capcity of the snowpack in the input file. Note that there are two separate sections of code.

the same with other hardcoded snowpack variables like snow density, snow emissivity, albedo and albedo decay parameters, and temperature thresholds for phase partitioning. Furthermore, these parameters should be placed into their own separate file like the land data table (*.ldt) instead of the input file. Implementing this would make calibrating the snow model much simpler, rather than recompiling the code for every calibration run and would provide a more suer friendly experience. This recommended change would be rather simple, but it should be noted that certain parameters appear in both tSnowPack.cpp and tSnowIntercept.cpp.

D.3 Additional Recommendations

In addition to the recommendations with the code changes outlined in section D.2 there are other sections of the code that should be addressed. The most important of these is the memory leak that occurs during long-term simulations or in models with a large number of computational nodes. During this work, the program “Valgrind” was used to identify the presence a memory leak within the code that causes crashes mid-simulation. This issue is highly specific due to the amount of memory available across the different

computational nodes on Agave. The recommendation is to fix the issue but to properly work around the issue it is recommended to use the same computational nodes for each simulation to isolate the time at what the model crashes so that restart files can be written before the crash. Furthermore, after moving simulations to Agave from the Ocotillo cluster during this work the model began to crash at the end of the simulation while the simulation objects are being destroyed. Whether this issue is related to the memory leak was not explored. This issue cause certain files like the *mrf to be incomplete as this file being written when the crash occurs. To circumvent this issue the code was modified to write *.mrf files a few hours of simulation time before the model crashed

There exists a problem with the code when restarting the model from a restart file and using gridded land cover data. This issue was explored but the problem was not found. When restarting from a restart file and using gridded land cover the model will set incorrect values to node. The issue is most apparent when using the interpolation option for interpolating temporally between grids which can result in erroneous values like negative values of vegetation fraction, eventually crashing the simulation in certain situations. The issue is less apparent when using high temporal resolution grids because error is only carried through a small period in time but if using monthly the error can persist throughout the month. More work should first be done in narrowing down the problem by testing whether the issue occurs with or without the snow model on before attempting to fix the issue.

A large amount of effort was placed on closing the basin scale water balance which was essentially achieved but this was accomplished through the calibration of model parameters. Previous parameter sets would result in ET/P ratios greater than 1.5

for the majority of water years. While the incorrect behavior was essentially fixed for the Base Case, when looking at the water balance for the simulation experiments that water balance is not closed as shown in Table F.1-F.9 in the Appendix F. The cause for this issue was not able to be explored. Further examination of this issue should start with checking the water balance with and without the snow model. Additionally, check that the error does not lie within the model outputs rather than the actual code itself. One example of this is shown in Figure D.6 where incorrect values of *ET* components were written to the output files. To determine if the model physics are incorrect rather than model outputs, run the model at a point scale with a set of artificial inputs like 1 mm/day of precipitation. Start with short simulations then expand to

APPENDIX E

E. FIGURES AND SCRIPTS

The files used to process data and generate the figures shown throughout the thesis is located on Google Drive, “Cederstrom_Thesis_Appendices” in the folder “Appendix_E”. The first section provides an overview of the Matlab and ArcMap files used to construct the figures shown in the thesis. The second section is provides the Microsoft Excel files used to construct the tables shown in the thesis. The final section provides an overview of a number of Matlab scripts used to process model outputs along with other efforts in the thesis.

E.1 Figures

The majority of the figures in this thesis were generated using Matlab. Initially spatial maps were generated using ArcMap but using Matlab resulted in easier construction. The only figure generated using ArcMap is Figure 1. Additionally, Figure 1 was also edited using the vector graphic editor, Inkscape. The only other figures not constructed in Matlab are Figures 2 and 31 which generated using Microsoft PowerPoint. The figure construction was organized such that referencing them later is fast and simple. Within “Appendix_E” the folder “Figures” contains a number of subfolders with the name “fig_XX_identifier” where XX is the figure number in this thesis document and identifier is a short description that was used by the writer of these scripts to quickly reference them without looking at the thesis document. Within each figure folder there is a Matlab script (*.m) with the same name as the folder, a subfolder that contains the data used to construct the figure, and two final versions of the figure stored as an 800-dpi tiff file and a Matlab figure file (*.fig).

E.2 Tables

The tables in this thesis were all first constructed in Microsoft Excel then brought into the thesis document. The tables are stored in “Appendix_E” in the folder “Tables” with same naming convention as the figures described in section E.2. The exception is that the Excel file are not with individual subfolders and instead all within the folder “Tables”.

E.3 Agave Matlab

For this study basins scale simulations output dynamic files at a daily resolution which took up large amounts of storage space. In order to reduce final storage size and complete initial data processing Matlab was utilized on the Agave cluster. The folder containing these Matlab scripts is found in “Appendix_E” in the folder “Matlab_Agave”. Within this folder contains scripts for the processing (*.m) and executing the jobs on the cluster (*.sh). The different Matlab scripts are all similar but were used for different phase of the project (calibration, validation, and simulation experiments). To explain how these scripts work the versions for the simulation experiments is discussed as they contain the most improvements out of all the scripts. The first Extract_WYMaps.m, will load the dynamic file outputs into Matlab and select the columns of interest. With the outputs the data will be stored raw in an array or gridded into rasters using spatial interpolation to a specified resolution. Furthermore, within this script the data is aggregated to mean annual values. The second script, Create_SWEGrids.m uses the dynamics outputs similar to the last script but deals only with SWE by gridding the data into rasters the same resolution and spatial extent as the SWANN dataset. Both of these

scripts will save the data as .mat files after completion which is then download from the cluster into the individual folder for each simulation. Note that these scripts take approximately eight hours to run on Agave for each simulation and specific details about the scripts is located within the scripts as comments.

APPENDIX F

F. ANNUAL WATER BALANCES FOR SIMULATION EXPERIMENTS

This appendix contains the annual water balance for the nine simulation experiments calculated using the the *.mrf files from model outputs for the Beaver Creek tRIBS model.

Table F.1. Basin scale annual water balance for BC1.

Water Year	**Q_{sim}**	**P**	**ET**	**S_g**	**S_c**	**ET_{tot}**	**dS/dt**	**Q_{sim}/P**	**ET_{tot}/P**
				[mm/yr]					
2003	134	692	409	31	29	469	106	0.19	0.68
2004	26	406	344	27	26	396	-19	0.06	0.98
2005	125	888	419	29	29	476	296	0.14	0.54
2006	10	363	383	14	13	410	-65	0.03	1.13
2007	19	403	373	29	16	417	-63	0.05	1.03
2008	76	557	356	52	32	440	19	0.14	0.79
2009	54	438	341	34	23	397	-26	0.12	0.91
2010	119	627	321	59	24	403	80	0.19	0.64
2011	67	529	384	43	23	450	17	0.13	0.85
2012	49	543	391	36	27	454	50	0.09	0.84
2013	84	589	398	41	33	472	120	0.14	0.80
2014	32	433	351	14	9	374	54	0.07	0.86
2015	60	549	415	5	5	426	69	0.11	0.78
2016	39	490	444	38	22	504	-113	0.08	1.03
2017	80	593	451	25	24	500	0	0.14	0.84
2018	17	277	371	12	8	392	-166	0.06	1.41
Mean	62	524	385	31	21	436	23	0.11	0.88

Table F.2. Basin scale annual water balance for BC2.

Water Year	Q_{sim}	P	ET	S_g	S_c	ET_{tot}	dS/dt	Q_{sim}/P	ET_{tot}/P
				[mm/yr]					
2003	124	692	443	15	12	470	130	0.18	0.68
2004	27	406	368	15	11	395	-14	0.07	0.97
2005	110	888	490	2	12	504	325	0.12	0.57
2006	10	363	408	8	7	423	-81	0.03	1.17
2007	18	403	407	15	7	429	-69	0.04	1.06
2008	93	557	393	25	14	432	25	0.17	0.78
2009	62	438	373	16	10	399	-30	0.14	0.91
2010	147	627	363	22	7	392	78	0.23	0.63
2011	56	529	435	19	14	468	26	0.11	0.89
2012	48	543	431	20	12	463	47	0.09	0.85
2013	80	589	436	25	18	480	119	0.14	0.82
2014	29	433	377	8	6	391	48	0.07	0.90
2015	48	549	449	1	2	452	70	0.09	0.82
2016	46	490	476	21	11	509	-125	0.09	1.04
2017	71	593	492	14	12	517	2	0.12	0.87
2018	15	277	395	6	4	406	-177	0.06	1.46
Mean	61	524	421	15	10	446	23	0.11	0.90

Table F.3. Basin scale annual water balance for BC4.

Water Year	Q_{sim}	P	ET	S_g	S_c	ET_{tot}	dS/dt	Q_{sim}/P	ET_{tot}/P
				[mm/yr]					
2003	106	692	478	6	3	487	146	0.15	0.70
2004	24	406	394	7	4	405	-10	0.06	1.00
2005	82	888	542	-2	5	544	337	0.09	0.61
2006	11	363	429	4	3	436	-96	0.03	1.20
2007	15	403	437	5	2	444	-75	0.04	1.10
2008	85	557	435	6	4	446	37	0.15	0.80
2009	59	438	402	6	2	410	-27	0.13	0.94
2010	161	627	409	-1	1	410	73	0.26	0.65
2011	46	529	471	9	8	487	28	0.09	0.92
2012	38	543	473	9	5	487	48	0.07	0.90
2013	65	589	480	11	9	500	119	0.11	0.85
2014	23	433	402	3	5	411	37	0.05	0.95
2015	40	549	471	0	1	471	62	0.07	0.86
2016	49	490	505	9	6	520	-132	0.10	1.06
2017	74	593	521	6	4	531	-4	0.13	0.89
2018	8	277	416	3	2	421	-183	0.03	1.52
Mean	55	524	454	5	4	463	22	0.10	0.93

Table F.4. Basin scale annual water balance for BC6.

Water Year	Q_{sim}	P	ET	Sg	Sc	ET_{tot}	dS/dt	Q_{sim}/P	ET_{tot}/P
				[mm/yr]					
2003	87	692	507	1	1	509	156	0.13	0.74
2004	20	406	416	2	1	419	-14	0.05	1.03
2005	67	888	571	-1	3	573	328	0.08	0.65
2006	13	363	444	1	1	446	-109	0.04	1.23
2007	12	403	456	1	0	457	-78	0.03	1.13
2008	54	557	469	1	2	472	55	0.10	0.85
2009	45	438	432	0	0	432	-26	0.10	0.98
2010	133	627	449	-2	0	446	82	0.21	0.71
2011	33	529	503	4	3	510	20	0.06	0.96
2012	28	543	506	1	2	509	42	0.05	0.94
2013	53	589	511	4	4	519	119	0.09	0.88
2014	17	433	419	2	4	424	27	0.04	0.98
2015	34	549	485	0	0	485	56	0.06	0.88
2016	40	490	529	3	3	535	-132	0.08	1.09
2017	68	593	547	1	1	549	-9	0.11	0.93
2018	3	277	431	1	0	433	-193	0.01	1.56
Mean	44	524	480	1	2	482	20	0.08	0.97

Table F.5. Basin scale annual water balance for PT0.

Water Year	Q_{sim}	P	ET	Sg	Sc	ET_{tot}	dS/dt	Q_{sim}/P	ET_{tot}/P
				[mm/yr]					
2003	134	692	380	29	27	436	141	0.19	0.63
2004	27	406	319	26	24	369	13	0.07	0.91
2005	128	888	393	27	26	446	332	0.14	0.50
2006	12	363	367	13	12	392	-42	0.03	1.08
2007	20	403	358	28	15	400	-48	0.05	0.99
2008	80	557	348	48	29	425	33	0.14	0.76
2009	57	438	333	32	20	386	-16	0.13	0.88
2010	133	627	312	54	21	386	87	0.21	0.62
2011	73	529	380	38	21	440	26	0.14	0.83
2012	56	543	383	33	25	441	60	0.10	0.81
2013	100	589	386	38	30	454	105	0.17	0.77
2014	39	433	344	12	9	365	72	0.09	0.84
2015	79	549	408	5	5	418	45	0.14	0.76
2016	51	490	431	36	20	488	-113	0.10	1.00
2017	99	593	436	23	22	480	-3	0.17	0.81
2018	18	277	355	12	7	375	-148	0.06	1.35
Mean	69	524	371	28	20	419	34	0.12	0.85

Table F.6. Basin scale annual water balance for PT1.

Water Year	Q_{sim}	P	ET	Sg	Sc	ET_{tot}	dS/dt	Q_{sim}/P	ET_{tot}/P
				[mm/yr]					
2003	133	692	395	21	18	434	154	0.19	0.63
2004	26	406	331	19	17	367	18	0.06	0.90
2005	127	888	430	9	17	456	344	0.14	0.51
2006	11	363	379	10	9	399	-50	0.03	1.10
2007	19	403	374	21	10	405	-50	0.05	1.00
2008	90	557	364	36	20	420	33	0.16	0.75
2009	62	438	350	21	14	385	-19	0.14	0.88
2010	147	627	332	35	12	380	82	0.23	0.61
2011	69	529	404	25	16	446	29	0.13	0.84
2012	54	543	401	25	18	444	61	0.10	0.82
2013	100	589	404	29	23	457	104	0.17	0.78
2014	37	433	356	9	7	372	69	0.09	0.86
2015	75	549	424	2	3	429	46	0.14	0.78
2016	54	490	447	27	15	489	-118	0.11	1.00
2017	94	593	455	17	16	489	-2	0.16	0.82
2018	17	277	366	9	5	381	-152	0.06	1.37
Mean	70	524	388	20	14	422	34	0.12	0.85

Table F.7. Basin scale annual water balance for PT2.

Water Year	Q_{sim}	P	ET	Sg	Sc	ET_{tot}	dS/dt	Q_{sim}/P	ET_{tot}/P
				[mm/yr]					
2003	125	692	412	14	11	437	167	0.18	0.63
2004	27	406	342	14	10	367	19	0.07	0.90
2005	114	888	463	1	11	476	354	0.13	0.54
2006	11	363	391	8	7	406	-58	0.03	1.12
2007	18	403	391	15	6	412	-53	0.04	1.02
2008	97	557	385	22	13	419	34	0.17	0.75
2009	63	438	365	14	9	388	-19	0.14	0.89
2010	159	627	352	20	6	378	81	0.25	0.60
2011	64	529	427	17	12	456	31	0.12	0.86
2012	52	543	421	18	11	450	60	0.10	0.83
2013	95	589	424	23	17	464	103	0.16	0.79
2014	34	433	369	6	6	381	66	0.08	0.88
2015	70	549	438	1	2	440	45	0.13	0.80
2016	58	490	461	20	10	491	-123	0.12	1.00
2017	92	593	472	12	11	495	-2	0.15	0.83
2018	16	277	377	6	4	387	-156	0.06	1.39
Mean	68	524	406	13	9	428	34	0.12	0.87

Table F.8. Basin scale annual water balance for PT4.

Water Year	Q_{sim}	P	ET	Sg	Sc	ET_{tot}	dS/dt	Q_{sim}/P	ET_{tot}/P
				[mm/yr]					
2003	106	692	444	6	3	452	185	0.15	0.65
2004	24	406	366	6	4	376	23	0.06	0.93
2005	90	888	512	-2	5	514	364	0.10	0.58
2006	12	363	412	3	3	418	-75	0.03	1.15
2007	16	403	419	5	2	426	-59	0.04	1.06
2008	90	557	425	5	4	434	43	0.16	0.78
2009	59	438	393	5	2	400	-17	0.14	0.91
2010	168	627	398	-1	1	398	76	0.27	0.63
2011	53	529	461	8	7	476	34	0.10	0.90
2012	43	543	460	8	5	472	59	0.08	0.87
2013	84	589	462	10	8	481	101	0.14	0.82
2014	28	433	391	3	4	398	56	0.07	0.92
2015	62	549	457	0	1	457	40	0.11	0.83
2016	60	490	488	8	6	502	-131	0.12	1.02
2017	94	593	499	5	4	508	-6	0.16	0.86
2018	8	277	395	3	2	399	-160	0.03	1.44
Mean	62	524	436	4	4	444	33	0.11	0.90

Table F.9. Basin scale annual water balance for PT6.

Water Year	Q_{sim}	P	ET	Sg	Sc	ET_{tot}	dS/dt	Q_{sim}/P	ET_{tot}/P
				[mm/yr]					
2003	87	692	470	1	1	472	197	0.13	0.68
2004	21	406	386	2	1	389	21	0.05	0.96
2005	78	888	539	-1	3	542	353	0.09	0.61
2006	14	363	426	0	1	427	-86	0.04	1.18
2007	12	403	437	1	0	438	-62	0.03	1.09
2008	66	557	454	1	1	457	54	0.12	0.82
2009	47	438	420	0	0	419	-15	0.11	0.96
2010	146	627	434	-2	0	432	80	0.23	0.69
2011	41	529	490	3	3	497	27	0.08	0.94
2012	33	543	491	1	2	494	55	0.06	0.91
2013	73	589	491	3	4	499	100	0.12	0.85
2014	22	433	405	2	3	410	47	0.05	0.95
2015	56	549	469	0	0	469	38	0.10	0.85
2016	54	490	509	3	2	514	-133	0.11	1.05
2017	88	593	522	1	1	524	-9	0.15	0.88
2018	4	277	408	1	0	410	-167	0.01	1.48
Mean	53	524	459	1	2	462	31	0.09	0.93